Title

Dynamics of the Artificial Axon

Author

Pi, Ziqi

Publication Date

2024

Peer reviewed|Thesis/dissertation

UNIVERSITY OF CALIFORNIA
Los Angeles

Dynamics of the Artificial Axon

A dissertation submitted in partial satisfaction
of the requirements for the degree
Doctor of Philosophy in Physics

by

Ziqi Pi

2024

ABSTRACT OF THE DISSERTATION

Dynamics of the Artificial Axon

by

Ziqi Pi
Doctor of Philosophy in Physics
University of California, Los Angeles, 2024
Professor Giovanni Zocchi, Chair

The "Artificial Axon" (AA) is a synthetic excitable system developed in the Zocchi lab, constructed with the minimal biological components. Based on traditional black lipid membrane setups, the AA is the first cell-free platform capable of producing action potentials (APs) in time. This dissertation details the results of my work with the AA, using the voltage gated potassium channel KvAP as the active ingredient. First, I report on experimental measurements with the AA near the threshold for firing APs, a critical point of the system. In particular, a delay in firing occurs due to the presence of a saddle node bifurcation, and a scaling exponent for this delay is measured. Supplemented by numerical results, I show that this behavior near the critical point has correspondence to the real neuron, due to the universal nature of the dynamics near a critical point. Next, I will characterize the AA in terms of its phenomenology. Using a minimal 3D model based on the Hodgkin-Huxley model, I construct a qualitative phase diagram in the parameter space of the system. The existence of limit cycle regions in this phase diagram indicates that the AA is capable of generating self sustaining AP trains with just a single ion channel. The analysis also shows that the AA, having just one channel species with inactivation, possesses all the same dynamics as a

two ion species system without inactivation, such as the Morris-Lecar model for the muscle fiber of the giant barnacle. This result is followed by measurements of the effective inactivation and recovery rates for our minimal model, qualitatively placing the AA with KvAP on the phase diagram. Finally, I will present work on an experimental system consisting of two AA connected by electronic "synapses", and explore the feasibility of constructing an autonomous oscillator with such a configuration. The connection of two AAs serves as a first step for our long term goal of AA based networks. The dissertation concludes with a short discussion on future directions for the Artificial Axon system.

The dissertation of Ziqi Pi is approved.

Dolores Bozovich

Shenshen Wang

Shimon Weiss

Giovanni Zocchi, Committee Chair

University of California, Los Angeles

2024

To you and me.

TABLE OF CONTENTS

LIST OF FIGURES

LIST OF TABLES

ACKNOWLEDGMENTS

First and foremost, I want to express my gratitude to Giovanni Zocchi, my advisor, for his mentorship during my time in the lab. Working under Giovanni's guidance has been instrumental in developing my skills as a researcher and physicist; his words of wisdom have helped shape my views on research, academia, and life in general. I am especially thankful for his unwavering support during these extraordinary times in the last few years.

I also want to acknowledge the current and former members of the Zocchi lab: Yilin Wong, the sagacious one, who has often dispensed helpful suggestions during discussions of our research; Hector Vasquez, who helped me get started on the Artificial Axon experiment, and showed me the "art" of producing KvAP; and Tri Chau, whose immaculate work station inspired me to improve my organizational skills. I've also enjoyed the company of our undergrad members: Daphne Chen, Yihong Xu, Xinyi Qi, Gale Sukarom, and Ruiyao Liu, all of whom left a lasting impression on me through our chats of research and daily life during periods of peace in the lab.

I deeply appreciate the helpful advice and encouragement given by my committee members, as well as the knowledge I've gained from discussions with all the professors in the physics department who I've interacted with during my time as a grad student, whether it be in classes, journal clubs, or research presentations.

Finally, I want thank my friends and family, all of whom generously provided me with the most important aspects of life outside the lab: bread and circuses. Special thanks to Joanne Lu, who has always been there for me.

VITA

2016	B.S. in Physics, University of California, Riverside
2016	B.S. in Applied Mathematics, University of California, Riverside
2017	M.S. in Physics, University of California, Los Angeles
2016 - 2023	Teaching Assistant, University of California, Los Angeles
2018 - 2024	Graduate Student Researcher, University of California, Los Angeles

PUBLICATIONS AND PRESENTATIONS

Ziqi Pi and Giovanni Zocchi. "Critical behavior in the artificial axon".
J. Phys. Commun., 5:125013, 2021.

Ziqi Pi and Giovanni Zocchi. "Action potentials in vitro: theory and experiment".
arXiv:2403.03369, 2024

Ziqi Pi and Giovanni Zocchi. "Cell-free action potentials as a dynamical system".
APS March Meeting, Las Vegas, NV, N00.00333, 2023

CHAPTER 1

Introduction

In the pursuit of understanding complex biological systems, an often rewarding approach is to construct a minimal system in a controlled, synthetic environment, which is inspired by the more sophisticated natural counterpart. In recent history, a great many innovations have been brought about through inspiration from unique phenomena which occur in nature. Some unconventional examples include the creation of Velcro from the clinging properties of the *Arctium* plant, and the development of ultrahydrophobic paints from investigations into the self-cleaning properties of lotus leaves [2]. Novel inventions aside, a more relevant example is perhaps the influence biological computation has had on the rapidly advancing field of artificial intelligence. Many of the innovations which contributed to the advancement of AI have basis in the mechanisms which living organisms use to "think" and compute, and although philosophers have grappled with the concepts of consciousness and thought for centuries, understanding of the underlying physiological mechanisms has only come to pass in recent decades. It is now understood that, at the cellular level, neurons and synapses serve as the fundamental units which are responsible processing and transmitting information in the context of neurobiology [3]; neurons acts as the processing units while synapses transmit and integrate the signals between neurons. These processes are in turn mediated by voltage spikes in the membranes of neurons: action potentials.

1.1 Action Potentials and Ion Channels

From an anthropological perspective, action potentials are among the most consequential dynamical systems on Earth. The information contained in their frequency and spiking patterns are utilized not just in the processing of information in the nervous system, but also in a host of other physiological functions, e.g. pacemaking in the heart and the production of insulin in the pancreas [4, 5]. These rapid fluctuations of the membrane potential are powered by concentration gradients of various ions across the cell membrane. Perhaps the most well known feature of action potentials is that their generation is based on the "all-or-none" principle; the output of an action potential requires an input which exceeds a threshold, while the exact magnitude and duration of a suprathreshold input has little to no effect on the characteristics of the resulting action potential.

Electrophysiology, the study of electrical phenomena in biological systems, has an extensive history dating back to the 17th century, yet knowledge of action potentials is comparatively recent; the first recordings were made by Julius Bernstein in 1868. Furthermore, the modern explanation for how action potentials are produced, the ionic theory of membrane potential and excitability, did not gain widespread acceptance until the mid-20th century, after Alan Hodgkin and Andrew Huxley provided strong evidence with their mold breaking experiments on the squid giant axon [6]. Hodgkin and Huxley were among the first to make direct recordings of the current across a cellular membrane, making use of Cole and Marmont's newly developed technique of voltage clamping, a method in which the membrane potential of a cell is held fixed by an external feedback circuit. Based on their measurements on the axon of the longfin inshore squid, they formulated a model which uses an equivalent circuit representation for the flow of ions across a membrane. Crucially, they proposed that the conductances of individual ions should be independent functions of the transmembrane potential, with the specific form of the conductance determining the excitability characteris-

tics of the membrane. They validated this theory by showing that the model quantitatively accounted for the excitations seen in their experiment [7]. The Hodgkin-Huxley (HH) model still remains relevant today, forming a class of models for action potential generation known as "conductance based models", with the proposed mechanisms of ion conduction being applicable to any excitable cell [4]. The molecular basis of voltage dependent conductances in the HH model also pointed to the existence of a structure within cell membranes which allowed for the selective passage of ions — known today as ion channels, though their existence would not be confirmed by experiment until the 1970s.

Ion channels are macromolecular pores embedded in the membranes of excitable cells which serve as the fundamental excitable elements in the generation of action potentials [8]. While their evolutionary origins remain uncertain, ion channels exhibit considerable diversity. More than 300 different ion channels have identified in the human genome [9], and though the role of ion channels in non-animal organisms is still poorly understood, a large variety have been identified in microbes as well [10]. As the name implies, the role of the ion channel is to allow passage of specific ions through the cellular membrane, but only when specific conditions are met ("gating"). Channels are predominantly classified by the type of ion they allow passage (Na^+, K^+, Ca^{2+}, or Cl^-), and by the their gating mechanism (voltage, chemical, pressure, etc). The diverse properties of these different channels lead to the qualitative differences in action potentials generated across a wide spectrum excitable cells.

1.2 Modern Directions

Experimental electrophysiology saw swift advancements in the decades following Hodgkin and Huxley's measurements. In the late 1970s, Erwin Neher and Bert Sakmann combined

several novel methods developed in the preceding decade and introduced the patch clamp technique, in which a small tip ($\sim 1 - 2\,\mu$m in diameter) filled with electrolytic solution is pressed against the surface of a cell, electrically isolating a "patch" from the rest of the cell membrane. This revolutionary new approach made single molecule experiments possible for the first time, and measurements of the current through individual ion channels as they opened and closed were obtained. A further refinement of the technique came soon after with the introduction of the "gigaseal" patch clamp, which was modified to have suction between the membrane and the tip. This vastly increased the seal's resistance and as a result significantly enhanced the signal-to-noise ratio of the current recordings. This improved version of the patch clamp remains the preferred technique for a wide array of present-day electrophysiological studies, owing to it's minimal noise and broad applicability [6]. Alongside these advances in experimental techniques, modern neuronal models have also seen significant refinement since the original HH model. Incorporation of microscopic effects that were previously poorly understood or neglected, such as channel kinetics, axon models and the role of glial cells, have allowed these newer models to more closely reproduce the measured electrical activities of more complex systems [3].

Separate from in vivo studies of action potentials, there has also been growing emphasis on research of isolated ion channels; motivations vary, from efforts to explain the mechanisms for channel gating [11], to quantifying their impact on human health and disease [12]. In regards to the former, imaging of channel structures with x-ray crystallography [13] and cryogenic electron microscopy (cryoEM) [14] have led to a detailed understanding of the conformational changes ion channels undergo when switching between different states. These results are complemented by in vitro investigations of isolated channels, which are typically carried out by inserting them into artificial lipid bilayers. Examining channels in an extracellular setting offers significantly improved control over experimental conditions; this in turn facilitates a more systematic approach to the categorization of ion channel properties [15].

Another direction which has surged in popularity in recent years is the replication of neuronal behaviors using electronics. Neuromorphic engineering aims to mimic the structure and function of neuronal networks using silicon integrated circuits [16]. A main motivator in this endeavor is the low power consumption of the human brain ($\sim 20\,\mathrm{W}$), a tiny fraction of the power consumed by modern electronic devices [17]. In addition, the ability for biological neural networks to "adapt" is a key feature which many machine intelligence designs seek to emulate, and to that end techniques such as spiking neural networks have been developed to more closely align the electronic networks with their biological counterparts. Despite only recently coming into the mainstream, electronic implementations of spiking behavior has had a long history. The first neuromorphic circuits consisted of MOSFETs, and were relatively simple devices with high power consumption. Nowadays, with modern advances in electronics and materials science, the scale of advanced neuromorphic devices have increased dramatically. Cutting edge implementations involve millions of electrical "neurons" and "synapses", with greatly reduced power consumption rivaling those of the actual biological system [3].

In summary, the unique properties of action potentials, in addition their central role in physiological processes, have inspired several directions of research. In vivo studies focus on production of action potentials within a cellular context; experiments typically involve cell preparations which are clamped and immersed in a electrolytic solution, using various external stimulus to obtain spiking patterns or current recordings. Similarly, modern models for action potential generation aim to be aligned with experimental findings, and as a result are concerned with accurately describing dynamics on the scale of individual neurons and neuronal networks. These models require a high amount of complexity in order to account for the various biological processes. In contrast, electronic implementations seek to reverse engineering the biologically system, mimicking spiking neurons with intricate circuits of

transistors. These implementations have the advantage of scale, with focus on the emergent properties of the network, rather than the microscopics of the individual action potential.

With the ultimate objective of understanding the processes which constitute "thought", our path in pursuit of this goal is to move away from the reverse engineering strategy, and embrace the bio-inspired constructionist philosophy. To that end, we take a slightly different approach to this problem, from the view of building up from action potentials.

1.3 The Artificial Axon

In recent years, the Zocchi lab has introduced the idea of producing cell-free action potentials in vitro [18, 19]. The platform, known as the "Artificial Axon" (AA, for short), is an artificial excitable system which is capable of generating action potentials in time. Unlike electronic realizations of the action potential, the AA has same microscopic mechanisms for voltage dynamics as real excitable cells, consisting of reconstituted biological components (phospholipid membrane and ion channels) immersed in electrolytic solution. The setup is a modified version of traditional painted bilayer experiments, with voltage gated potassium ion channels as the active elements of the system. We use the Archaean channel KvAP, which is expressed and reconstituted entirely within the lab. Non-traditionally, a modified voltage clamp is used to hold the system in an off-equilibrium excitable state. This clamp plays a role similar to the second ionic species of an excitable cell, and is the key component which allows for voltage dynamics.

While the AA is designed to have the same underlying mechanism for generating APs as the neuron, it is not an attempt at replicating one. Our philosophy is to define a minimal system; a tool to generate action potentials from the bottom up. We start by exploring the simplest dynamics related to action potentials, and proceed from there. The experimental

system also provides motivation and inspiration for developing models and theories in the general field of complex systems.

The discussion of the AA begins with an overview of the experimental platform (Ch. 2), followed by a description of the kinetic model used to describe the dynamics of the system (Ch. 3). After the AA is introduced in full, I will present the results of my work with the AA, starting with experimental measurements on critical behavior in the physical AA, near the threshold for firing (Ch. 4). We find that behavior near the threshold for firing corresponds to that of a saddle node bifurcation, the same correspondence as in real neurons. A scaling exponent is measured and compared to the predicted result obtained from modeling the AA as a 1D dynamical system. Next, focusing on the model we have developed for the AA, I will present a thorough analysis of the system in parameter space, discussing phase diagrams, identifying transitions, and building physical understanding through comparisons to other systems with similar physics (Ch. 5). A key insight is that a system with one ion channel species possessing inactivation (the AA with KvAP) can be phenomenologically equivalent to a system with two channel species without inactivation (the Morris-Lecar model). As the Morris-Lecar dynamical system accurately describes the electrophysiology of actual biological tissue (the muscle fiber of the Chilean barnacle) [20], we can say that the one channel species Artificial Axon is a simpler, more minimal system which is in theory capable of the same basic phenomenology as a biological one. Penultimately, I will discuss nascent work on systems of interconnected AAs (Ch. 6). A long term goal of the project is to construct and study networks of AAs. As a first step, two AAs are connected through electronic "synapses", introducing the element of feedback to the system. Experimental data along with numerical results show that with two AAs, it is possible to construct an "oscillator", in which two separate AAs fire continuously and autonomously through positive and negative feedback. Finally, I will conclude with a brief discussion on the future direction of the AA platform (Ch. 7). The AA, being minimal in its ingredients and construction, is a modular

system that can be adapted to survey a variety of electrophysiological phenomenon. Certain modifications, such as incorporation of different kinds of channels (mechanosensitive, photosensitive, etc.) or the addition of a second ion species, can be readily implemented with the current setup. More ambitious directions, such as space extended AP generation or large scale AA networks, present a larger challenge and will require radical improvements to the system.

CHAPTER 2

Materials and Methods

This chapter will serve as an overview of the Artificial Axon system as an experimental platform. Specifications of the components, operating protocols, and methods for procuring ion channels will be described in detail. The AA system has gone through several iterations throughout the years, being maintained, updated, and improved by the work of previous lab members [21, 22].

A brief overview of the physical system in its current iteration is as follows: The primary ingredients is the voltage gated ion channel KvAP, which is the active component in generating action potentials. The channels are inserted into a phospholipid bilayer which rests on a $\sim 200\,\mu$m hole at the bottom of a plastic cup. The cup itself is firmly held in place in a custom made Teflon chamber. The lipid membrane separates the Teflon compartment and the inside of the plastic cup, and both sides are immersed in electrolyte solution. The outer chamber is grounded, while the inner chamber's voltage is controlled and monitored by AgCl electrodes which connect the system to computer control via custom circuitry. Fig. 2.1 depicts a schematic of the setup, along with a picture of the chamber.

2.1 Apparatus

The exterior solution of the AA setup is housed in a custom made Teflon chamber, which rests upon a metal plate with a rectangular hole cut in the center. The hole is fitted with

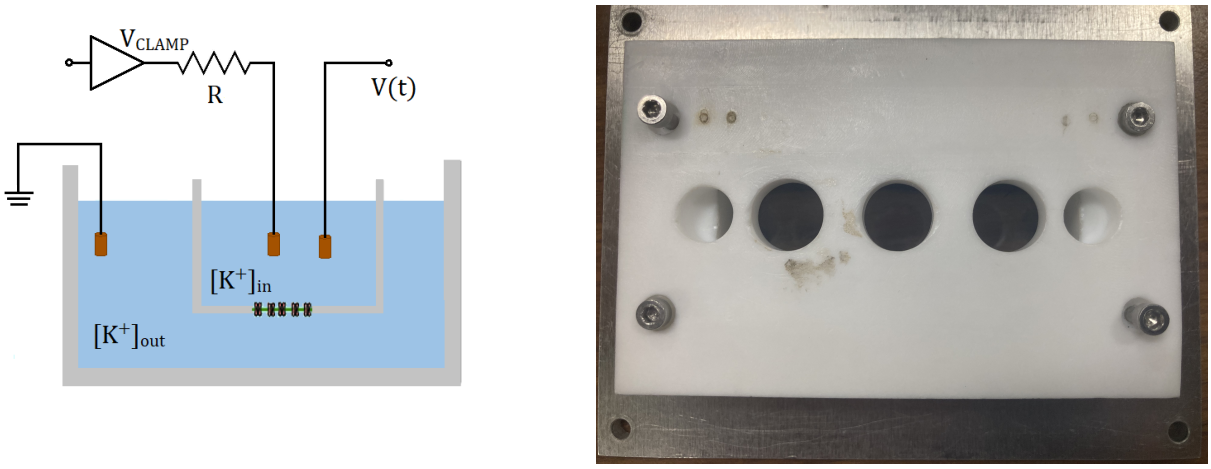

Figure 2.1: **Left:** Schematic of the Artificial Axon setup (not to scale), displaying all the essential components. **Right:** The chamber which houses the AA system.

a glass slide to facilitate observation with an optical microscope, and sealed with rubber lining. The chamber is secured to the microscope stage via screw holes in the metal piece, and the total volume of the Teflon chamber is $\approx 20\,\text{mL}$. The interior solution is housed in standard plastic centrifuge cups, which sit securely in premade holes in the Teflon chamber. The cups are sourced from Beckman-Coulter and modified for use in the experiment, based on techniques from [21]. They are first cut to a length such that the top of the cup sits flush with the chamber, while the bottom rests just above the glass slide; this results in an interior volume of $\approx 300\,\mu\text{L}$. Then, using a heated metal tip, a conical protrusion is created at the bottom of the cup, the tip of which is carefully sliced off using a razor blade so that a small aperture is created. This hole is serves as the support for the phospholipid membrane and is typically of the size $100 - 200\,\mu\text{m}$. Smaller holes are generally preferred for their stability. The Teflon chamber in its current form can house up to three cups (i.e. three AAs), though only two are currently in use.

2.2 Chamber Solutions

To create the transmembrane ion concentration difference required for generating an action potential, the two chambers of the AA (inside and outside the cup) are filled with salt solutions of differing concentration. The specific salt used depends on the type of ion channel in the membrane (e.g. KCl for KvAP), and the ratio of concentrations directly determines the peak voltage of the action potentials generated (the Nernst potential). For KvAP, the typical choice is $[\mathrm{KCl}]_{in} = 30\,\mathrm{mM}$, and $[\mathrm{KCl}]_{out} = 150\,\mathrm{mM}$, corresponding to a Nernst potential of $\approx 42\,\mathrm{mV}$ at room temperature, measured as the potential of the inner chamber relative to the outer chamber (grounded). These chosen concentrations result in peak voltage values which are closely aligned to those seen in neurons, while remaining practical to produce. Larger concentration differences can of course be used, but are more unwieldy and can lead to less stable membranes.

The salt solutions are made starting with dry KCl from Sigma-Aldrich (or any other salt), dissolved in DI water. HEPES is added at a concentration of 10 mM and the pH is brought to 7.0 using HCl and KOH. The interior solution (the lower of the two concentrations) has an additional 120 mM of sucrose added to minimize the osmotic pressure gradient across the membrane. Finally the solutions are filtered through $0.22\,\mu$m polyethersulfone filters from Fisher Scientific and stored at room temperature.

2.3 Electronics

The voltage in the system is controlled and monitored using a custom LabView 2014 program. The program communicates with the circuitry through a National Instruments DAQ adapter, and the circuitry in turn connects to the Teflon chamber via the AgCl electrodes. The main circuit is depicted in Fig. 2.2, it consists of a voltage clamping portion and a current measurement portion, with a corresponding electrode for each. The current is measured

by monitoring the voltage across the resistor R_F, which is then amplified by a factor R_1/R_2 before being output to the computer and converted into a current. The clamping is done by first choosing a desired clamp voltage V_c. The circuitry then compares the current voltage in the system, V, to V_c, and injects a current I_c proportional to the difference $(V - V_c)$ through the AgCl electrode. This process repeats until the voltage in the system is equal to V_c.

The distinct aspect of the electronic setup is the addition of the clamp resistor, R_c. In traditional voltage clamping experiments, the current sourced from the operational amplifiers is several orders of magnitude larger than other currents in the system. Thus the voltage clamp will correct any deviations from the desired voltage instantaneously, hence the voltage is "clamped" to the value set by V_c. The addition of a resistor before the electrode means that the output from the operational amplifier will instead be reduced by a factor proportional to the resistance. The value R_c is chosen such that the clamping current is roughly the same magnitude as the other currents in the system; the desired magnitude for I_c being larger than the leak currents but smaller than the channel currents. This allows for dynamics (i.e. action potentials) to occur in the system while still retaining control over the voltage when the channels are not active. The circuit also contains a switch to bypass R_c, which acts as a toggle between "current limited" mode (through R_c), and "voltage clamping" mode (bypassing R_c). This is useful for conducting more traditional electrophysiology experiments, such as measuring channel rates.

An auxilliary circuit for clamping the current is also present in the system, shown in Fig. 2.3. The role of this circuit is to inject constant current into the inner chamber, regardless of the voltage across the membrane. In practice this circuit is used in conjunction with threshold logic in Labview to connect two separate AA systems (2 cups) together. It injects a current in one well proportional to the voltage in the other, and is only used for experiments involving feedback (Ch. 6). The current clamp is completely modular and disconnected when

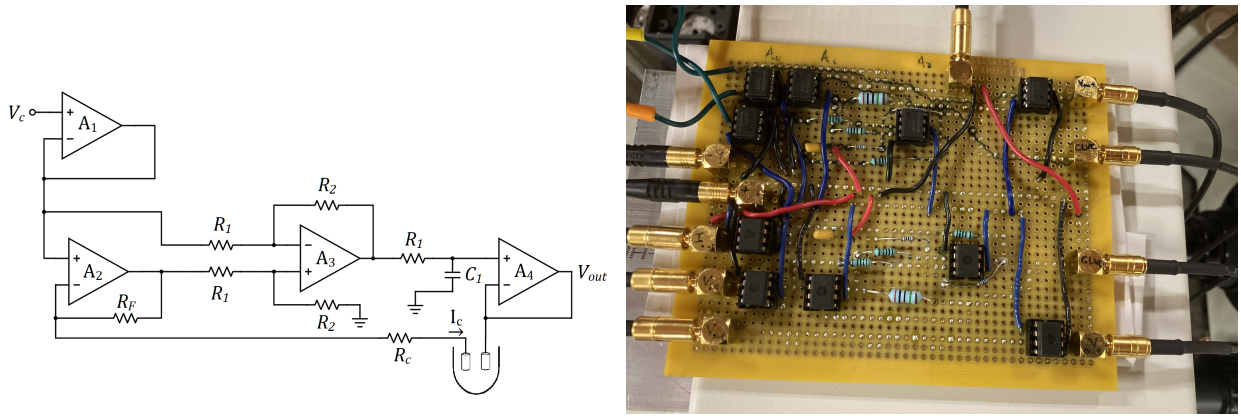

Figure 2.2: Current limited voltage clamp schematic (left), and circuit (right). All op amps are the TL071IP, with A_1 and A_4 being used as voltage followers. The values of the passive components are: $R_1 = 1\,\mathrm{k}\Omega$, $R_2 = 10\,\mathrm{k}\Omega$, $R_F = 20\,\mathrm{M}\Omega$, $C_1 = 0.1\,\mu\mathrm{F}$. The clamp resistance R_c is usually $2\,\mathrm{G}\Omega$, but can vary (see text). Two identical copies of this circuit are used in the experiment, one for each AA; they share a common ground with the extracellular side of the Teflon chamber, as well as with the computer which controls the experiment.

not in use. When it is in use, it outputs through the same AgCl electrode as the one used to measure the voltage. Thus there are always only two electrodes in the inner chamber (inside the cup).

2.4 Phospholipid Bilayer Membrane

The semipermeable lipid membrane is where the "action" occurs, analogous to the cell membrane in which ion channels are embedded in excitable cells. The lipid bilayer itself plays a surprisingly key role in the dynamics of the system, as studies have shown that channel kinetics depend on the lipid composition of the membrane itself [23]. In this work, the lipid chosen for membrane creation is 1,2-diphytanoyl-sn-glycero-3-phosphocholine ("DPhPC"), following previous lab work [21, 22]. DPhPC is purchased from Avanti Polar Lipids (dissolved in chloroform at $25\,\mathrm{mg/mL}$), and stored under N_2 gas in aliquots of $10\,\mu\mathrm{L}$ in borosilicate

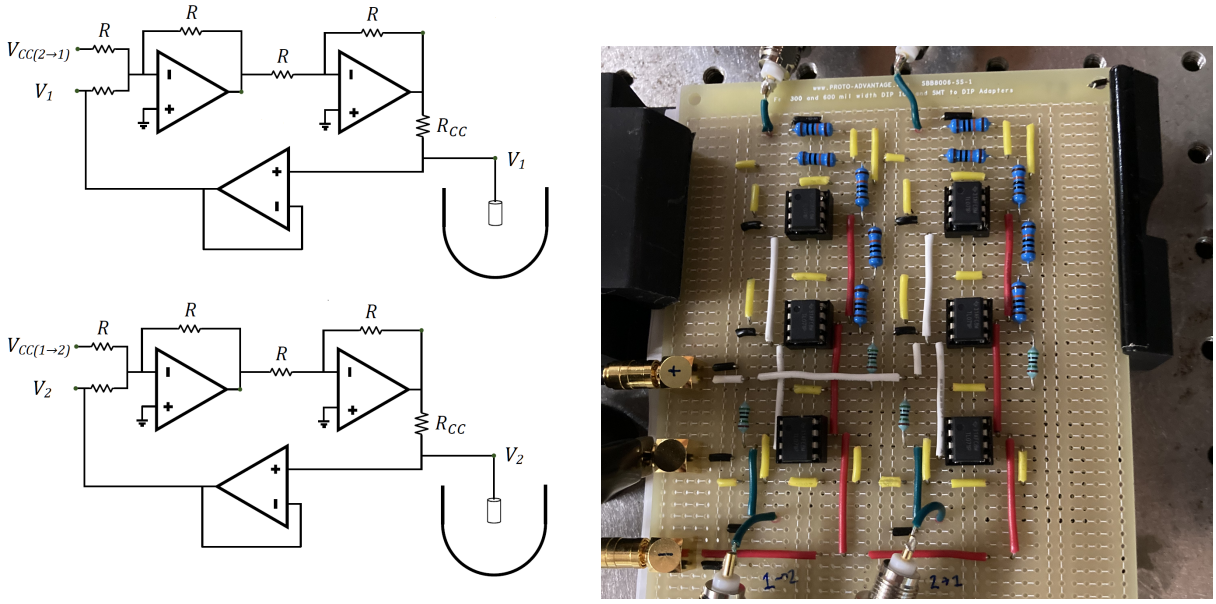

Figure 2.3: Current clamp schematic (left) and circuit (right). The clamp consists of two identical circuits, one for each AA. The current injected is $I_{CC} = V_{CC}/R_{CC}$, where V_{CC} the measured voltage in the "pre-synaptic" AA. All op amps are the TL071IP; the resistances are: $R = 100\,\mathrm{k}\Omega$, $R_{CC} = 100\,\mathrm{M}\Omega$.

glass vials at -20°C until ready to use. To create the membrane, the DPhPC is pipetted onto the hole ("aperture") in the plastic cup in a series of steps, and a pipette is used to "paint" the membrane. The following describes how to prepare DPhPC for use in painting the phospholipid bilayer:

To begin, an aliquot of DPhPC (10 μL in a glass vial) is removed from the fridge and dried under a steady stream of N_2 gas for 10 minutes to evaporate the chloroform. Then, 250 μL of pentane (C_5H_{12}) is added to the vial using a Hamilton glass syringe, and the contents are dried again with N_2 for another 10 minutes. This is to further remove any residual chloroform, the presence of which significantly and negatively impacts the stability of the lipid membranes. After the second stage of drying, DPhPC should be visible as a ring at the bottom of the glass vial. The vial is attached to vacuum for further drying, again to remove residual chloroform. The lipid can be held under vacuum for up to a week, but sufficient chloroform removal should be reached after 30 minutes or so. Once removed from the vacuum, 12.5 μL of decane ($C_{10}H_{22}$) is added to the vial via syringe to dissolve the DPhPC at a concentration of 20 mg/mL. The solution is shaken by hand to mix, and a very small amount of the decane-lipid mixture is dripped onto the aperture of the plastic cup(s), again with a syringe. It is sufficient to wet only the immediate area around the aperture. The cup(s) are placed under vacuum for 30 minutes to dry the decane, starting the vacuum at low power as to prevent the decane from being violently pulled off the cup. This layer of dry decane around the aperture creates a hydrophobic surface which supports the formation of a bilayer in the aperture. Once sufficiently dried, the cup(s) are placed into the Teflon chamber, which is then flooded with the relevant solution (e.g. KCl). Once the cup(s) are immersed in solution, a small amount of the decane-lipid mixture is pipetted directly above the aperture. The viscous decane will naturally flow from the pipette and sit on top of the aperture, sealing it and preventing the diffusion of ions. Proper sealing can be confirmed by monitoring the voltage (an unsealed or improperly sealed aperture will lead to a voltage

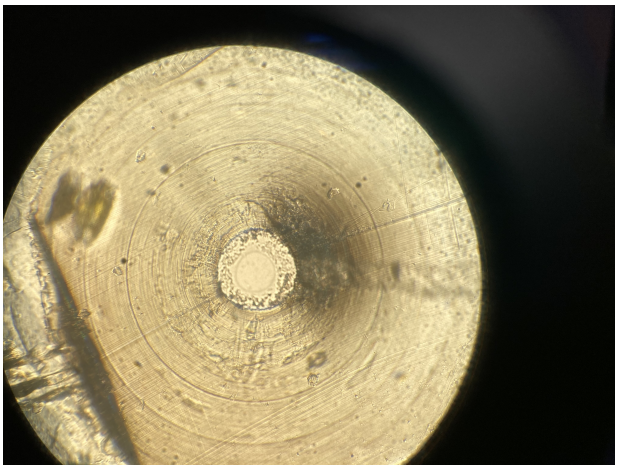

Figure 2.4: Lipid bilayer (center) surrounded by decane, viewed from below through the optical microscope.

reading of $\approx V_N$, whereas a proper seal will allow the current from the voltage clamp to keep the voltage steady at V_{clamp}). To paint the lipid membrane, an empty pipette is inserted into the inner chamber and placed near the aperture. A small bubble is formed at the tip of the pipette by a partially pressing on the plunger; the bubble will attract nearby decane to it. The bubble is carefully maneuvered near the aperture to slowly peel away decane from the area. Once a sufficient amount of decane is removed from around the aperture, the lipid in the area will spontaneously form into a bilayer membrane, which has a distinct sheen in the microscope's view. The creation of the membrane can also be confirmed electronically as it has a different capacitance than the decane-lipid mixture. The thickness of the lipid bilayer is $\sim 4\,\text{nm}$.

Once the membrane is painted, it is ready for the insertion of ion channels. The stability of the painted membrane is affected by a number of factors, the dominant one being the hydrostatic pressure. It is essential to minimize the pressure difference in the system before painting a membrane by making sure that the solution level of the inner and outer chambers are as close as possible. The horizontal orientation of the membrane means that differences

in pressure lead to a force on the membrane, which can cause it to "burst" (violently come apart). The simplest way to ensure the intracellular and extracellular solution levels are equal is to simply leave the aperture of the cup unsealed for a few minutes after flooding the chambers. The solutions will equilize during this time, while the change in ion concentration due to diffusion through the aperture will be very small.

Other effects which can burst the membrane include large mechanical disturbances, e.g. sudden movements of the chamber; or sudden capacitive spikes, e.g. interrupting the power supply to the operational amplifiers. A membrane that is undisturbed and has no channels inserted is quite stable, with a life time depending on the size and the shape of the aperture which it sits upon. Larger and less uniform apertures tend to be less stable compared with smaller and/or uniformly round apertures. Membranes will tend to shrink over time as the surrounding decane slowly collapses inward, and eventually will either be completed buried by decane or destroyed by a bursting event. If a membrane is destroyed in any way, it can be repainted by the same method as before, and typically there will be no adverse effects. Once ion channels have inserted into a membrane, the stability tends to decrease due to the large amount of current flowing through it, though this is not always the case. In addition, membranes that are destroyed and repainted after channels are inserted tend to have large "leaks", in that the voltage will rapidly fluctuate and be difficult to control via the voltage clamp.

2.5 The Ion Channels

Once the electronics are connected, the chamber is immersed in solution, and the lipid membrane is painted, ion channels are ready to be inserted into the system. Channels are removed from storage and brought to room temperature by the warmth of the hand.

They are very briefly sonicated and then mixed with a pipette. To insert, a small amount of channels ($\sim 0.1\,\mu$L) is drawn with a pipette and brought as close to the membrane as possible before being gently injected into the solution. The injection must be done very carefully to minimize mechanical disturbances to the membrane. Channels will diffuse into the solution and (may) eventually insert into the membrane. The process of insertion is stochastic and can be instant or take more than 30 minutes. Successful insertion of channels is confirmed by monitoring the voltage recordings in LabView. Insertion events typically lead to fluctuations in voltage, while proper activity of the channels can verified by various experimental protocols, depending on the specific channel.

2.6 Action Potential

Starting with the voltage clamped below threshold, a the simplest test to check if channels are inserted and working is to raise the voltage clamp above threshold and monitor the results. The occurrence of an action potential signifies that a sufficient number of channels have inserted into the membrane. A typical voltage trace which confirms the insertion of channels is shown in Fig. 2.5.

2.7 Gel stabilized system

The stability of the AA system can be increased by encasing it in a hydrogel to further support the lipid bilayer. Preparations are based on [24] and [25]: 8 g/100 mL poly-ethylene glycol dimethacrylate (PEG-DMA) and 0.8 g/100 mL Irgacure 2959 UV photo initiator (2-hydroxy-4'-(2-hydroxyethoxy)-2-methylpropiophenone) are dissolved in the usual KCl solution in which experiments are conducted. Once a membrane is painted, 365 nm UV light is shone directly at the intracellular side (inside the plastic cup) for 90-120 s to solidify the gel. Once gelled, the membrane is much more resistant to mechanical and electrical stress and

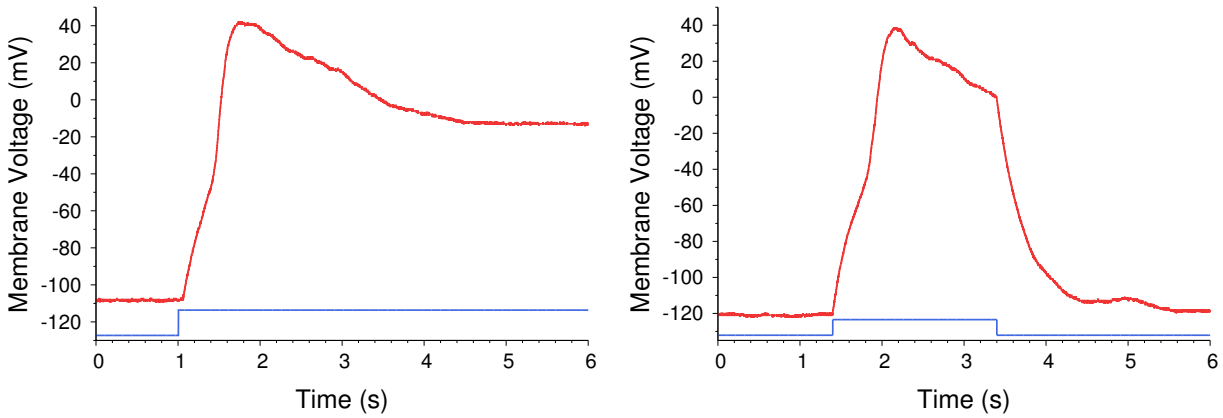

Figure 2.5: Archetypal time course of the membrane potential when eliciting action potentials in the Artificial Axon (red). The CLVC protocol used is shown below (blue, not to scale), either a step (left) or a pulse (right) which causes the voltage to exceed the threshold for firing will produce an action potential.

lasts much longer (>24 hrs, compared to 0-4 hrs for a typical preparation with no gel).

Due to the horizontal orientation of the bilayer membrane in the current setup, the gelled membranes can be harder to work with compared to vertical setups. The reason being the fluctuating hydrostatic pressure in combination with the fact that the lipid membrane must bear a load. Currently there have not been any successfully attempts of inserting channels into a gelled membrane. One technique which improves the success rate of the method is to put an additional support cup under the usual cup containing the intracellular solution. This gives the gel below the membrane a support structure, rather than having it free floating in solution. An issue with the gel method with the current materials is that the UV light seems to degrade the cups, preventing repeated use with the gel setup.

2.8 KvAP

The AA serves as a minimal system for eliciting of action potentials. In principle this means that any ion channel which can insert into a phospholipid membrane can serve as the active component of the system. However, identifying suitable channels can be a difficult task, and producing them even more so. The ion channel used in all experiments described in this work is KvAP. The channels are produced in the lab in a difficult but well known process. The next few sections will describe the step by step procedure for producing KvAP in explicit detail. This is worth highlighting since quality of the channels plays an enormous role in determining the outcome of the experiments. Many experimental limitations and failures have been due to the quality (or lack thereof) of the produced channels.

The starting ingredient is the wild-type KvAP gene in pQE-60 vector, which was gifted to Zocchi lab by the Roderick MacKinnon group. This wild type was then modified via site-directed mutagenesis by predecessors in the lab [21]. Specifically, a point mutation was performed at site 247 of the plasmid to change a single thymine (T) to an adenine (A). This changes the amino acid starting at site 247 from a cysteine (TGC) to a serine (AGC). The desired effect is to make aggregation of the proteins less likely by removing the capability to form a disulfide bond. All steps described below start with the mutated plasmid. It should be emphasized that KvAP production is extremely sensitive and small changes may have a large effect on the final yield.

2.9 Expression of KvAP in *E coli.*

Starting with the mutant KvAP plasmid, the first step is to incorporate it into *E coli.* and have them express the protein in large amounts. This is a slow biological process, achieved over the course of three days, known as "expression". Items marked (sterile) must be done near an open flame with sterilized pipettes to prevent undesired bacteria from being

introduced into the system.

2.9.1 Day 1

1. Prepare 10mL of stock ampicillin solution, using deionized H_2O and powdered ampicillin at a concentration of 1 g/mL. Store at 4°C for use throughout the procedure.
2. Pre-chill empty 1.5 mL vial.
3. Pre-heat SOC medium to 42°C and incubator to 37°C.
4. Thaw XL1-Blue Supercompetent Cells (Agilent) along with a vial of β-mercaptoethanol (βME) in ice.
5. Thaw KvAP plasmid on ice.
6. (Sterile) Aliquot 60-100 μL of cells to chilled 1.5 mL vial, along with 1.7 μL of βME.
7. Incubate mixture on ice for 10 minutes, gently swirling it by hand every 2 minutes.
8. (Sterile) Add 50 - 200 ng of KvAP plasmid to the aliquot of cells. Gently swirl to mix and let incubate for 30 minutes.
9. Heat shock the mixture in 42°C water bath for 45-60 seconds. Afterward immediately incubate the mixture on ice for 2 minutes. The duration of the heat shock and icing afterwards must be precise, and are essential for successful transformation.
10. Add 0.9 mL of pre-heated SOC medium to cell mixture and incubate for 1 hour at 37°C, with shaking at 375 rpm.
11. (Sterile) Use glass rod to spread 150 μL of the cell mixture onto pre-made agar plates (LB agar, Ampicillin, pH 7.0) along with 20 μL of 100 mg/mL ampicillin.
12. Incubate plates with agar side on top for 17 - 20 hours at 37°C

13. Prior to day 2, prepare flasks of LB broth solution using 25 g/L of LB broth (Fisher Scientific) mixed with DI water. Seal with aluminum foil and autoclave at 250°F for 45 minutes. Allow ample time to cool at room temperature. Autoclaved and sealed broth can be made 1-2 weeks before use, the usual amount is $5 \times 1\,\text{L} + 4 \times 0.5\,\text{L} = 7\,\text{L}$.

2.9.2 Day 2

1. (Sterile) Check agar plates to ensure separated colonies have formed. Alternatively, thaw glycerol stock of *E coli.* on ice (see step 10 of day 2).

2. Using an open flame, sterilize three glass tubes and enough aluminum foil to cover each tube.

3. (Sterile) Pipette 5 mL of LB broth, followed by 5 μL of ampicillin, into each glass tube.

4. (Sterile) If using colonies, use a pipette to scoop one colony into each tube; if using glycerol stock, aliquot 25 μL of the stock in each tube after it is fully thawed. Mix each tube with a pipette.

5. Cover each tube with sterile aluminum foil and shake at 37°C and 250 rpm for 4-5 hours.

6. After 4 hours, check the contents of the glass vial by mixing with a sterile pipette. The cloudiness of it indicates the amount of cell growth.

7. (Sterile) If cell growth is sufficient and no foreign substances are in the vial, select one glass tube and pour contents into a flask of 1 L LB broth. Discard remaining tubes, or keep for future use (see step 10).

8. (Sterile) Add 1 mL of ampicillin to the flask of LB broth which has the *E coli.*.

9. Incubate at 37°C and 220 rpm for 14 - 18 hours.

10. (Optional) Leftover *E coli.* can be frozen and stored for future use. Mix DI H_2O and glycerol in a 1:1 solution (750 μL total if using a 1.5 mL tube) and vortex vigorously to mix. This mixture can then be mixed 1:1 again with *E coli.* solution (i.e. 750 μL of *E coli.* for a 1.5 mL tube). Vortex again and store at -80°C. Glycerol stock can be used in place of agar plate colonies, in which case expression starts at step 1 of day 2.

2.9.3 Day 3

1. (Sterile) Check the optical density (OD) of the broth by taking a 1 mL sample from flask with *E coli.* after incubating for 14-18 hours. Dilute either 2x or 3x with broth from an unopened flask. Take a sample of pure broth of the same volume to use as a blank.

2. Use a spectrometer to check OD at a wavelength of 600 nm. First measure the pure broth as blank, then the sample. The actual OD is the result on screen multiplied by the dilution factor. Target OD range is a minimum of 0.6 - 0.8, but in practice it may be higher.

3. (Sterile) If target OD is reached, aliquot *E coli.* broth to the other flasks such that each flask has an OD of 0.1, using the following formula:

$$C_1V_1 = C_2(V_2 + V_1) \rightarrow V_1 = \frac{0.1 * 1000\,\text{mL}}{C_1 + 0.1}$$

   where V_1 is the volume to add to each 1 L flask (half for the 500 mL flasks) and C_1 is the measured OD.

4. Prepare 17.1 g of $BaCl_2$ in 66 mL of DI H_2O, resulting in 17.1 g/≈70 mL = 1 M $BaCl_2$. Ensure that the $BaCl_2$ is fully dissolved by slightly heating and vortexing the solution.

5. (Sterile) Add 1 mL ampicillin to each 1 L flask and half that for each 500 mL flask.

6. (Sterile) Add 10 mL of 1 M $BaCl_2$ per 1 L of broth for each flask for a concentration of 10 mM $BaCl_2$ in each flask. This helps slow the toxicity of the channels from affecting the *E coli.* Procedures vary on whether to add the barium here or when adding the IPTG, from trial and error it seems more effective to add it at this stage.

7. Shake flasks in incubator at 37°C and 220 rpm for about 4 hours.

8. Prepare a 1 M solution of IPTG by dissolving 1.192 g of IPTG in 5 mL final volume of DI H_2O. "IPTG" is isopropyl β-d-1-thiogalactopyranoside which induces the expression of KvAP in the *E coli.*.

9. After ≈4 hours, check OD of flasks via the same method as step 1 of day 3, if OD is 0.6 - 0.8 or greater, proceed. Otherwise, continue to shake and check periodically, but do not exceed 5 hours of incubation.

10. (Sterile) Aliquot the appropriate amount of 1 M IPTG solution to each flask such that the final concentration is 0.4 mM, using the same formula as step 3 of day 3. The amount is usually around 400 μL for the 1 L flasks.

11. Shake for another 4 hours at 37°C and 220 rpm. Do not exceed as 4 hours as KvAP is toxic to *E coli.* and the produced protein will degrade in quality over time.

12. Pour *E coli.* into centrifuge bottles, weighing the bottles with a scale to make sure that their weights are as close as possible. Centrifuge at 4000 rpm for 20 minutes (depending on the centrifuge's ramp up time, 22 - 24 minutes). All the *E coli.* will aggregate at the bottom of the bottles. Discard the supernatant and store the bottles at -20°C until ready to purify.

Name	Ingredients	Amount	Concentration	Notes
Tris-HCl (500 mL)	Tris H_2O	30.29 g to 500 mL	0.5 M -	Stock solution pH 8.0 + degas Store at RT.
KCl (500 mL)	KCl H_2O	37.28 g to 500 mL	1 M -	Stock solution Degas, store at RT.
DM (20 mL)	DM H_2O	4.826 g to 20 mL	0.5 M -	Centrifuge at 4000 rpm to remove bubbles. Store at 4°C.

Table 2.1: Stock solutions needed for making the necessary buffers for KvAP purification. All aqueous solutions are made with "NanoPure H_2O", which is DI water free of DNase and RNase, purchased from Fisher Scientific. pH is adjusted using stock HCl and 5 M KOH. Degassing is done by putting the buffer under vacuum with a loose cap until no bubbling occurs. DM is "n-Decyl-β-D-maltopyranoside", a detergent and a key ingredient which is needed to shield the proteins during the purification process. High quality (purity) DM is essential for successful production of the final product.

2.10 Purification and Reconstitution of KvAP

Once KvAP has been successfully expressed, the next step is to extract it from the *E coli.* and remove the unwanted portion (i.e. everything other than KvAP). This process is termed "purification". Following that is "reconstitution", the process in which the KvAP obtained from purification is encapsulated in small unilamellar vesicles (SUVs) to keep them stable and ready to use in experiment. Tables 2.1 and 2.2 list buffers and other solutions which are necessary for purification and reconstitution. They are listed with recommended volumes and target concentrations. It is best to make these before proceeding (if permitted), as some of the steps involved in purification and reconstitution are time sensitive.

Name	Ingredients	Amount	Concentration	Notes
Lysis Buffer (50 mL)	Tris-HCl KCl Lysozyme DNase β-ME (14 M) PIC H_2O	5 mL 5 mL 10 mg 10 μL 7.4 μL 1 tablet to 50 mL	50 mM 100 mM 0.2 mg/mL 2 μg/mL 2 mM - -	Needed at start of day 4. Must be freshly made. Need 2x50 mL for large yields. "PIC" is protease inhibitor cocktail.
Wash Buffer (50 mL)	Tris-HCl KCl DM Imidazole (1 M) H_2O	2 mL/5 mL 5 mL 0.5 mL 1 mL to 50 mL	20 mM/50 mM 100 mM 5 mM 20 mM -	Make before day 5. Can store at RT if DM not added until before use.
Elution Buffer (50 mL)	Tris-HCl KCl DM Imidazole (1 M) H_2O	2 mL/5 mL 5 mL 0.5 mL 20 mL to 50 mL	20 mM/50 mM 100 mM 5 mM 400 mM -	Make before day 5. Can store at RT if DM not added until before use.
HPLC Buffer (500 mL)	Tris-HCl KCl DM H_2O	20 mL 50 mL 5 mL to 500 mL	20 mM 100 mM 5 mM -	pH 7.5 + degas Add DM after pH and degas. Lasts 2-3 expressions.
RC Buffer (500 mL)	KCl HEPES H_2O	22.5 mL 0.119 g to 50 mL	450 mM 10 mM -	pH 7.4 + degas Make before day 5 Store at RT

Table 2.2: Buffers needed for purification and reconstitution of KvAP. Water, pH, and degas requirements are the same as the stock solutions (see Table 2.1).

2.10.1 Day 4

1. Ensure that all buffers needed for the day are prepared. Lysis buffer must be freshly made to ensure the potency of the protease inhibitor cocktail. The usual amount of *E coli.* produced from expression usually requires > 50 mL of lysis buffer.

2. Thaw *E coli.* on ice. Dissolve *E coli.* in lysis buffer by pouring the buffer into the centrifuge containers and gently shaking by hand. Alternatively, shake in the incubator at low rpm and at a low temperature.

3. Use Emulsiflex to lyse the *E coli.*. A pressure of 15,000-18,000 psi is required to lyse the cells (exceeding this pressure is not beneficial). Running the *E coli.* through 2 - 3 times is sufficient. Store lysate in 50 mL polypropylene conical tubes.

4. Immediately add DM to lysate for a DM concentration of 40 mM. Unprotected KvAP in aqueous solution will quickly aggregate and lose its function. Keeping the lysate at lower temperatures (via ice) can also help slow KvAP degradation.

5. Rotisserie lysate for 3 hours (on low, $\sim$25 rpm) in a low temperature room, if possible. The gentle mixing allows time for DM to bind to all the free roaming KvAP within the lysate.

6. Centrifuge 50 mL vials of lysate at 10,200 rpm for 1 hr. Most of the unwanted cell debris is centrifuged out while the supernatant contains the KvAP encapsulated in DM. This step can be done at even higher rpm for better results, depending on the capability of the centrifuge being used.

7. Prepare 2 - 3 mL of cobalt beads (Takara) in a chromatography column. A larger amount of beads will lead to a higher yield, but may pick up unwanted particles.

8. Wash cobalt beads 3x with 8 mL of wash buffer and drain. Evenly transfer the beads into the 50 mL tubes of lysate after centrifugation has completed. Rotisserie for another

1.5 hours. The KvAP are his-tagged (i.e. six histidines are attached at the end of the protein) and will bind to the cobalt beads during this time.

9. Run lysate through chromatography column to collect beads. This must be done multiple times to collect all the beads, as they will stick to the side walls of the vials. As the beads are collected the lysate also has more time to flow through the beads, allowing for further protein binding to the beads. This process can be very slow, but more repetitions lead to higher yields.

10. Wash the cobalt beads again with the remain wash buffer while disturbing them (shake column or use pipette). Allow the beads to settle and drain the wash buffer.

11. Elute the KvAP by adding 12 - 14 mL of elution buffer very slowly to the chromatography column while disturbing the beads. Most of the KvAP should elute from the first milliliter of elution buffer ("first elute"). A sample can be taken from the first one or two elutes for troubleshooting.

12. Perform a Bradford Assay by mixing 40 μL of eluted solution together with 760 μL of pre-diluted "Protein Assay Dye Reagent Concentrate" from Bio-Rad. The sample should turn from reddish to blue to indicate the presence of protein (KvAP), with darker blues indicating more protein.

13. Mix the assay sample via pipette, and extract 200 μL for spectroscopy at 595 nm, together with 200 μL of dye with no protein in it (blank). Record ODs and calculate the yield mass by comparing the OD of the blank to the OD of the sample.

14. Yield mass can vary despite careful adherence to protocols listed up until this point. In general yield must be at least 2 mg, otherwise there isn't enough to proceed as more will likely be lost during further purification and reconstitution.

15. Pipette in 1.5 units of thrombin per milligram of yield mass. Thrombin is used to cleave away the his-tag, which is no longer of use. Leave eluted solution overnight

at 12°C in incubator. The low temperature slows the activity of thrombin. Optimal time to allow for cleavage varies with thrombin concentration and temperature. From experience, 16 hrs at 12°C seems to work well.

16. Dry 250 μL of 25 mg/mL DPhPC (1,2-diphytanoyl-sn-glycero-3-phosphocholine, Avanti Polar Lipids) under N_2 gas for 10 minutes. Add 250 μL pentane and dry for another 10 minutes. Then leave attached to vacuum to dry overnight.

2.10.2 Day 5

1. Ensure that the HPLC is maintained and properly working prior to proceeding.

2. Make DM in RC if no previous stock is available. This is DM made as per Table 2.1, except with RC (reconstitution) buffer instead of water as the solvent. Because only a small amount is needed, it is usually made in 1.5 mL tubes and as a result it can be difficult to get precisely 500 mM. This can be adjusted for in the step where it is needed, so there is no need for high precision. Once made, DM in RC can be stored at 4°C as stock solution for future expressions.

3. Remove eluted protein with thrombin from the incubator and place in 4°C fridge as needed to further slow thrombin activity once 16 hours has been reached.

4. The next step is to run the eluted proteins through the HPLC for further purification, while also preparing vesicles for reconstitution. These two processes must be performed such that they are completed as close to simultaneously as possible. Typically the vesicles take longer to make, while the HPLC requires more attention.

2.10.2.1 HPLC

5. Centrifuge the eluted solution from day 4 at $5000 \times g$ for 2 - 5 minutes at a time to reduce volume down to $< 2\,\mu$L, using a 50 mL filtered conical tube. It is **essential** that

care be taken to properly mix the solution after each centrifuge step, as the protein will tend to aggregate at the bottom. This is an extremely important step, not doing so will lead to significantly lower yield.

6. Once the eluted solution is below 2 μL, load into HPLC using a 2 μL syringe, taking care not to introduce bubbles into the HPLC column. (Note: One untested but promising alternative to improve yield is to load the eluted solution into the HPLC several times. This means that the solution would not have to be condensed into a $< 2\,\mu$L volume, which from experience is a key step that causes a lot of loss. This would take a longer time as the capacity of the HPLC is only 2 μL, so multiple loads would mean multiple HPLC runs, each taking 25 - 50 minutes.)

7. Run solution through the size exclusion HPLC column at 0.5 mL/min, collecting the fracs which fall under the large 280 nm/260 nm peak (typically fracs 11 - 14). This typically occurs $\approx$12 minutes into the process.

8. Combine fracs and perform another Bradford Assay (day 4 step 12) on the solution to find the post-HPLC yield. There will typically be a loss of 30 - 50% compared to the yield from the end of day 4.

9. Based on the yield from the assay, centrifuge the channels at 7500 $\times$ g in 15 mL filtered conical tubes for 4 - 8 minutes total, in steps of 1 - 2 minutes at a time, to reduce to a concentration of $\sim$10 μg/mL. For a typical yield this results in a final volume of around 150 - 250 μL. Once again it is **essential** to mix solution between each centrifuge run so that the channels do not all clump at the bottom.

10. Once the solution is near the target concentration, place in 4°C fridge until vesicles are also finished.

2.10.2.2 Vesicles

11. Resuspend previously dried DPhPC using RC buffer to a DPhPC concentration of 20 mg/mL. (312.5 μL of RC buffer for 250 μL of dried DPhPC at 25mg/mL.)

12. Gently shake to dissolve all the lipid into the solution. The solution will be turbid, use vortex mixer on the lowest setting to further mix for no more than 10 minutes. The resulting solution should become "milky" (white and opaque). Vortexing the solution too long causes it to be unworkable in terms of creating SUVs.

13. Prepare ice cold water in the sonicator, filling up to $\sim$25% of operational level. There are various water levels which yield "resonance" that is not achieved at full operational levels. It is vital that the sonication strength is large to allow for the breakdown of large lipid vesicles into smaller ones. Wrap vial of DPhPC suspended in RC buffer in parafilm, and submerge only the portion of the vial containing the buffer into the sonicator and begin sonicating. Take care to find a spot of maximum sonication strength. Sonicate until the solution clears up and becomes a translucent blue. This may take anywhere from 5 minutes to $>$ 8 hours, or never at all. The more translucent the solution, the more confirmation there is that the solution is made up of small unilamellar vesicles, which are key for encapsulating the ion channels. During this process, it's also essential that the water is constantly replaced with cold water, as the sonication process heats up the water and DPhPC undergoes a transition at higher temperatures which prevents it from ever forming SUVs.

    This step is extremely important and not easily replicable, depending on several factors. Many attempts were made to standardize this, but issues remained with consistency of results. The above description is the latest method which yielded usable channels, further modifications may lead to improved results.

14. Once the solution is sufficiently translucent, check the final volume again with a Hamilton syringe. Add DM in RC for a concentration of 10 mM DM, mix and rotate gently

for 30 minutes.

15. Place in fridge until HPLC step is also complete.

16. Ideally, the HPLC procedure should finish at the same time as the vesicles, i.e. the channels are eluted from the HPLC just as the 10 mM DM/lipid solution have been mixed for 30 minutes. If simultaneity cannot be achieved, it is preferable if the HPLC step is finished later, as it's best to avoid having the channels be at low volumes as much as possible.

17. Once both vesicle and HPLC steps are completed, the two solutions must be combined along with an additional amount of DM in RC for a final DM concentration of 17.5 mM. The amount of vesicle solution, V_{lipid}, depends on the desired mass ratio of lipids to channels. The following formulae help determine the amount of each solution to use:

$$n = \frac{V_{lipid} \times C_{RCDM}}{M_{channels}}$$

where C_{RCDM} is typically 20 mg/mL as per step 11 of day 5, and $M_{channels}$ is obtained from step 8 of day 5. V_{lipid} is recommended to be the entirety of it (total lipid mass should be 6.25 mg if there is no loss from sonication), as based on experience a slightly higher mass ratio ($n \sim 10$) produces better results. Meanwhile, to determine the amount of DM in RC to add:

$$17.5\,\text{mM} = \frac{5\,\text{mM} \times V_{channels} + 10\,\text{mM} \times V_{lipid} + C_{RCDM} \times V_{RCDM}}{V_{channels} \times V_{lipid} \times V_{channels}}$$

where C_{RCDM} is the concentration of the prepared DM in RC, and V_{RCDM} is the required amount.

18. Once combined, allow solution to sit at room temperature for 2 hours, gently mixed by hand every 20 minutes, or alternative placed on a gentle rotator for the entire duration.

19. Scoop out roughly 60 - 100 mg of Bio-beads (BioRad) into four separate 1.5 mL centrifuge tubes. Thoroughly wash the beads three times each with ethanol, then wash again three times with NanoPure water, and finally three more times with RC buffer. Leave the beads submerged in RC buffer and label the tubes "1", "2", "3", "4" in approximate order of most beads to least.

20. Degas beads in vacuum chamber. This can get messy as beads tend to "jump" out of tubes as gas is removed from the RC buffer. Loss can be minimized by partially closing the caps on the tubes. Store at 4° after degas until ready to use.

21. Prepare three spin desalting columns (Zeba, Thermo Scientific) in the centrifuge, following the instructions on the packaging. Take care to mark the side that faces outward.

22. After the channels/lipid mixture has been allowed to mix at room temperature for 2 hours, pipette the mixture into the desalting columns one by one and centrifuge. The mixture should be clear before desalting, and if done correctly, they should remain clear after desalting. An opaque/cloudy mixture after desalting indicates that something went wrong, and the channels most likely will not be fully functional.

23. After desalting, remove the RC buffer from the first tube of beads (labeled "1") and carefully pipette all channels into the tube, taking care to mix the solution with a pipette before transferring. Place tube back into fridge on its side to maximize the exposed surface area of the beads and allow to rest for 12 hours.

24. Repeat the previous step three more times, cycling through all four tubes of beads over the course of 48 hours. Thoroughly mix solution before transferring to new tube. This is the final step to remove any remaining DM from the solution, and allows the channels to migrate into the lipids. If anything has gone awry (most likely at sonication step, i.e. the formation of SUVs), then the solution may become cloudy or turbid during these 48 hours.

25. After the channels have been allowed to rest in the fourth and final tube for 12 hours, the production process is complete, and channels can be flash frozen and stored until ready to use.

2.11 Storage and Handling of KvAP

The KvAP channels must be flash frozen and stored at -80°C to maintain their function in the long term. To flash freeze, split the produced channels into 10-15 μL aliquots and dip into into liquid nitrogen for 30 - 45 seconds. Ensure that the entirety of the aliquot is submerged. After the liquid nitrogen bath, promptly store in a -80 °C fridge until ready to use. When removed from the fridge for an experiment, channels are thawed at room temperature by hand and briefly sonicated and mixed with a pipette before use. Channels stored at -80°C can maintain function for at least 18 months.

CHAPTER 3

Model

The Artificial Axon generates action potentials using a single species of voltage gated potassium ion channels (KvAP) as the active ingredient. With the archetypal Hodgkin-Huxley (HH) and Morris-Lecar (ML) models as a basis, this chapter will discuss the formulation of a minimal 3D model for the AA dynamical system. The model satisfies two key criteria: it describes the dynamics of the physical AA accurately, i.e. produce results which are in agreement with the experiment; and it is simple enough such that it lends itself to analysis as a dynamical system (Ch. 5), i.e. it has a minimal amount of dimensions in parameter space.

3.1 Membrane Voltage

In biological systems, electrical excitations typically occur in the membranes of excitable cells [8]. Accordingly, the starting point for describing the dynamics of the Artificial Axon is the equation for the transmembrane potential, i.e. the voltage across the phospholipid bilayer. Like the cell membrane, the lipid bilayer in the AA is sandwiched between two conducting media which are the electrolytes (KCl) on either side, and acts as the dielectric of a parallel plate capacitance. In these conditions the region is mathematically analogous to the charging of a capacitor. For the AA, this capacitance is charged by two kinds of ionic currents: the current through the voltage gated ion channels embedded in the membrane, and the current injected by the AgCl electrodes of the current limited voltage clamp. The relation between these charging currents and the potential of the membrane is given by:

$$C\frac{dV}{dt} = I_{channels} + I_{clamp} \tag{3.1}$$

The charge carriers for $I_{channels}$ are K^+ ions, and for I_{clamp}, Cl^-, Ag^+, and all other ions in solution. Dividing through by C, and substituting in V/R for each current, an equation for the voltage across the membrane is obtained:

$$\frac{dV}{dt} = \frac{N_0\chi}{C}\left(p_o(t) + \chi_\ell/\chi\right)\left[V_N - V(t)\right] + \frac{1}{RC}\left[V_c - V(t)\right] \tag{3.2}$$

The first term in Eq. (3.2) corresponds to the channel current, with driving force proportional to $[V_N - V(t)]$, V_N being the Nernst (reversal) potential for the potassium ions:

$$V_N = \frac{kT}{|e|}\ln\left(\frac{[K^+]_{out}}{[K^+]_{in}}\right) \tag{3.3}$$

where $|e|$ is the charge of the K^+ ion, T the absolute temperature, k the Boltzmann constant (at room temperature, $kT/|e| \approx 25\,\mathrm{mV}$), and square brackets denote concentration. The other parameters are N_0, the number of functional ion channels embedded in the membrane; C, the membrane capacitance; χ, the conductance per open channel; χ_ℓ, the leak conductance, which is present even if the channel is closed ($\chi_\ell << \chi$); and $p_o(t)$, the probability that a channel is open at time t (or equivalently, the fraction of channels in the open state at time t, i.e. $N_0\chi\, p_o(t)$ is the total channel conductance).

The second term in Eq. (3.2) corresponds to the clamp current, with driving force proportional to $[V_c - V(t)]$. Here R is the series resistance of the CLVC, and V_c is the command voltage to the CLVC, which serves as the control parameter in the experiments. This clamp term is exactly equivalent to the presence of a second, reversed ionic gradient with Nernst potential equal to V_c and total leak conductance $\chi_c = 1/R_c$ [19, 26].

N_0	C	χ	χ_ℓ/χ	R	V_N	V_c
100	300 pF	170 pS	1/1000	2 GΩ	42 mV	−200 mV

Table 3.1: Typical experimental values for the parameters of Eq. (3.2), with V_c such that the system rests at V_r. The exact values of N_0, C, χ_ℓ and V_N will vary with each individual preparation of the AA.

In the case of KvAP, the channels are predominantly closed for large negative voltage values ($V \leq -120\,\mathrm{mV}$). As a result, if V_c is held at a large negative value, a steady state solution of Eq. (3.2) exists such that $V(t) = V_r$ is also large and negative:

$$V_r = \frac{N_0\chi_\ell V_N + V_{clamp}/R}{N_0\chi_\ell + 1/R} \tag{3.4}$$

The CLVC resistance R is chosen such that the clamp current is sufficient to pull the resting potential to negative values $V_r \sim -100\,\mathrm{mV}$ with channels closed, while also ensuring that $I_{current}$ with channels open can overwhelm the the clamp current so that the AA can fire. In terms of the parameters of the model, the requirement is $N_0\chi_\ell < 1/R \ll N_0\chi$.

Given parameter values usually observed in the experiments (Table 3.1), $V_r \approx -190\,\mathrm{mV}$, $I_{clamp} \approx 100\,\mathrm{pA}$, with characteristic time scales $C/(N_0\chi) \sim 10\,\mathrm{ms}$, $RC \sim 1\,\mathrm{s}$, and $C/(N_0\chi_\ell) \sim 10\,\mathrm{s}$ for the channels, clamp, and leak currents, respectively. Under these conditions, the system is in an excitable state; starting from the resting potential $V(t) = V_r$, a perturbation such as a positive input current or a step increase in V_c can cause the system to fire an action potential [27].

Equations of the form of Eq. (3.2) underlie many models of nerve excitability [28]. These are known as conductance based models, for the fact that the electrical excitability of the system is solely contained within the (voltage and time dependent) conductance terms [8].

In the case of the AA, there is the clamp conductance, a constant; a small leak conductance $N_0\chi_\ell$; and the channel conductance, $N_0\chi\, p_o(t)$. In other words, p_o, the channel opening probability, is the key term which determines the system's capability for generating action potentials, as well as the attributes of those generated APs. In general the probability $p_o(t)$ is specified by a set of rate equations which reflect the microscopic dynamics of the channels.

3.2 Channel Dynamics

There is some flexibility in the choice of model which determines the form of p_o. This choice can be informed by considering the progenitor HH model, which was devised by Alan Hodgkin and Andrew Huxley to explain their experimental findings in the squid giant axon [7]. More generally, the HH model provides a mathematical description for how action potentials are generated and propagated in the (commonly encountered) system of two ion species, sodium and potassium, which have opposing concentration gradients across the cell membrane. In this model, the conductance of sodium is given by the term $m^3h\bar{\chi}_{\mathrm{Na}}$, while the potassium conductance is described by $n^4\bar{g}_{\mathrm{K}}$. The form of these conductances were determined empirically to account for the excitable behavior they observed in the experiments. m and n are coefficients which represent the "open" probability of sodium and potassium channels, respectively, with the powers representing the number of sub-units which must be aligned ("open") for the channel itself to open. The coefficient h serves a similar purpose, but represents the inactivation sub-unit for sodium, which has an opposing effect compared to m and is completely independent of the opening and closing of the channel. These coefficients vary from 0 to 1, depending on the voltage, and multiply onto the maximum conductance of the channels $\bar{\chi}_{\mathrm{Na}}$ and $\bar{g}_{\mathrm{K}}$.

This model of the channel conductances proved to be quite successful, and subsequent

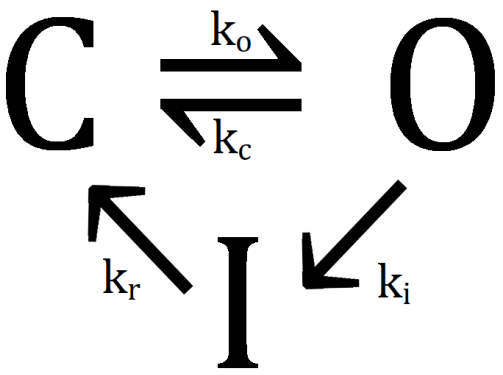

Figure 3.1: State diagram of the proposed model for the channel dynamics of KvAP. The channel is considered to have three states: open (O), closed (C), and inactive (I). The voltage dependent rates of opening (k_o), closing (k_c), inactivation (k_i), and recovery (k_r) move the system between these three states.

models have been largely based on the same principles [20, 23]. As such, a similar approach will be taken for the AA, while keeping the model as simple as possible. Knowing that the KvAP possesses an inactive state [23], the minimal model for KvAP channel dynamics consist of three states: open, closed, and inactive. The state diagram for the model is shown in Fig. 3.1. In order to minimize the dimensions of parameter space, the three states are connected with the fewest number of rates allowable. The main feature of this model is that the inactive state is accessed only from the open state and flows into the closed state. The unidirectional rates are strictly speaking unphysical, but represent a permissible approximation if the rates for the transitions $C \to I$ and $I \to O$ are small. The key advantage of a such approximation being the reduced number of parameters to consider. Note that a key difference with the HH model is that inactivation no longer independent of opening and closing.

In reality, the detailed channel dynamics are more complex than shown in Fig. 3.1, and models with more states and corresponding transition rates [23] have been formulated. However, the specifics of these microscopic details are not important for the descriptions of

action potentials that are the focus of the AA. In addition, a more complete description leads to the introduction of several more rates, i.e. an uncomfortable proliferation of the number of parameters in the model. Thus, the simplified model of Fig. 3.1 is employed with the assumption that these complications do not change the qualitative features of the system.

3.2.1 Rates

With the model defined, all that remains to complete the mathematical description of the system is define a form for the rates and relate them to Eq. (3.2). As KvAP is a voltage-gated ion channel, the rates at which the channels open and close, k_o and k_c, must also be voltage dependent. Considering the transition between states as a 1D barrier crossing process [7, 8, 23, 29], the rates are given Arrhenius form:

$$k_o(V) = \kappa\, e^{\alpha(V-V_0)} \qquad k_c(V) = \kappa\, e^{-\alpha(V-V_0)} \tag{3.5}$$

The parameters κ, α and V_0 (the "half-voltage", at which $k_o = k_c = \kappa$) are chosen to be symmetric, minimizing the number of parameters [20]. The rates of inactivation and recovery, k_i and k_r, are assigned similar forms:

$$k_i(V) = \kappa_i\, e^{\alpha_i(V-V_0^i)} \qquad k_r(V) = \kappa_r\, e^{-\alpha_r(V-V_0^r)} \tag{3.6}$$

From the state diagram, a set rate of differential equations can be written down for the time evolution of the probabilities p_o, p_i, and p_c. The condition that $p_o + p_c + p_i = 1$ reduces the number of equations needed to determine the system. Eliminating the closed state, the remaining rate equations are:

$$\begin{cases} \dfrac{dp_o}{dt} = (1 - p_o - p_i)\, k_o - p_o\, (k_c + k_i) \\ \\ \dfrac{dp_i}{dt} = p_o\, k_i - p_i\, k_r \end{cases} \tag{3.7}$$

where p_c is substituted with $(1 - p_o - p_i)$. Eqs. (3.7) are coupled to Eq. (3.2) through the voltage dependence of the rates, Eqs. (3.5), (3.6). Thus, Eqs. (3.2), (3.7) fully describes the AA with KvAP channels as a 3D dynamical system.

The 3D system can also be approximated as a 1D system in certain situations, by equating p_o in Fig. 3.2 with p_e, the "equilibrium" opening probability. The latter is purely a function of the voltage, reflecting the open - closed equilibrium of the channel in the absence of inactive states, whereas the former is also history (time) dependent. If channel dynamics are fast compared to all other timescales in the system, and if the inactive state is not present or not accessed, then the channel will always be in equilibrium with respect to the instantaneous voltage, and $p_o(t) \approx p_e(V)$. This is a useful approximation, especially when considering the dynamics at the threshold for firing (as inactivation does not play a role), and will be discussed further in Ch. 4.

The form of the term p_e is obtained by considering the opening rate for a two state system, i.e. the model of Fig. 3.1 with the inactive state removed. This is exactly equivalent to the coefficient n in the HH model. In this case, Eqs (3.7) reduces to an ordinary differential equation:

$$\frac{dp_e}{dt} = (1 - p_e)\, k_o - p_e\, k_c \tag{3.8}$$

with solution:

$$p_e(V) = \frac{k_o(V)}{k_c(V) + k_o(V)} = \frac{1}{1 + e^{-\frac{2q}{kT}(V - V_0)}} = \frac{1}{2}\left[1 + \tanh\left(\frac{V - V_0}{\gamma}\right)\right] \tag{3.9}$$

and so p_e has the form of a Fermi-Dirac distribution, where $q/(kT) = \alpha$ from Eq. (3.5) and V_0 is the same half-voltage. Also shown is an equivalent form commonly used in electrophysiology literature, with p_e in terms of the hyperbolic tangent [20] and $\gamma = kT/q$.

Eqs (3.2), (3.7) describes the dynamics of the physical AA well [26]. The model can be numerically simulated and used to probe how the AA responds under various conditions. Comparisons between time traces measured from the physical AA and ones obtained numerically from integrating the dynamical system will be presented in the following chapters. The parameter values used are obtained through a combination of measurements and fitting the experimental traces [26, 27]

3.3 Rates for the KvAP

3.3.1 Experimental Measurements

Rates for the KvAP have been reported before [23], however these previous measurements correspond to the states of a more detailed kinetic model for the KvAP (higher dimension in phase space, in order to account for the physical gating properties of the channels) which cannot be mapped onto Fig. 3.1. Thus, it is necessary to measure the "effective" rates Eqs. (3.5), (3.6) to determine the phenomenology of system with KvAP. In order to do so, a modified version of the AA is used in which the voltage is clamped in the traditional manner (i.e. $R_c = 0$). The experiments are then carried out in standard electrophysiological fashion [8, 23], using various voltage protocols and measuring the current to extract the rates.

3.3.1.1 Opening and Closing Rates

The opening and closing rates k_o and k_c of the model can be directly extracted from p_e through the equivalence in Eq. (3.9). Using the values obtained for p_e from previous work in the lab [18] and converting to the form of Eq. (3.5), the resultings rates are:

$$k_o(V) = 0.3\, e^{46(V+0.016)} \qquad k_c(V) = 0.3\, e^{-46(V+0.016)} \tag{3.10}$$

3.3.1.2 Measuring the Inactivation Rate

The protocol to measure k_i is as follows: the system is first held at a resting voltage $V_r = -120\,\mathrm{mV}$ where almost all channels are in the closed state. At $t = 0$ voltage is stepped up to $V_1 = 100\,\mathrm{mV}$, firing in the process, and held there for a time $t_1 = 100\,\mathrm{ms}$. At the end of this time interval most channels are open and only few are inactivated, since at V_1 the opening rate is faster than 100 ms and the inactivation rate considerably slower. At $t = t_1$ the voltage is dropped to a lower value V_2, held there for a time t_2 ($\sim 1\,s$). The value of V_2 is in the range between -80 mV and 0 mV, i.e. above threshold so that the channels start to inactivate but do not recover significantly. At, $t = t_1 + t_2 = \Delta t$, the voltage is stepped back up to $V_1 = 100\,\mathrm{mV}$ for a second firing. Finally the voltage is returned to the resting state V_r to begin another measurement.

The measured quantity is the clamp current (equal to the channel current if we neglect leak currents). The proportion of open channels at time t_1 (immediately before the voltage is stepped to V_2) is constant. While the system is held at V_2, some channels will inactivate with a rate $k_i(V_2)$, thus the second step to V_1 will elicit a smaller current than the first. The ratio of these two current peaks as a function of V_2 and t_2 allows us to extract the rate $k_i(V)$. Fig. 3.2 shows several current traces which illustrate the protocol.

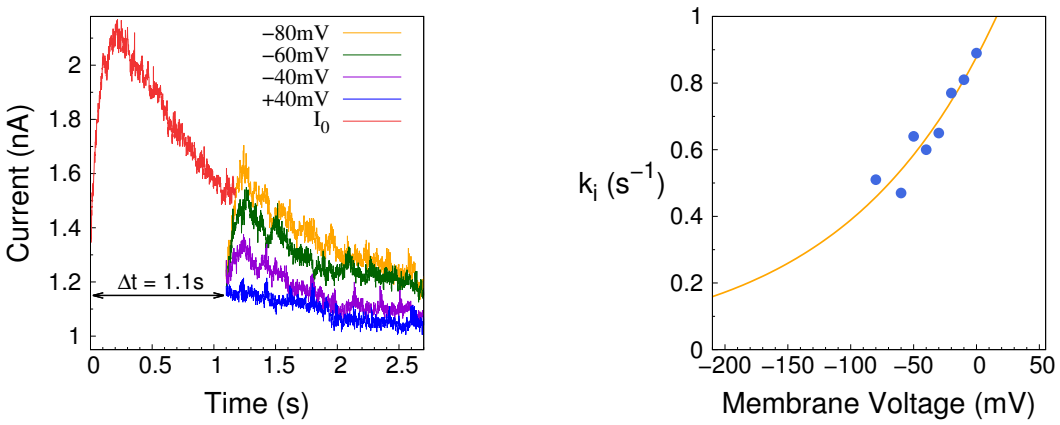

(a) (b)

Figure 3.2: **(a)** Representative time traces of the current corresponding to the voltage clamp protocol used to measure the inactivation rate $k_i(V)$. The initial peak (red trace) gives the maximum current I_0, and the ratio of subsequent peaks in comparison gives the ratio of inactivated channels after a time $t_2 = 1\,\mathrm{s}$ spent at V_2 (legend). **(b)** The inactivation rate $k_i(V)$ plotted vs V, obtained from time traces as in (a). The solid line is a fit with an exponential function $k_i(V) = k_0 \exp(\beta V)$, returning the values $k_0 = 0.878\,\mathrm{s}^{-1}$, $\beta = 8.13\,\mathrm{V}^{-1}$.

Quantitatively, the initial state is prepared with $p_i(t=0) \approx 0$ and $p_o(t=0) \approx 1$. Since we want the effective rate $O \to I$ we consider $d(p_o)/dt = -k_i(V)\, p_o$ for the dynamics while the system is held at $V = V_2$, choosing V_2 such that $k_r(V_2) \approx 0$. Therefore after the time t_2 we have: $p_o(t_2, V) = p_o(0) \exp[-k_i(V)\, t_2]$. For a given voltage, the current is $I \propto p_o$ so $I_{peak}/I_0 = p_o(t_2, V)/p_o(0) = \exp[-k_i(V)\, t_2]$ where I_{peak} is the peak value of the current when the voltage is stepped to V_1 the second time, and I_0 the initial peak of the current, when the voltage is stepped to V_1 the first time (red trace in Fig. 3.2(a)). The quantity $-(1/t_2)\, \ln(I_{peak}/I_0) = k_i(V)$ (where $V = V_2$), obtained from traces as in Fig. 3.2(a), is plotted vs V in Fig. 3.2(b), together with a fit to the form $k_i(V) = k_0 \exp(\beta V)$ (solid line), from which the parameters k_0 and β are determined. From this a value for the inactivation rate is obtained: $k_i = 0.878\, e^{8.13V}$

3.3.1.3 Measuring the Recovery Rate

To measure the recovery rate k_r, the system is prepared in a state where all channels are inactive, $p_i = 1$. The is achieved by holding the AA at an above threshold voltage $V_1 = 100\,\text{mV}$ for an extended period of time ($> 5\,\text{s}$). The voltage is then stepped to a V_2 below the threshold for firing (between -120 to $-80\,\text{mV}$), and held there for a time Δt; during this time, a fraction of the channels recover (into the closed state), with rate $k_r(V_2)$; then the voltage is stepped back up to V_1. A reference measurement is also taken where the system is held at V_2 for a long time ($> 20\,\text{s}$) before stepping the voltage back to V_1. The ratio of measured current over reference current gives the ratio of open channels (i.e. channels which have recovered from inactivation) as a function of V_2 and Δt; $k_r(V)$ can be extracted by repeating the process for several values of V_2 and Δt. Fig. 3.3 shows a sample data set demonstrating the protocol, along with the fit for determining k_r. The resulting rate is: $k_r = 0.034\, e^{-11.4V}$

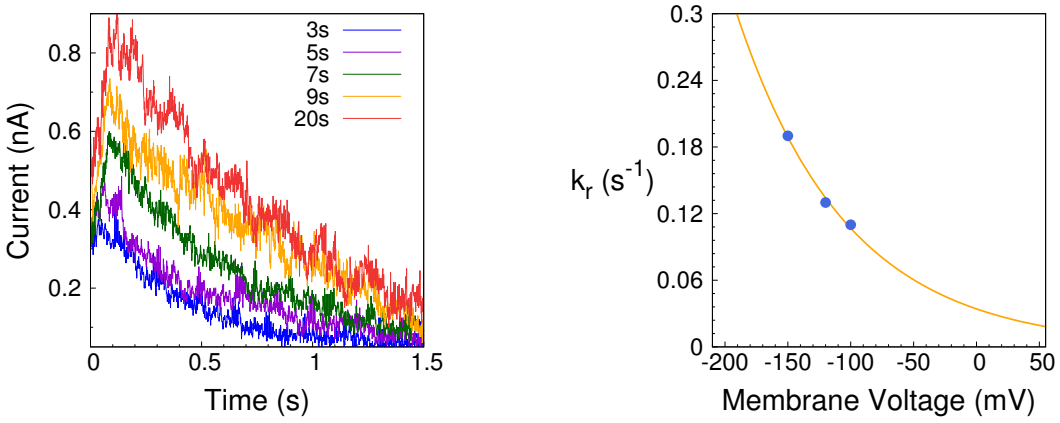

(a) (b)

Figure 3.3: **(a)** Representative time traces of the current corresponding to the voltage clamp protocol used to measure the recovery rate $k_r(V)$. Each curve represents a firing of the AA after recovery for a time t_2 (legend) at $V_2 = -150\,\mathrm{mV}$. The red trace corresponding to $t_2 = 20\,\mathrm{s}$ is taken to be the maximum current, and the ratio of subsequent peaks in comparison gives the ratio of recovered channels after t_2. **(b)** The recovery rate $k_r(V)$ plotted vs V, obtained from time traces as in (a). The solid line is a fit with an exponential function $k_r(V) = k_0 \exp(\beta V)$, returning the values $k_0 = 0.034\,\mathrm{s}^{-1}$, $\beta = -11.4\,\mathrm{V}^{-1}$.

$k_o(V)$	$k_c(V)$	$k_i(V)$	$k_r(V)$
$0.3\,e^{46(V+0.016)}$	$0.3\,e^{-46(V+0.016)}$	$0.878\,e^{8.13V}$	$0.034\,e^{-11.4V}$

Table 3.2: Rates determined from fitting the model on to experimental traces.

3.3.2 Measured Rates of the AA System

To summarize, the measured rates for the model (in units of s^{-1}, V^{-1}) are shown in Table 3.2. The purpose of obtaining these rates is to provide guidance for the experiments in order to realize interesting dynamical behavior and understand the phenomenology. It should be emphasized that measurements are of effective rates for the model, and are not meant as definitive statements on the inherent properties of the KvAP channel. This is because rates are highly sensitive to experimental conditions, and cannot be decisively measured as a fixed quantity without reference to other parameters. For example, the measurements performed in this section were all done using the lipid DPhPC to create the bilayer membrane (Ch. 2), and it has been shown that using a different lipid results in large differences in inactivation times [23] as well as differences in the V_0 of Eq. (3.9) [30]. In addition, fluctuations in other uncontrolled parameters such as leak current, membrane capacitance, and especially temperature [31, 32], may alter the rates from one experiment to another.

Fig. 3.4 shows a comparison between an experimentally obtained data for an the firing of an action potential compared with a numerical simulation of the model Eqs. (3.2), (3.7). Using the rates of Table 3.2 as a starting point, the final simulation has the parameters in Table 3.3. The results demonstrate that the measured rates provide a good reference for numerical simulations of the system, while at the same time giving an idea of where the KvAP rates fall in the parameter space of the model (Ch. 5). This aligns with the goal of determining which of the dynamical phases can be accessed with the present experimental setup. Knowledge of the phase diagram in parameter space will also guide the choice of alternative channels to improve the AA.

$k_o(V)$	$k_c(V)$	$k_i(V)$	$k_r(V)$	N_0	C	χ	V_N	R_c
$3\,e^{53(V+0.016)}$	$3\,e^{-53(V+0.016)}$	$2\,e^{8V}$	$0.01\,e^{-11V}$	80	182 pF	167 pS	42 mV	2 GΩ

Table 3.3: Fitted rates for the red trace in Fig. 3.4.

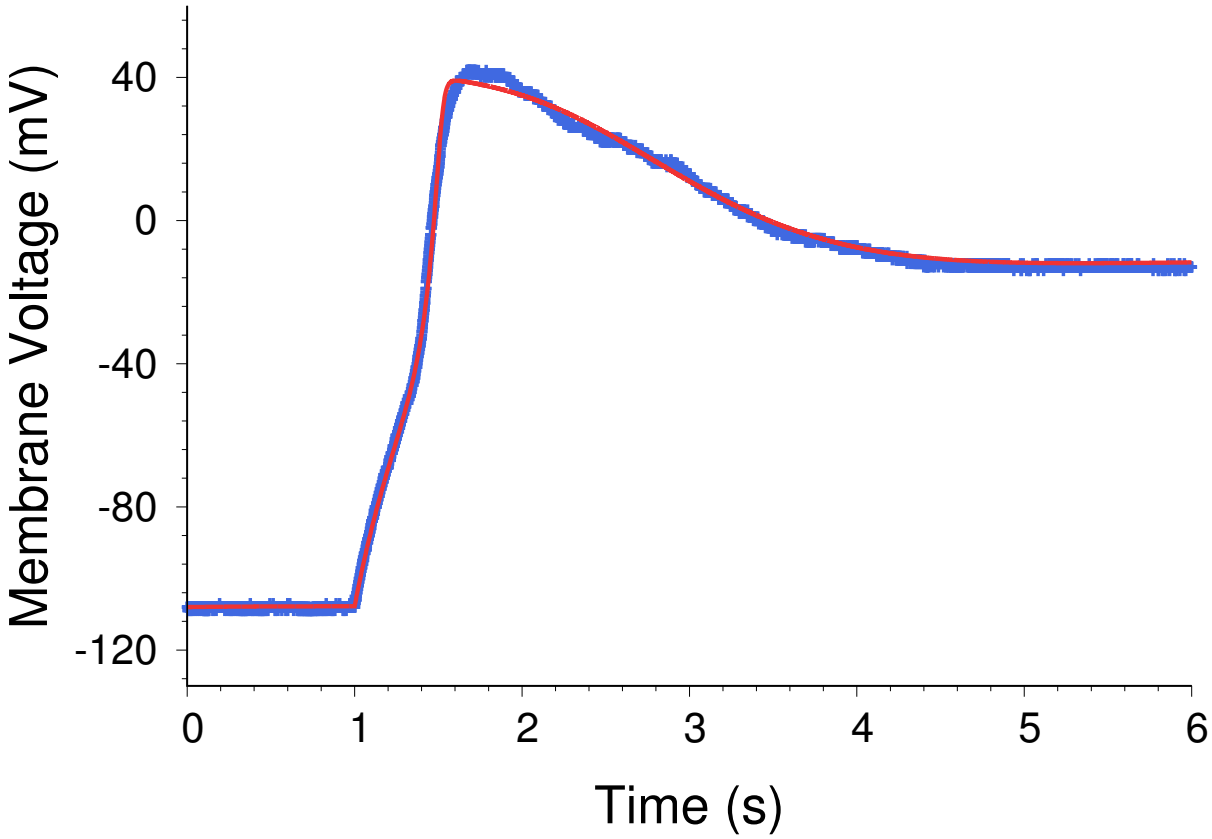

Figure 3.4: Time trace of an action potential firing obtained from the physical AA (blue), fitted with a numerical comparison obtained from integrating the 3D dynamical system using the rates of Fig. 3.2 as a starting point (red).

CHAPTER 4

Critical Behavior Near Threshold

This chapter will detail results on the dynamics of the AA near the threshold for firing. In this region, the AA can be approximated by a 1D dynamical system. The threshold then corresponds to a saddle-node bifurcation, where two critical points collide and annihilate, resulting in a delay in firing APs due to critical slowing down near the remnant of the bifurcation. This effect is measured, and a scaling exponent extracted.

4.1 Normal Form of the Saddle-Node Bifurcation

The occurrence of a saddle-node bifurcation in the firing of the Artificial Axon can be shown by comparing the behavior of the system near threshold to the normal form of the saddle-node bifurcation. In one dimension, the normal form is:

$$\dot{x} = r + x^2 \tag{4.1}$$

where r is a control parameter. For $r < 0$ the system has two fixed points ($\dot{x} = 0$), one stable and one unstable. They merge at the critical point $r = 0$; for $r > 0$ the velocity is always positive so the system escapes to infinity. The transition exhibited by the dynamical system Eq. (4.1) as the parameter r goes through the critical value $r = 0$ is termed a saddle node bifurcation [33]. The system exhibits critical slowing down near the critical point: for $r > 0$, Eq. (4.1) integrates to:

$$x(t) = \sqrt{r}\,\tan(\sqrt{r}\,t + b) \qquad b = \arctan(x(0)/\sqrt{r}) \tag{4.2}$$

From the form Eq. (4.2), it can be seen that the time to escape to infinity is finite. Starting from a large negative value $x(0)$, so that $b \approx -\pi/2$, that time is:

$$\tau \sim \frac{\pi}{\sqrt{r}} \propto r^{-1/2} \tag{4.3}$$

which can also be estimated by:

$$\tau \sim \int_{-\infty}^{+\infty} \frac{dx}{r + x^2} = \frac{\pi}{\sqrt{r}} = \pi\,(r - r_c)^{-1/2} \tag{4.4}$$

The time to escape diverges as one approaches the critical point from above, and scales with the distance to the critical point with characteristic exponent $-1/2$. The relations Eqs. (4.3), (4.4) are exact if τ is the time for $x(t)$ in Eq. (4.1) to move from $x = -\infty$ at $t = 0$ to $x = +\infty$ at $t = \tau$. They also approximate the time for the system to move between two finite values of x across the transition. The reason is that for r close to the critical value, the dominant contribution to τ comes from the neighborhood near $x = 0$, where there previous was a fixed point; thus the escape time is roughly independent of the starting and end points.

4.2 Saddle-Node Bifurcation in the Artificial Axon

The existence of the bifurcation in the AA system can be shown explicitly if the following two approximations are made: $p_o(t)$ is taken to be the equilibrium value $p_e(t)$ in Eq. (3.2), and the inactive state p_i is neglected. The first approximation is valid if the opening and closing rates are much faster than the other time scales in the system, which is the case for the KvAP. The second approximation is also reasonable near the threshold for firing; to generate an action potential, the system must start at a large negative resting voltage and approach the threshold from below, with channels starting in the closed state. Under the

model of Fig. 3.1, channels cannot inactivate until they open; meaning that the in the region of interest near the threshold for firing (where channels have just begun to open), inactivation is negligible. Given these two approximations, the 3D dynamical system Eqs. (3.2), (3.7), reduces to 1D:

$$\frac{dV}{dt} = -\frac{N_0\chi}{C}\left[p_e(V) + \chi_\ell/\chi\right][V(t) - V_N] - \frac{1}{RC}\left[V(t) - V_{clamp}\right] \tag{4.5}$$

where $p_e(V)$, the steady state open probability, is a Fermi-Dirac function as discussed in Ch. 3:

$$p_e(V) = \frac{1}{1 + e^{-\frac{2q}{kT}(V - V_0)}} \tag{4.6}$$

with experimentally determined values $V_0 = -16.1$ mV, $\gamma = kT/q = 21.7$ mV [18]. The fixed points ($dV/dt = 0$) of the dynamical system Eqs. (4.5), (4.6) are given by:

$$p_e(V) = \frac{1}{N_0\chi R}\left(\frac{V - V_{clamp}}{V_N - V}\right) - \frac{\chi_\ell}{\chi} \tag{4.7}$$

Fig. 4.1 shows plots of Eq. (4.7) as a function of V for three different values of V_{clamp}, the relevant range of voltages being $V_{rest} < V(t) < V_N$ ($V_{rest} \approx -200\,\text{mV}$). The fixed points of the system are given by the intersection of the two curves.

For V_{clamp} sufficiently negative, shown in Fig. 4.1(a), there are 3 fixed points. As V_{clamp} is increased, the stable and unstable fixed points on the left merge at a critical point as shown in Fig. 4.1(b), i.e. the threshold, where the two curves in the figure are tangent to each other. For values of V_{clamp} greater than the critical point, there is only one stable fixed point near the Nernst potential, as in Fig. 4.1(c). This is the same bifurcation as exhibited by the dynamical system Eq. (4.1), thus the same behavior should occur near the critical point. If V_{clamp} is stepped close to, but above, V_{crit}, there will be a delay time for firing, scaling as:

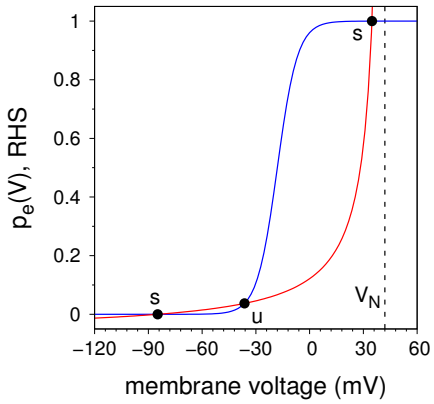

(a)

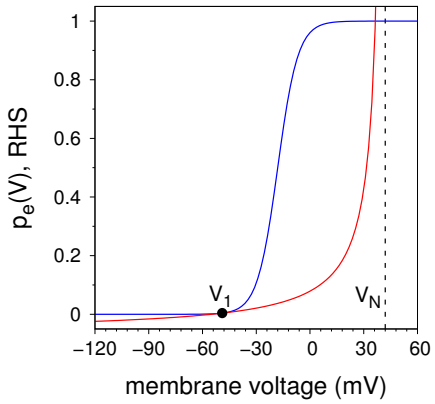

(b)

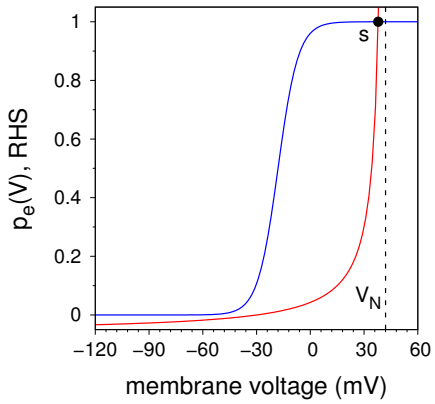

(c)

Figure 4.1: Plots of the LHS (blue) and the RHS (red) of equation (4.7), for three different V_{clamp} values; the dotted asymptote indicates the Nernst potential V_N.

(a) $V_{rest} < V_{clamp} < V_{crit}$, two stable (s) fixed points and one unstable (u).

(b) $V_{clamp} = V_{crit}$, at the critical point $V = V_1$.

(c) $V_{clamp} > V_{crit}$, the only remaining fixed point is near V_N (action potential deplorizes).

$$\tau \sim (V_{clamp} - V_{crit})^{-1/2} \tag{4.8}$$

To show this, first note that the critical point, $V_{clamp} = V_{crit}$, $V(t) \equiv V_1$, is defined by:

$$\begin{cases} p_e(V_1) = \dfrac{1}{N_0 \chi R}\left(\dfrac{V_1 - V_{crit}}{V_N - V_1}\right) - \dfrac{\chi_\ell}{\chi} \\ \\ \left.\dfrac{dp_e}{dV}\right|_{V=V_1} = \dfrac{\partial}{\partial V}\left(\dfrac{1}{N_0 \chi R}\ \dfrac{V - V_{crit}}{V_N - V}\right)\Bigg|_{V_1} \\ \\ = \dfrac{1}{N_0 \chi R}\dfrac{V_N - V_{crit}}{(V_N - V_1)^2} \end{cases} \tag{4.9}$$

Set $V_{clamp} = V_{crit} + \epsilon$ and write (4.5) in the form:

$$\frac{dV}{dt} = F(V, V_{clamp}) \tag{4.10}$$

Expanding around the critical point:

$$F(V, V_{crit} + \epsilon) \approx F(V, V_{crit}) + \frac{1}{RC}\,\epsilon \tag{4.11}$$

while

$$\begin{aligned} F(V, V_{crit}) \approx F(V_1, V_{crit}) + \frac{\partial}{\partial V} F(V, V_{crit})|_{V_1}\,(V - V_1) \\ + \frac{1}{2}\left(\frac{\partial^2 F}{\partial V^2}\right)\Bigg|_{V_1}(V - V_1)^2 \end{aligned} \tag{4.12}$$

Using Eq. (4.7), the first two terms on the RHS of Eq. (4.12) vanish. Also, the coefficient of the quadratic term is positive. Finally,

$$F(V, V_{crit} + \epsilon) \approx \frac{1}{RC}\,\epsilon + b\,(V - V_1)^2$$
$$b = \frac{1}{2}\left.\frac{\partial^2 F}{\partial V^2}\right|_{V_1} > 0, \quad \epsilon = V_{clamp} - V_{crit} > 0 \tag{4.13}$$

Thus, close to the critical point the dynamical system Eq. (4.5) reduces to the form of Eq. (4.1). Using the estimate Eq. (4.4) for the delay time:

$$\begin{aligned}\tau \sim \int_{-\infty}^{+\infty} \frac{dV}{\epsilon/RC + b(V - V_1)^2} &= \frac{\pi}{\sqrt{b\epsilon/(RC)}} \\ &= \pi\sqrt{\frac{RC}{b}}\,(V_{clamp} - V_{crit})^{-1/2}\end{aligned} \tag{4.14}$$

and, noting that $b \propto N_0\chi/C$:

$$\tau \propto \frac{RC}{\sqrt{N_0 R\chi}}\,(V_{clamp} - V_{crit})^{-1/2} \tag{4.15}$$

The delay time scales with the distance to the critical point with the exponent $-1/2$, as expected, with a prefactor proportional to the characteristic RC time scale, modulated by a factor which depends on the number of channels and the ratio between the open channel conductance and the CLVC conductance.

The rate at which the voltage proceeds to the fixed point close to the Nernst potential can be visualized via trajectories in phase space. Fig. 4.2(a) shows a plot of dV/dt vs V for several trajectories (time traces) obtained from directly integrating the full (3D) AA model. Note that a point in the plane of Fig. 4.2(a) does not completely represent the state of the system, as inactivation is unaccounted for. However, this plot is still useful for a qualitative description of the delay in firing. When V_{clamp} is stepped up, dV/dt jumps to a positive value

and the voltage immediately starts to rise. For $V_{clamp} > V_{crit}$, dV/dt reaches a minimum in the vicinity of the critical point V_1, i.e. the dynamics of the system slows down in this vicinity. This is shown in Fig. 4.2(b), where $1/(dV/dt)$ for the blue trajectory is plotted. This quantity is proportional to the time the system spends near the voltage V. The peak in this plot identifies a "bottleneck region" which is ultimately responsible for the scaling behavior of the delay time τ. Eventually, dV/dt will start to rise again due to the opening of the channels and spiking will occur, as shown in the right half of Fig. 4.2. The subsequent drop and sign change in velocity is due to the inactivation of the channels which moves the fixed point back near V_{crit}.

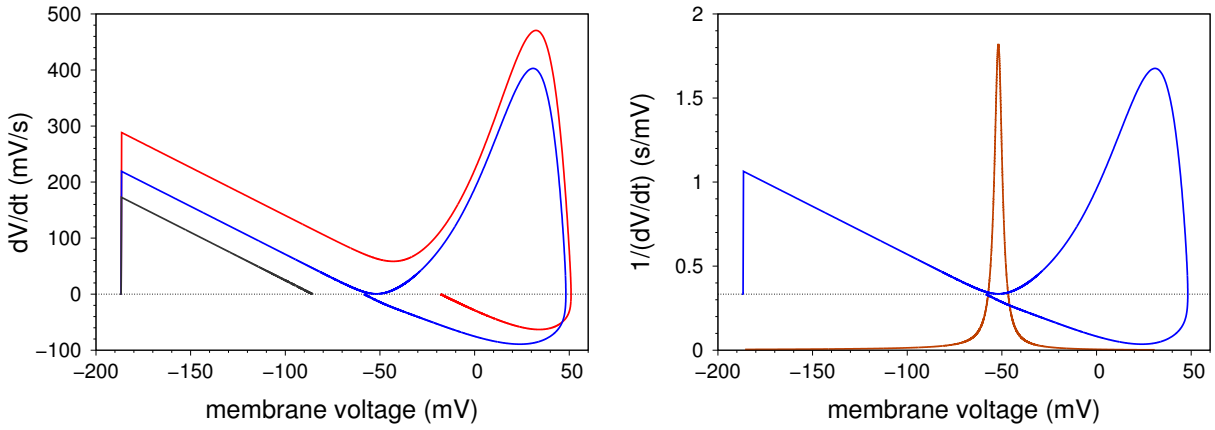

(a) (b)

Figure 4.2: **(a)** Trajectories in phase space from integrating the 3D model. Starting from $V_{clamp} = -200\,\text{mV}$, the clamp was stepped up to $-86\,\text{mV}$ (black), $-58.8\,\text{mV}$ (blue), and $-18.18\,\text{mV}$ (red) and held steady. The black trajectory is below threshold and fails to depolarize. The blue trajectory, reaching closer to the saddle-node remnant, experiences a significant delay before firing compared to the red. **(b)** The same blue trajectories from (a) juxtaposed with the corresponding plot of $1/(dV/dt)$ (brown trace, y-axis). The area under the brown curve represents the total time elapsed, with most of the contribution coming from the vicinity of the saddle-node remnant.

4.3 Experimental Measurements

The delay in firing near threshold can also observed experimentally in the physical Artificial Axon system. Starting with an AA prepared in the usual way (Ch. 2), the system is held steady at a voltage by the clamp at $V_{clamp} = -200\,\mathrm{mV}$. At this voltage almost all the channels are in the closed state, $p_c \approx 1$, $p_o \approx p_i \approx 0$. V_{clamp} is then stepped up to various values between 0 and $-100\,\mathrm{mV}$ and held steady. If functional ion channels are in the membrane and V_{clamp} is above the threshold V_{crit}, the AA will fire. Whereas if V_{clamp} is below V_{crit}, the AA does not fire and voltage will stabilize at $V(t) \approx V_{clamp}$. After the AA has fired, V_{clamp} is stepped back to $-200\,\mathrm{mV}$ and held there for 20 s to allow the channels to recover from inactivation; this process is then repeated, varying the value that V_{clamp} is stepped to.

Fig. 4.3 shows the resulting time traces of the experimental protocol, for various values of V_{clamp}. As predicted by the analysis in Section 4.2, there is a delay time, τ, it takes to depolarize the inner chamber when membrane voltage is stepped close to the voltage threshold V_{crit} from below. The measure of delay τ adopted here is defined as the time interval between the step in V_{clamp} and the peak of the action potential. Note that for electrophysiologists, various other definitions of the firing time exist. With regards to our goal of using τ to find the threshold voltage and extracting the scaling exponent, the choice of τ does not significantly alter the results.

Of course, the dynamics of the real system reduces to Eq. (4.1) only near the critical point, and consequently the exact solution Eq. (4.2) applies to the physical AA only close to the critical point. This is shown in Fig. 4.4, where the different time traces from Fig. 4.3 are rescaled according to Eq. (4.2), and are seen to collapse into a "universal" form near the critical point $V = V_1$.

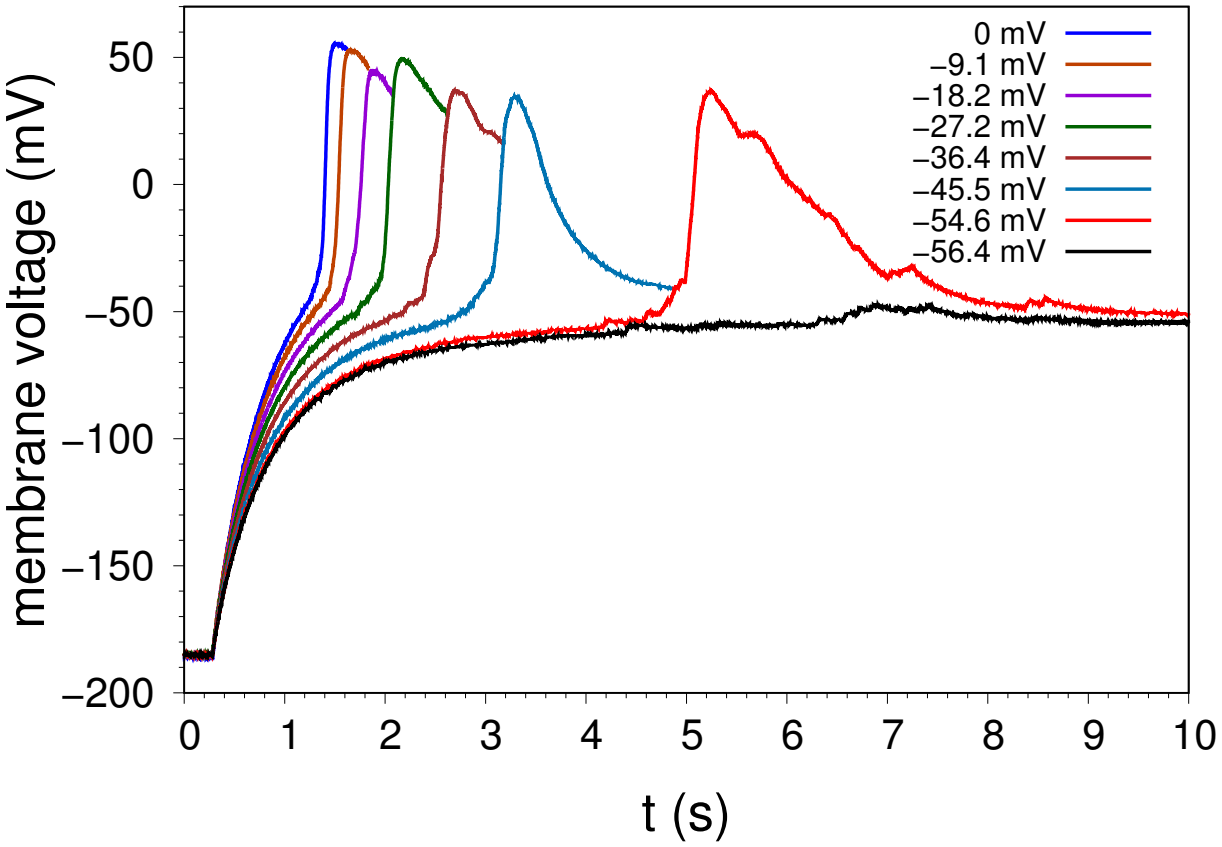

Figure 4.3: Series of action potentials evoked by stepping the CLVC to the values shown in the key, plotted on a common time axis. Firing is delayed as V_{clamp} is decreased towards V_{crit}, until V_{clamp} is below threshold and no action potential is fired (black trace).

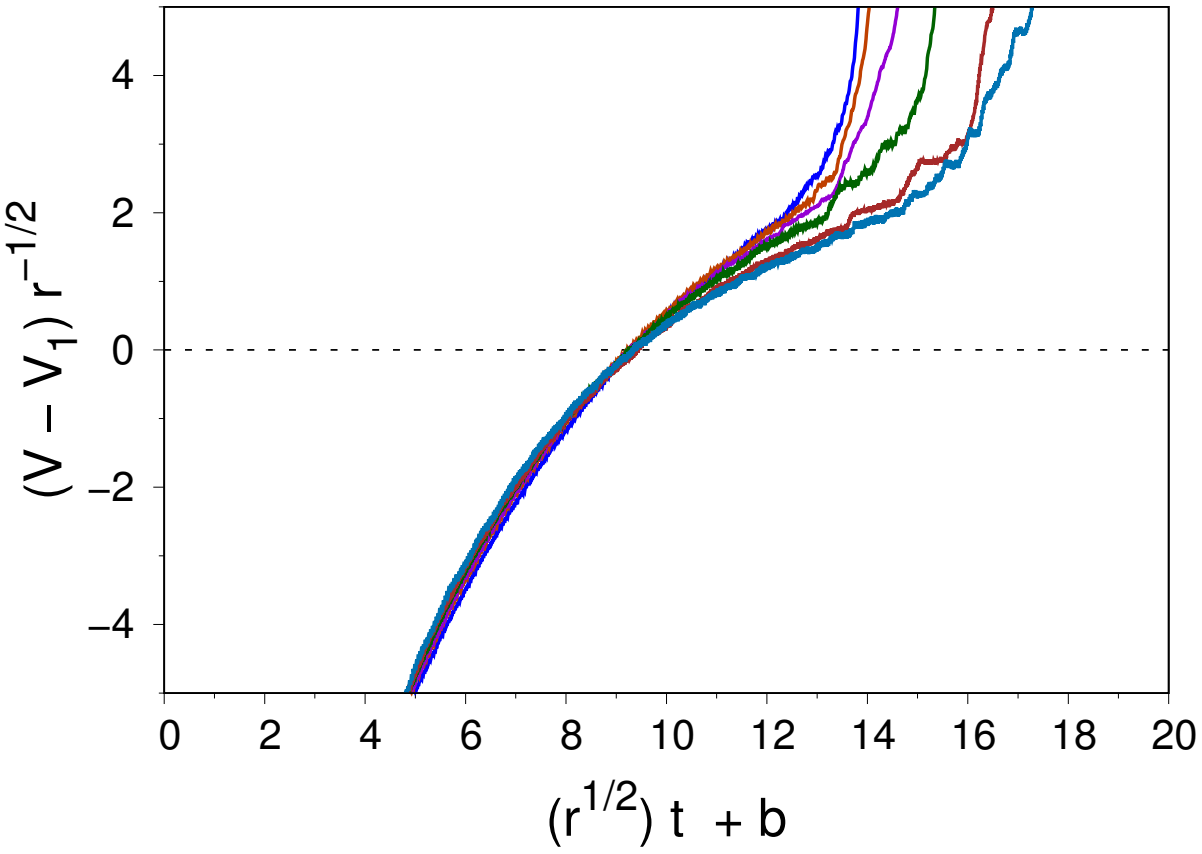

Figure 4.4: Experimental data Fig. 4.3 plotted in the form of Eq. (4.2). Near the critical point ($V = V_1$, dashed line) the traces collapse as the dynamics in this region are universal. The particular parameters used in Eq. (4.2) are: $b = -\pi/2$, $V_1 = -66$ mV, and $r = (V_{clamp} - V_{crit})/RC$.

4.3.1 Determining the Threshold

Based on the derivations in Section 4.2, the delay time τ should be a function of $(V_{clamp} - V_{crit})$, scaling with a theoretical exponent of $-1/2$. In order to fit the experimental data with this relation and verify whether the same scaling holds, it is essential to have a precise determination of the threshold V_{crit}, i.e. the location of the critical point in phase space. A direct measurement V_{crit} involves repeated experiments involving the variation of V_{clamp} until a value is found such that any clamp value below it does not elicit firing. In practice, direct measurement of the threshold is not very realistic, as the required resolution cannot be realistically attained when considering noise and stability of the experiment.

Instead, given that V_{crit} is a parameter value at the critical point of the system, fitting techniques can be employed to extrapolate it from time trace data. For a given data set of AA firings as a function of V_{clamp} (e.g. Fig. 4.3), plots of $\log \tau$ vs $\log (V_{clamp} - V_{crit})$ are produced for various values of V_{crit} near the empirically observed value. Each plot is fitted to a second order polynomial in $\log (V_{clamp} - V_{crit})$. A quadratic coefficient is obtained from each of these plots, which is then plotted against the corresponding V_{crit} value. Performing linear regression on the plot of quadratic coefficients vs V_{crit}, the value of V_{crit} which corresponds to a quadratic coefficient of zero is taken to be the threshold (Fig. 4.5). To put it in simpler terms: for a given data set, different values of V_{crit} are trialed, and the one which returns a straight line in the plot of $\log \tau$ vs $\log (V_{clamp} - V_{crit})$ is chosen to be the actual value, as that is the expected behavior of the system.

It's important to emphasize that V_{crit} is different from the critical membrane voltage at which the axon fires, defined as the membrane voltage corresponding to the location of the critical point ($V(t) = V_1$, see Section 4.2). The methods that have been employed in electrophysiology for estimating action potential thresholds actually estimate this latter quantity,

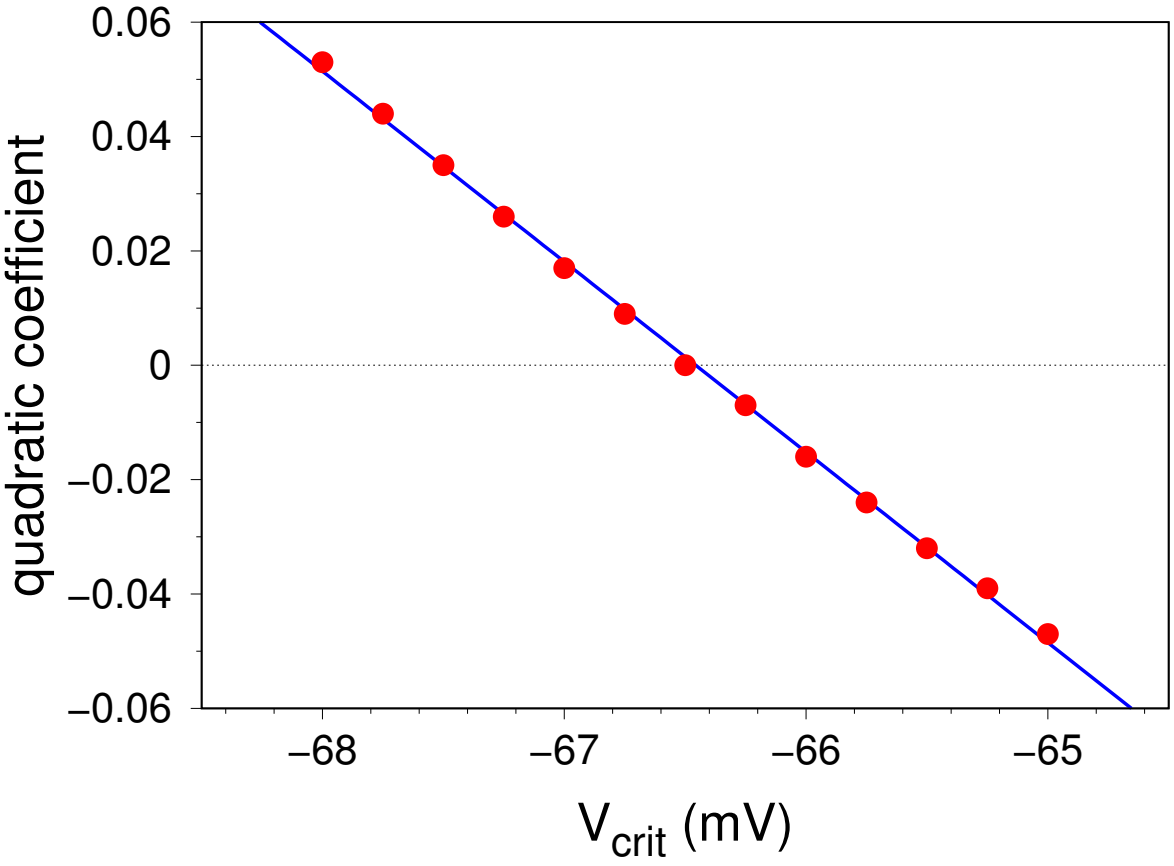

Figure 4.5: The quadratic coefficients of plots of $\log \tau$ vs $\log(V_{clamp} - V_{crit})$, for different values of V_{crit}. The x-intercept of the least squares fit (blue line) is taken as the threshold value V_{crit} for the purpose of obtaining scaling exponents. In this case, $V_{crit} \approx -66.5\,\mathrm{mV}$

the well known methods all relate to observing changes in the derivative of the voltage [34]. In our setup, we could also keep the CLVC fixed, and introduce a traditional current clamp injecting a current I_{cc} into the AA. We would then have a corresponding threshold I_{crit}, which is the more usual situation in electrophysiology (the scaling would remain the same).

4.3.2 Scaling Near the Threshold

The determination of the critical exponent under the scaling assumption for one data set is shown in Fig. 4.6. Fig. 4.6(a) is a log-log plot of the delay time τ vs $(V_{clamp} - V_{crit})$, using the threshold value $V_{crit} = -90.6$ mV, determined using the method of the previous section. The slope of the linear fit gives a critical exponent $\beta = -0.57 \pm 0.04$, close to the theoretical value of -1/2. Fig. 4.6(b) is a linear plot of the same data with the delay time plotted directly against V_{clamp}, i.e. without predetermining V_{crit}. The solid line is a three parameter fit to the power law:

$$\tau \; = \; \alpha \, (V_{clamp} - V_{crit})^{\beta} \tag{4.16}$$

This fit returns the values: $\alpha = 9.49$, $V_{crit} = -87.5 \pm 6.1$ mV, and $\beta = -0.51 \pm 0.11$. The values for V_{crit} and the scaling exponent β differ slightly compared to the values obtained from Fig. 4.6(a), but are compatible within error.

Though experimental data in Fig. 4.6 shows good agreement with the prediction that the scaling exponent should be -1/2, it is lacking in the sense that the range of the measurements is quite limited, covering only a decade in the control parameter $(V_{clamp} - V_{crit})$. This is a result of several factors, most notably the relatively small number of channels in the AA, which limits how close one is able to get to the critical point, and beyond that, the stability and noise in the system.

Fig. 4.7(a) shows plots for two more independent data sets; the values of V_{crit} were determined in the same way as for the plot in Fig. 4.6. These data sets show differing values of the scaling exponent, which is likely due to the drifting of the threshold during the experiment. To be specific, this is because in the experimental system, parameters such as N_0 and C can change over the course of the experiment. For example, a painted membrane may shrink as

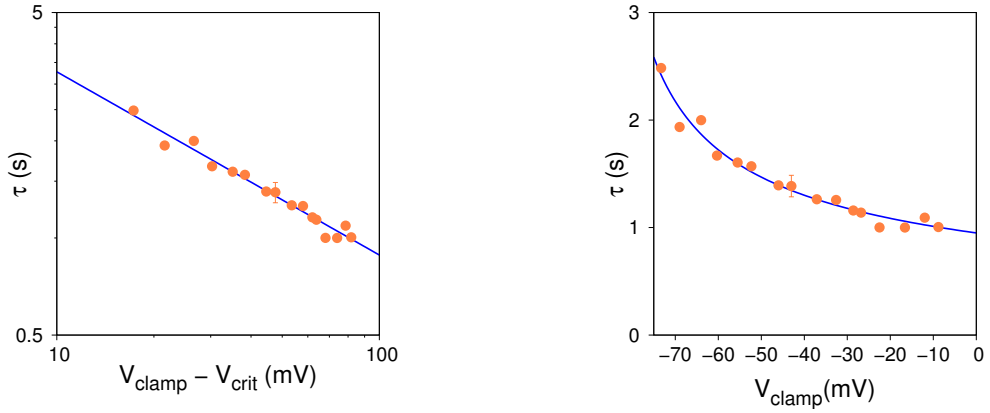

(a) (b)

Figure 4.6: **(a)** Data from one set of recordings in the physical AA, uncertainty on individual measurements is given by a representative error bar on one data point. (a) Log-log plot of τ $(V_{clamp} - V_{crit})$, with $V_{crit} = -90.6 \pm 1.1$ mV. The resulting scaling exponent from the linear fit is $\beta = -0.57 \pm 0.04$. **(b)** The same data plotted on a linear scale with V_{crit} as a free parameter. The exponent obtained this way is $\beta = -0.51 \pm 0.11$.

the decane surrounding it collapses inward, changing the size of the membrane and thus its capacitance; or channels which were pipetted in may not have inserted into the membrane immediately, floating above the membrane and stochastically inserting over time, altering the number of channels N_0. As a result of these fluctuations, the threshold may shift over the course of an experiment.

The following observation supports the idea that threshold drift may be the cause of the mismatched exponents: The time traces corresponding to the purple dots in Fig. 4.7(a) are of the same data set as shown in Fig. 4.3. From Fig. 4.3, it can be seen that $V_{clamp} = -56.4\,\text{mV}$ is just below threshold, while $V_{clamp} = -54.6\,\text{mV}$ is just above. This constrains the threshold to be in the range $V_{crit} = -55.5 \pm 1\,\text{mV}$. Fig. 4.7(b) shows the log-log plot with the "experimentally constrained" value of V_{crit}, eliminating the longest delay data point which is clearly off (the longest delay points being most affected by a drift in V_{crit}). There is a slight

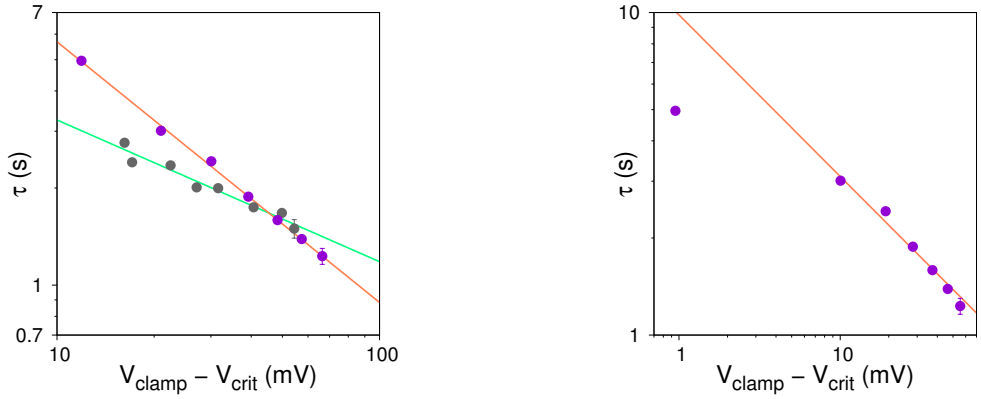

(a) (b)

Figure 4.7: **(a)** Two additional data sets (purple and green dots) obtained from two independent experiments, plotted the same way as Fig. 4.6(a). For the purple dots (same data set as Fig. 4.3), $V_{crit} = -66.5 \pm 0.6\,\text{mV}$, and the slope of linear fit (orange) is $\beta = -0.81 \pm 0.03$. For the green dots, $V_{crit} = -54.4 \pm 1.0\,\text{mV}$, and $\beta = -0.44 \pm 0.04$. **(b)** The same data as the purple dots in (a), plotted using the "experimentally constrained" value $V_{crit} = -55.5\,\text{mV}$. The linear fit excludes the point closest to threshold (see text); $\beta = -0.50 \pm 0.04$.

N_0	C	χ	χ_ℓ/χ	R_c	$V(t=0)$	$p_c(t=0)$
110	329.7 pF	170 pS	8.8×10^{-4}	2 GΩ	-200 mV	1

Table 4.1: Parameters used in integrating the 3D dynamical system directly.

curvature, but fitting to a straight line returns an exponent close to $-1/2$ ($\beta = -0.50 \pm 0.04$).

While these results clearly demonstrate that the scaling behavior described is present in the AA, the experimental conditions prevent precise measurements of the exponent. To explore regions closer to the threshold and verify whether the scaling holds, numerical methods are adopted to supplement the experimental results.

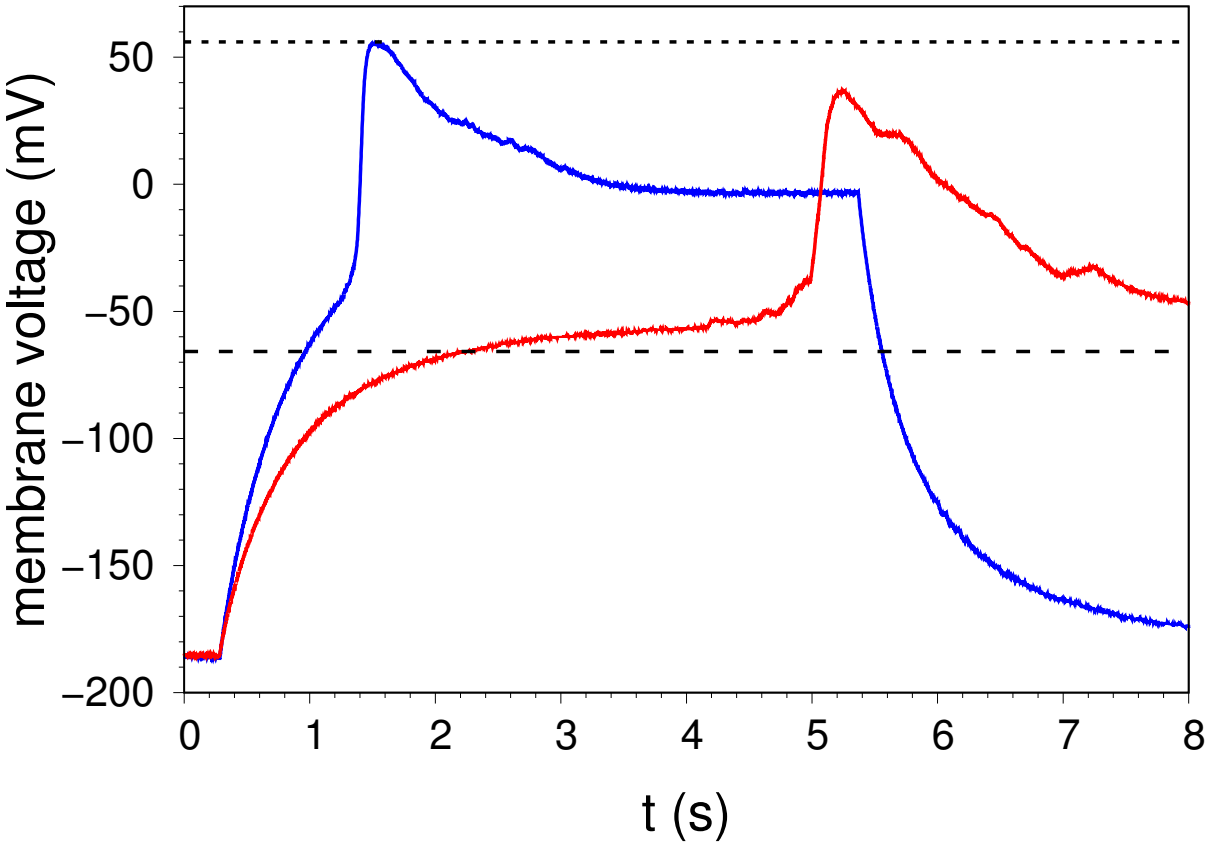

Figure 4.8: Two action potentials recorded in the physical AA, demonstrating delay in firing for clamp values near threshold. For both traces, the CLVC was held at $V_c = -200\,\text{mV}$ before being stepped up at $t = 0.28\,\text{s}$ to $V_c = 0\,\text{mV}$ (blue) and $V_c = -54.55\,\text{mV}$ (red). The dashed line shows the threshold $V_{crit} \approx -66.5\,\text{mV}$, while dotted line is the Nernst potential. The break in the blue trace at $t \approx 5.5\,\text{s}$ corresponds to the CLVC being stepped down again to $V_{clamp} = -200\,\text{mV}$.

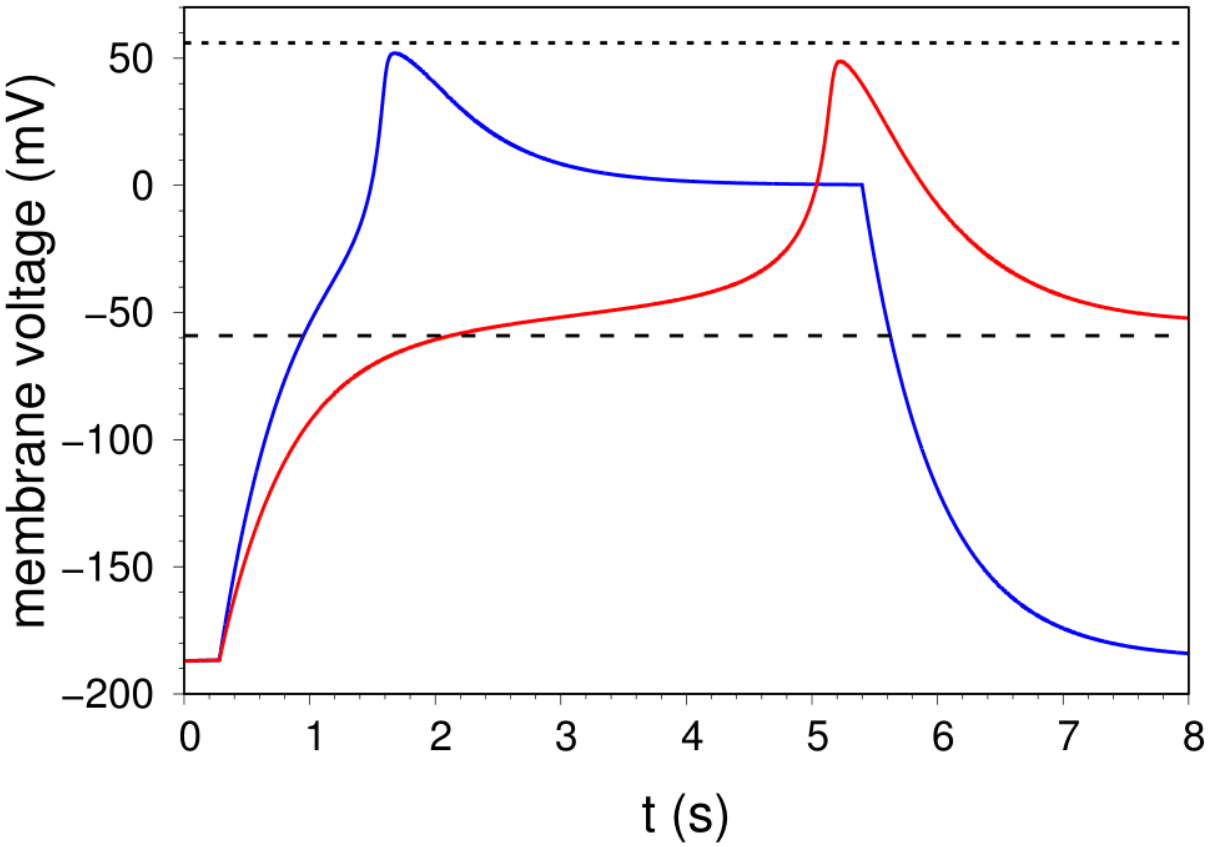

Figure 4.9: Action potentials produced from integrating the 3D model. The clamp protocol and other settings follow those in Fig. 4.8. Namely, $V_{clamp}(t = 0) = -200\,\mathrm{mV}$, at $t = 0.28\,\mathrm{s}$ the clamp is raised to $0\,\mathrm{mV}$ for the blue trace and $-54.55\,\mathrm{mV}$ for the red, displaying the same delay in firing effect. The dashed line shows the threshold $V_{crit} \approx -59.1\,\mathrm{mV}$, the dotted line shows the Nernst potential.

4.4 Numerical Results

By integrating 3D dynamical system Eqs. (3.2), (3.7) directly, the delay in firing near the threshold can be reproduced numerically. Figs. 4.8 and 4.9, show a comparison between an experimental firing of the AA and numerically simulated firing from integrating the model. With proper fitting of the system parameters (Table 4.1), the numerical results match very closely with that of the physical system. Simulated AAs can access a large range in the distance to threshold, and in turn provide a good determination of the scaling exponent. This is because, unlike the experiment, there are no concerns of noise or stability, and with the parameters truly fixed there is also no drifting of the threshold. With that in mind, the "experiment" is carried out numerically, repeating the same methods as the previous section, i.e. producing a series of action potentials for different values of V_{clamp}, measuring the delay time τ, determining the threshold V_{crit}, and producing a log-log plot of τ vs $(V_{clamp} - V_{crit})$ to determine a scaling exponent. Fig. 4.10 shows one such data set, the resulting linear fit has a slope of $\beta = -0.51$, very close to the theoretical value. The numerical result also shows good agreement with the experimental data in the range where they overlap, further affirming how well the numerical approach models the physical system.

The data of Fig. 4.10 shows that the scaling relation holds for a relatively large range in the parameter $(V_{clamp} - V_{crit})$. This naturally leads to the question of whether this behavior holds for values of V_{clamp} arbitrarily close to the threshold, as is the case with the normal form of the saddle node bifurcation. Further simulations show that this is not the case; there is deviation from the expected scaling extremely close to the threshold, shown in Fig. 4.11. For a distance to threshold of less than $\approx 0.2\,\mathrm{mV}$, the relationship between τ and $(V_{clamp}–V_{crit})$ is no longer a straight line in the log-log plot. This is not entirely unexpected; the reason being that the effect of inactivation becomes non-negligible at long delay times. Though the inactivation rate is much smaller than the opening rate at threshold voltage, given a long enough delay time, some fraction of the channels will inevitably inactivate before firing. This

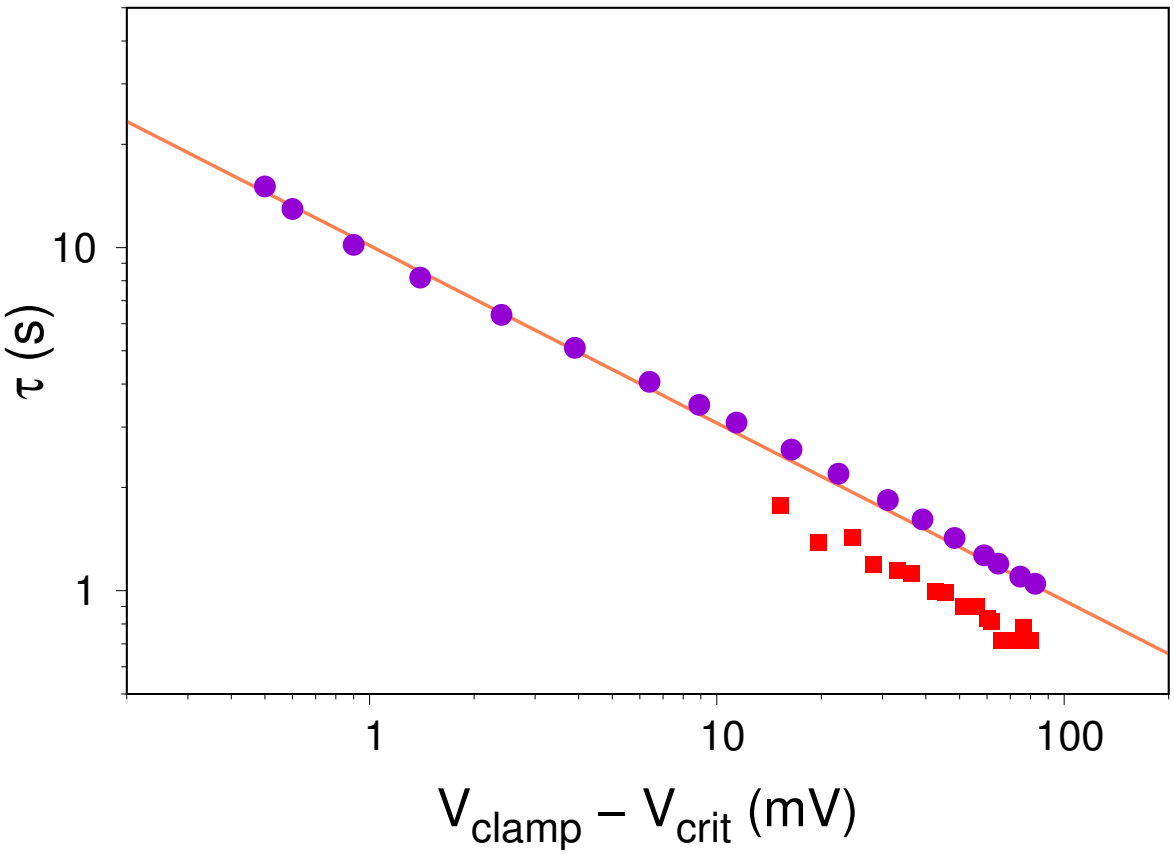

Figure 4.10: Log-log plot of the delay time τ vs distance to the critical point ($V_{clamp} - V_{crit}$) on the simulated AA (purple), using the same procedure as the experimental data of Fig. 4.6. The threshold is determined to be $V_{crit} = -91.4\,\text{mV}$, compared to $-90.6\,\text{mV}$ for the experimental data in Fig. 4.6(a). The linear fit returns a scaling exponent of $\beta = -0.51$. The experimental data of Fig. 4.6 are overlaid (red) for comparison, shifted downward for visual clarity.

effectively reduces the number of channels in the system, which, as shown in Fig. 4.12, will result in a shifting of V_{crit}. Thus, even in the simulated system, which is idealized compared to the physical one, deviation from -1/2 scaling is still unavoidable when very close to the threshold, as the assumption of a 1D dynamical system is no longer valid when inactivation has a sizable effect.

Solutions to Eq. (4.7) with steady state opening were also calculated numerically to obtain a relation between N_0 and V_{crit} for varying values of χ_ℓ. The results show that for a given ion channel and clamp (fixed R and χ), there exists a range of N_0 such that excitability is possible, above and below which there is no bifurcation and thus no possibility of action potentials occurring. This fact can also be seen directly from the graphical representation of Eq. (4.7) in Fig. 4.1: increasing N_0 makes the slope of the RHS of Eq. (4.7) shallower, and thus V_{crit} more negative, but since $\chi_\ell/\chi > 0$ there is a maximum N_0 beyond which the only fixed point is the one close to V_N (i.e. a steady state with channels open). Conversely, decreasing N_0 makes the slope of the RHS of Eq. (4.7) steeper, and thus V_{crit} increases; the critical point V_1 (Eq. (4.9)) moves towards the inflection point of the open probability curve $p_e(V)$, and if N_0 is too small, the unstable fixed point disappears, and so there is no firing.

In the case that there is no leak ($\chi_\ell = 0$), there is a logarithmic relationship between the number of channels and the threshold. This is in agreement with previous numerical studies [1] that calculate a relationship between conductivity and threshold voltage, since the total conductance is directly proportional to the number of channels. As χ_ℓ increases, V_{crit} becomes more negative, and the relationship is no longer logarithmic. When the leak is taken to be the same value as in the simulation, the numerical solutions with steady state opening are in good agreement with the simulation of 3D model, indicating that the threshold does not depend strongly on the opening model. These results are displayed in Figs. 4.12 and 4.13.

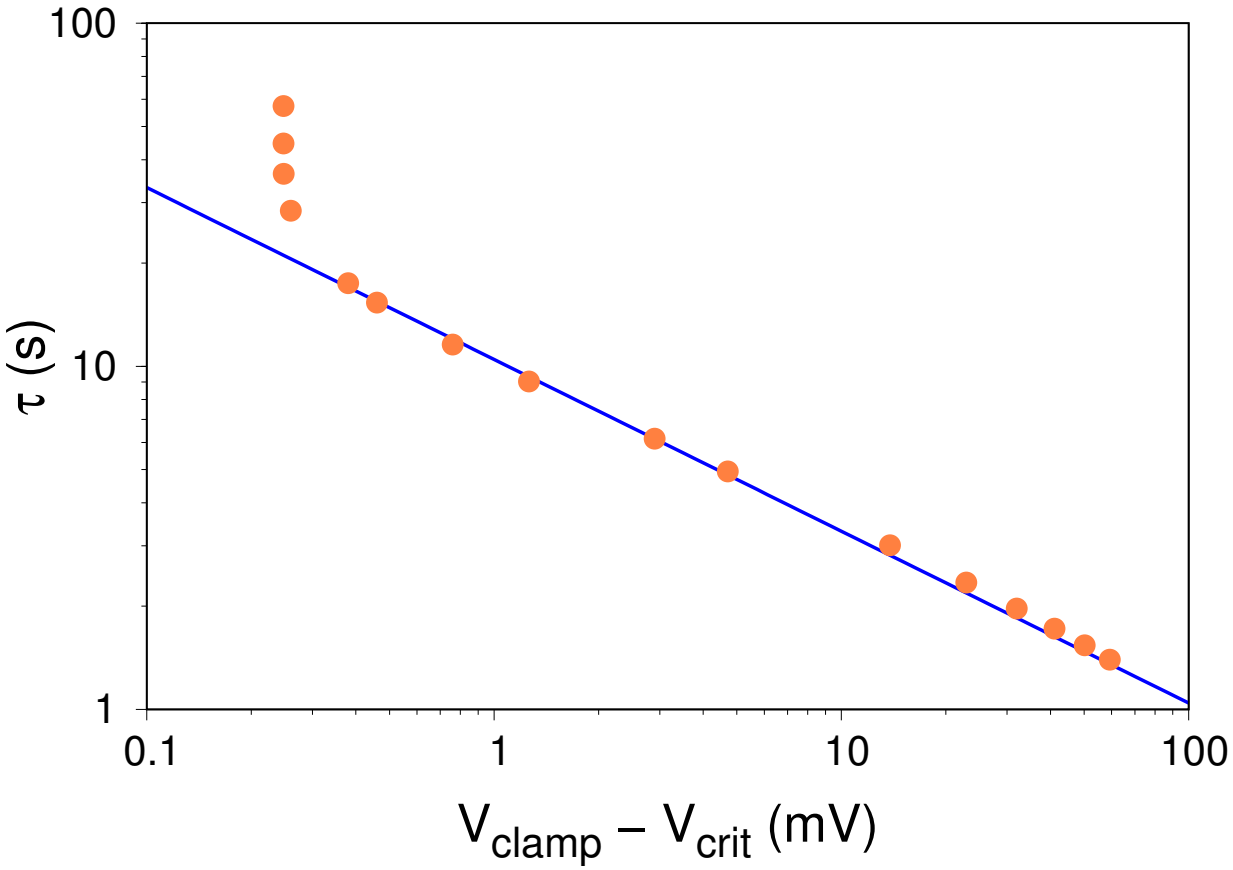

Figure 4.11: Log-log plot of delay time vs distance to critical point obtained from the numerical integration, the same plot as Fig. 4.10 for a different data set. Points extremely close to the critical point showcase deviation from expected scaling, due to channel inactivation. The linear fit excluding the leftmost four data points returns a scaling exponent of -0.50, with $V_{crit} = -59.26\,\mathrm{mV}$

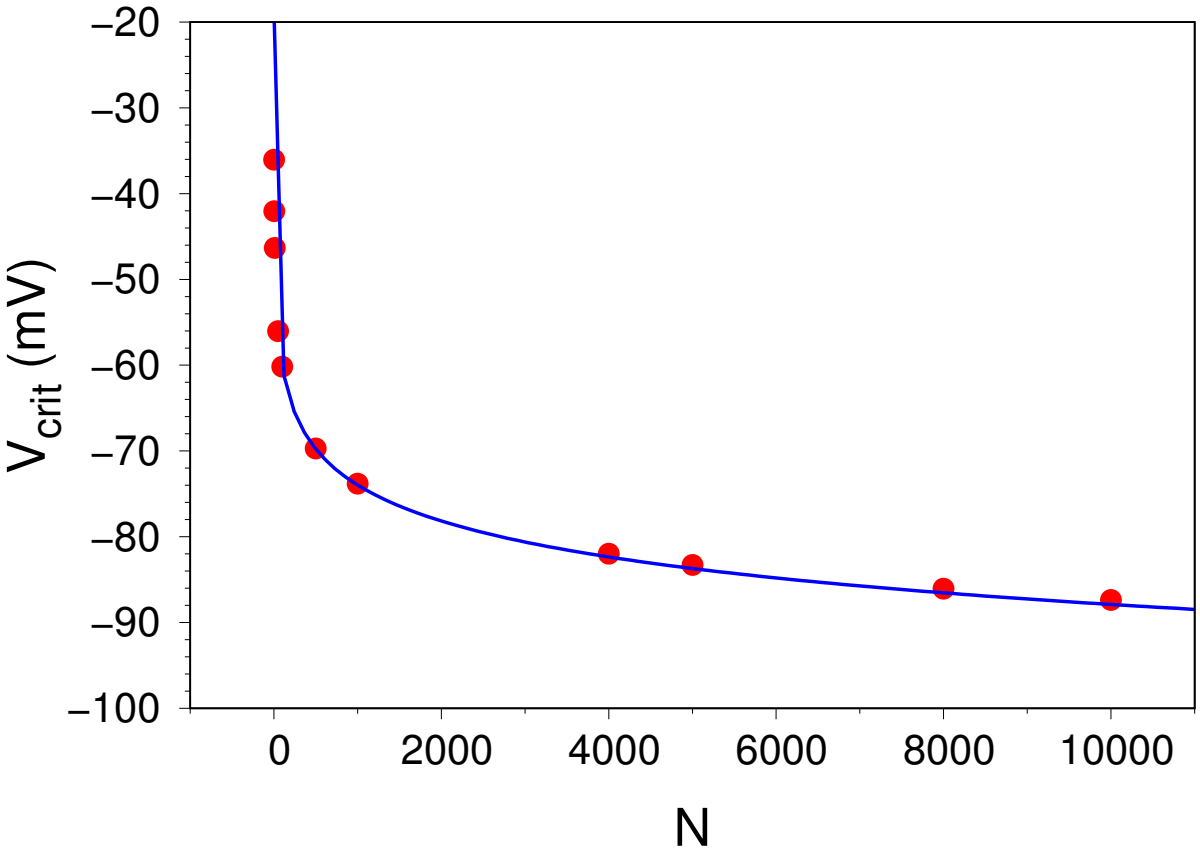

Figure 4.12: Numerically calculated relation between the number of channels in the system and the threshold, using steady state opening probabilities and no leak. The blue fit is logarithmic with coefficient $-kT/2q$ (Eq. (4.6)) [1].

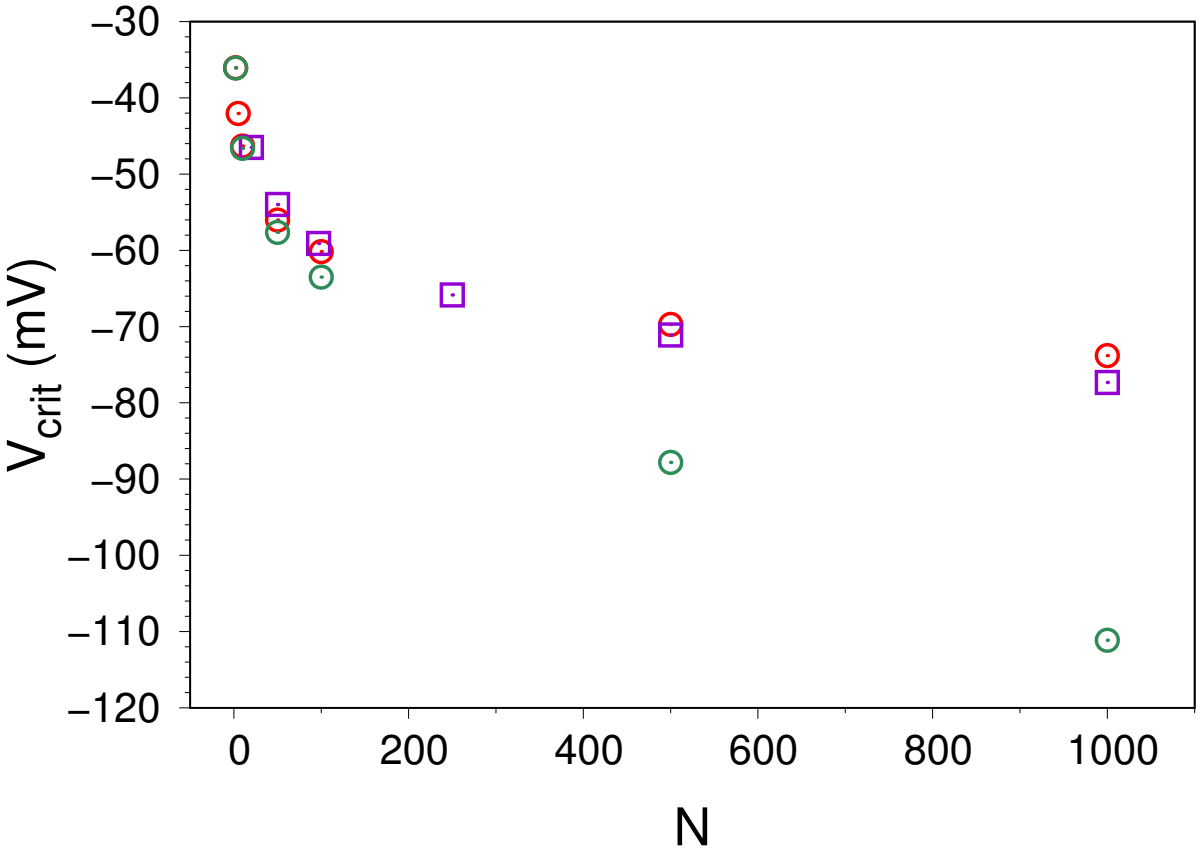

Figure 4.13: When a leak χ_ℓ is introduced into the system, the threshold voltage is depressed. The red circles are from Fig. 4.12 ($\chi_\ell = 0$), and the green circles are with $\chi_\ell/\chi = 10^{-3}$, both calculated using steady state opening. The purple squares were simulated with the full model Eqs (3.2), (3.7) and $\chi_\ell/\chi = 9.1 \times 10^{-5}$, they agree extremely well with the steady state result for the same value of χ_ℓ (not plotted). All parameters are identical to Fig. 4.12.

4.5 Discussion

When considering the Artificial Axon purely from the perspective of threshold firing, i.e. without considering the shape or dynamics of the action potential after depolarization, the system can be modeled as a 1D dynamical system using the equilibrium opening rate $p_e(V)$. It can be explicitly shown that the system passes through a saddle-node bifurcation when V_{clamp} is stepped above threshold, with critical slowing down occurring near the threshold due to the remnant of a fixed point. This slowing down scales with the distance to threshold $(V_{clamp} - V_{crit})$ with an exponent of -1/2 and is observable in the physical AA. However, as a result of the limited range of the scaling behavior in the experiments, the critical exponent cannot be determined with high accuracy. In the simulated system where there is no issue of stability and noise, a much larger scaling range is observed, and correspondingly a better determination of the scaling exponent follows. The numerical results match the theoretical prediction for the scaling exponent, while also matching the experimental findings in the range where they overlap. Simulations further show that experimental limits which arise due to issues of stability and noise are not the only factors which cause deviations from power law scaling, but that there is also an intrinsic dynamical effect which has a large influence on the scaling behavior close to the threshold: channel inactivation.

Physically, channel inactivation restricts the range where scaling is observed, similar to finite size effects in other condensed matter systems. The "finite size" is here the finite number of channels (more precisely the finite total conductance with open channels, $N_0\chi$), which prevents arbitrarily long delay times. However, channel inactivation does not change the nature of the bifurcation and therefore does not change the scaling exponent, as is evident from the simulation (Fig. 4.10), which contains inactivation dynamics but still gives a scaling exponent of almost exactly $-1/2$. The simulations also demonstrate the 'stability' of the scaling exponent, in that significantly varying the rates and conditions do not alter

the scaling behavior correspondingly. This is to be expected since the scaling phenomenon arises from the saddle-node nature of the critical point, which is universal.

It is interesting to note that if the experimental data from Fig. 4.7 are taken and plotted with the simulated threshold rather than the fitted threshold, a scaling exponent much closer to the theoretical one is obtained. This further supports the reasoning for the deviation in experimental behavior (i.e. the drift in voltage threshold as over the course of an experiment). The reasoning is that if a drift had occurred, it would have likely decreased the voltage threshold over time, as channels floating above the lipid membrane tend to inserted over time, increasing the number of channels in the system. As such, a simulation using fits on the first few data points would be well suited to provide an estimate for how the system would behave in the absence of this drift. The simulation rates are obtained from fits on the spikes closest to the critical point, which were the data points first recorded in the experiment.

In summary, scaling behavior of the delay time τ extending infinitely close to the critical point is a property of the 1D dynamical system Eq. (4.1). The 3D dynamical system Eqs. (3.2), (3.7), which provides a good description of the dynamics of the physical AA, reduces to the 1D dynamical system Eqs. (4.5), (4.6) in the limit of fast channels without inactivation. The latter system is equivalent to Eq. (4.1) in the vicinity of the critical point, meaning it has exactly a saddle node bifurcation and thus also exhibits scaling extending infinitely close to the critical point, this corresponds to similar firing behavior in real neurons [20, 28, 35, 36, 37, 38]. However, this is only an approximation of the 3D system, the question then arises whether the latter, and the physical system it represents, also exhibit the same scaling properties. The results in this chapter indicate that the scaling exponent of $-1/2$ is indeed robust, but the scaling range of the 3D system is limited. This restricted range as analogous to finite size effects, as reasoned above. Finally, note that the findings here pertain only to the system with regards to behavior near the threshold for firing. The Artificial

Axon as modeled by Eqs. (3.2), (3.7) in its full form displays several other transitions to spiking in different regions of parameter space, these will be detailed in the following chapter.

CHAPTER 5

Artificial Axon: A Dynamical Systems Perspective

Motivated by the desire to generate interesting dynamics with the AA and understand the types of behavior available to the system, a numerical analysis of the minimal model developed in Ch. 3 is conducted in this chapter. We begin with the construction of a phase diagram for the AA through simulations of the model, identifying regions in parameter space which give rise to different types of voltage dynamics. The goal is to qualitatively place the present experimental system in the phase diagram and understand the criteria on channel properties necessary for obtaining desired behaviors, such as single channel oscillations. Along the way, bifurcations which separate the different regions in the phase diagram will be explored, along with other intriguing features of the dynamical system, including a transition which may not have been described before in other electrophysiological models.

5.1 The Artificial Axon as a 3D Dynamical System

The dynamics of the AA with KvAP as the ion channel is modeled by the following set of equations (Ch. 3):

$$\begin{aligned}
\frac{dV}{dt} &= \frac{N_0\chi}{C}\, p_o(t)\,[V_N - V(t)] + \frac{\chi_c}{C}\,[V_c - V(t)] \\
\frac{dp_o}{dt} &= [1 - p_o(t) - p_i(t)]k_o(V) - p_o(t)[k_c(V) + k_i(V)] \\
\frac{dp_i}{dt} &= p_o(t)k_i(V) - p_i(t)k_r(V)
\end{aligned} \tag{5.1}$$

Eqs. (5.1) being a slightly modified version of Eq. (3.2) more suited for theoretical discussions. The leak conductance is neglected ($\chi_\ell << \chi$), and R_c is rewritten as an equivalent conductance term χ_c, for consistency with χ. Eqs. (5.1) form the 3D dynamical system which describes the AA, but even in this minimal representation the parameter space is still high dimensional, making direct analysis rather difficult. Progress can be made by identifying and focusing on the most relevant parameters with respect to the experiments. The control parameters in the experiment are V_c, the clamp voltage, and χ_c, the clamp conductance, and the effective rates of Fig. 3.1, which define the suitability of the channel for obtaining interesting dynamical behavior, such as autonomous firing. In general (and specifically for the KvAP) $k_o, k_c \gg k_i, k_r$, and so the most relevant parameters are then the clamp voltage, the clamp conductance [39], and the rates of inactivation and recovery. The focus in subsequent sections will be on the parameter space spanned by these four quantities.

5.1.1 Phase Diagram

In order to understand the requirements on channel dynamics to obtain various temporal patterns, a phase diagram can be constructed to explore the dynamical behavior of Eqs. (5.1), representing a single AA. For an initial discussion of the qualitative aspects of the system, k_i, k_r are first taken as constant (independent of voltage). Thus only the opening and closing rates are coupled to the voltage. The result is a 4D parameter space spanned by V_c, χ_c, k_i, and k_r. Fig. 5.1 shows one representation of the phase diagram, namely a cut through parameter space in the plane of k_r and k_i, for $V_c = -50\,\mathrm{mV}$, $\chi_c = 500\,\mathrm{pS}$. The diagram is obtained by simulating the AAs with the given parameters at each point on the plane and recording the firing rates of the time traces. The protocol to fire the AA is the same as previously discussed; starting with the system clamped at a large negative resting potential, V_c is stepped up to an above threshold value to fire. The remaining parameters of the simulation are shown in Table 5.1.

We identify four regions of distinct behavior, as labeled in Fig 5.1. In Region I, the

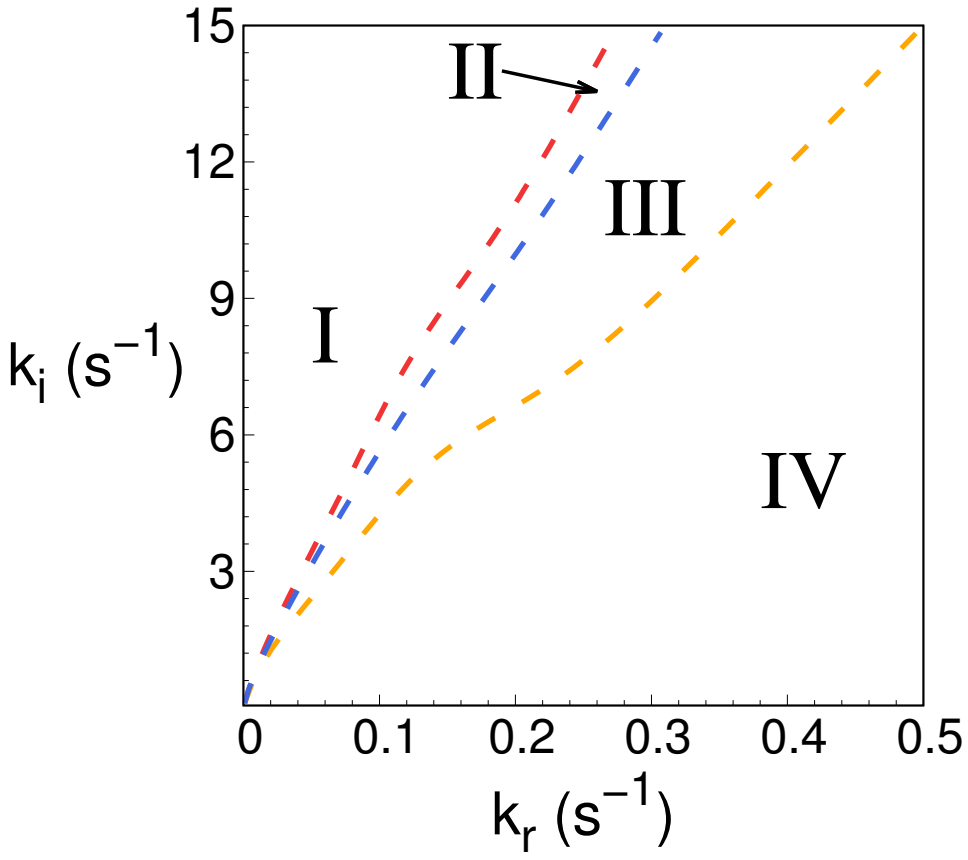

Figure 5.1: Phase diagram of the dynamic behavior obtained from simulating the model Eqs. (5.1), with voltage independent inactivation and recovery rates k_i and k_r. The phase plane shown is a cut through a higher dimensional parameter space, for $\chi_c = 500\,\text{pS}$ and $V_c = -50\,\text{mV}$. Four distinct regions of behavior are identified.

N_0	C	χ	χ_ℓ/χ	V_N	χ_c	$k_{co}(+), k_{oc}(-)$	$V_c(t=0)$
250	330 pF	170 pS	4.18×10^{-4}	42 mV	500 pS	$0.3\, e^{\pm 106(V+0.018)}$	-200 mV

Table 5.1: Simulation parameters for the 3D dynamical system. The system is simulated with the initial state of $V = -200$ mV, $p_c = 1$.

dynamical system Eqs. (5.1) produces large, repeating action potential which reach close to the Nernst potential (i.e. spike trains). The firing rate increases as k_r increases, while the width of the AP decreases for increasing k_i. In Region II the system exhibits "oscillations", distinct from behavior in Region I in that the firing rate is higher, and with exception of the first peak, the amplitude is smaller. The transition from Region I to Region II is quite interesting; depending on the control parameters χ_c and V_c, there can be either a sharp jump in firing rate or a smooth continuous increase. This transition is discussed further in the next section. Fig. 5.2 showcases representative behavior in these two regions.

Region III corresponds to damped oscillations, the damping increasing as k_r increases, corresponding to a collapse of the stable limit cycle to a single fixed point. Finally, in Region IV the system fires only once, after which the voltage remains constant at a relatively high value; here the system moves directly to the fixed point without spiraling (overdamped). Representative examples of these two regions are shown in Fig. 5.3.

In summary, for the case that the inactivation and recovery rates are voltage independent, there are four possiblebehaviors when the system is excited (i.e. stepped above threshold from rest): AP trains, oscillations, damped oscillations, and single shot firing. This phenomenology of the AA, possessing only one channel species with inactivation, is the same as for the Morris-Lecar system which possesses two channel species without inactivation [20, 40, 41].

The phase diagram of Fig. 5.1 is representative of the system; while it is only one slice through a higher dimensional parameter space with the two control parameters V_c and χ_c held fixed, taking a different slice in parameter space (e.g. χ_c vs V_r, k_i vs χ_c, etc) will yield the same regions of behavior. Changing these control parameters (or the other parameters, such as C, N_0, etc) shifts the boundary lines in the k_i, k_r plane but does not fundamentally alter the possible behaviors.

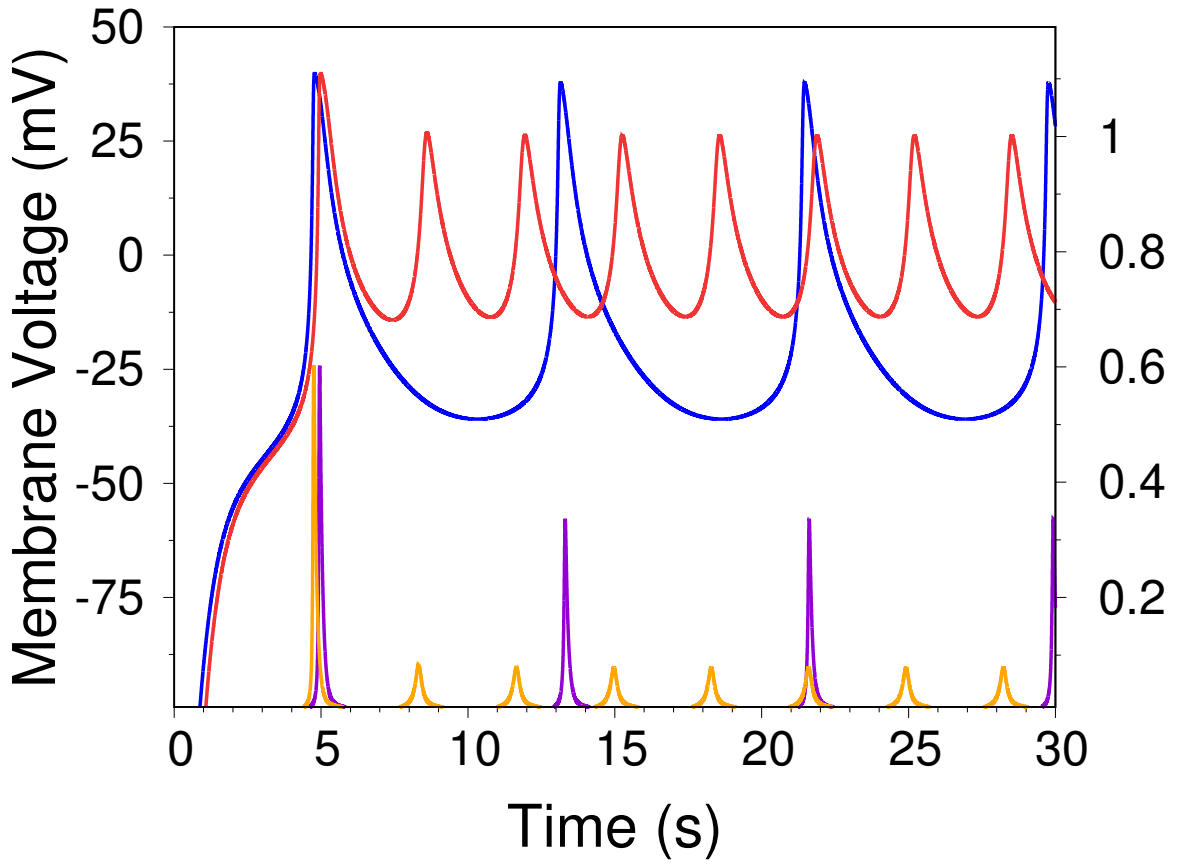

Figure 5.2: Two representative time traces of the voltage independent model, illustrating the sharp increase in frequency as one crosses from Region I to Region II in the phase diagram of Fig. 5.1. The blue trace has $k_r = 0.18\,\mathrm{s}^{-1}$ while the red trace has $k_r = 0.19\,\mathrm{s}^{-1}$, with all other parameters identical ($k_i = 10.4\,\mathrm{s}^{-1}$). The purple and orange traces show the probability that channels are open (p_o) for the blue and red traces respectively, with scale on the second y-axis.

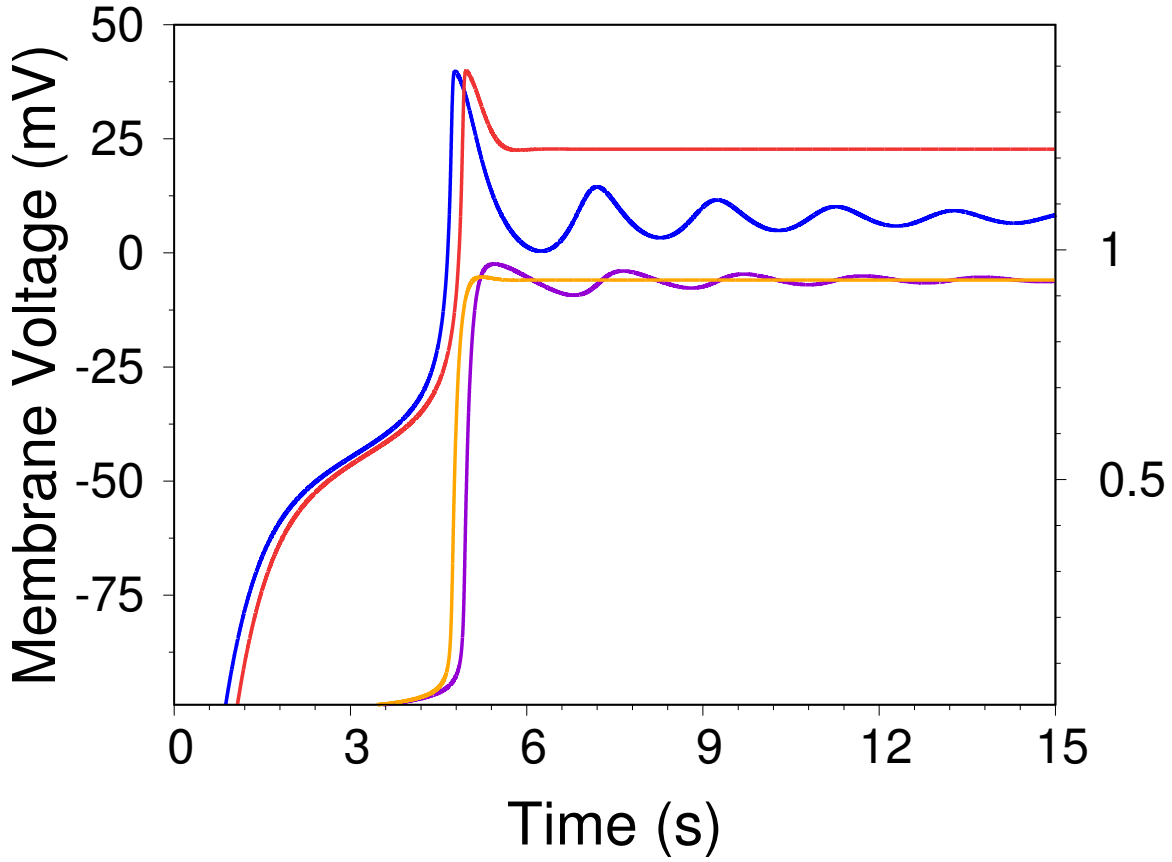

Figure 5.3: Two additional time traces of the voltage independent model, displaying damped oscillations and single shot AP behavior. The blue trace ($k_r = 0.22\,\mathrm{s}^{-1}$) corresponds to Region III of the phase diagram of Fig. 5.1, the red trace ($k_r = 0.5\,\mathrm{s}^{-1}$) to Region IV. The purple and orange traces display the corresponding probability that the channels are inactive, p_i. Parameters other than k_r are identical to Fig. 5.2.

5.1.2 Phase Transition

A point of particular interest in the phase diagram is the nature of the transition between regions I and II. Fig. 5.4(a) shows the firing rate vs k_r for four different values of V_c, with fixed $k_i = 10.4\,\mathrm{s}^{-1}$, $\chi_c = 500\,\mathrm{pS}$. Each curve is a crossing between Region I and Region II on a particular cut of the phase plane k_r, k_i, with the orange curve ($V_c = -50\,\mathrm{mV}$) corresponding to Fig. 5.1. The lower part of each curve corresponds to AP trains in Region I, while the upper points are of oscillations in Region II. For $V_c = -54\,\mathrm{mV}$ a sharp transition is seen around $k_r \approx 0.21\,\mathrm{s}^{-1}$, where the firing rate increases steeply. This transition smooths out as V_c is raised to higher values, with the transition point moving to lower values of k_r. The same transition is present in other cuts of the parameter space as well. Fig. 5.4(b) depicts a similar situation, with the roles of k_i and V_r swapped. Here the transition point in k_r shifts more drastically while the change in sharpness is less prominent, however the phenomenology remains identical.

5.2 The Reduced 2D Dynamical System

Displaying phase space trajectories often gives better insight into the nature of a bifurcation. In the Hodgkin-Huxley model, a standard technique is to reduce the system to two dimensions in order to plot the trajectories on a plane [8]. The same approach can be applied here, provided care is taken to preserve the dynamics. Specifically, in the regime $k_i, k_r \ll k_o, k_c$, the 3D system Eqs. (5.1) can be reduced to 2D by introducing a new coordinate $p_a(t)$, the probability that channels are "active" (i.e. not inactive: open or closed, $p_a = p_o + p_c$). Since the interconversion C $\rightleftharpoons$ O is fast with respect to other timescales in the system, $p_o(V,t)$ can be substituted by $p_a(t)p_e(V)$ in Eqs. (5.1), where $p_e(V)$ is the equilibrium opening probability in the absence of inactivation as defined in Ch. 3.

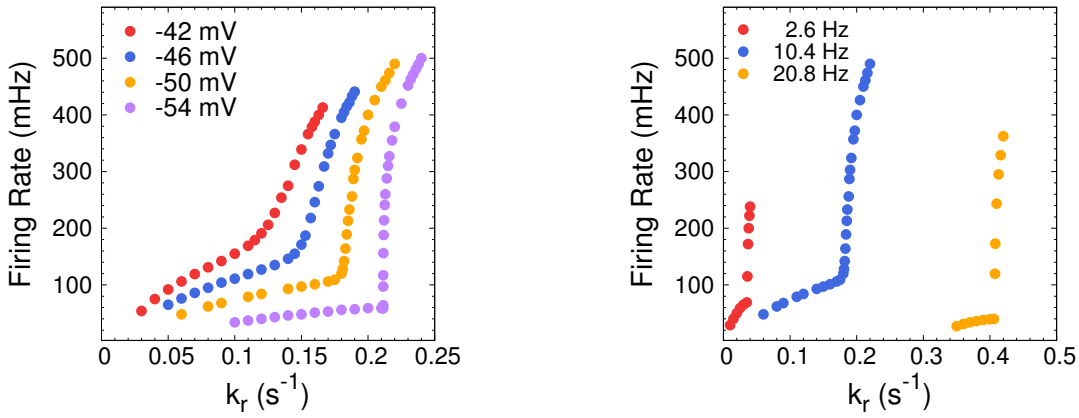

(a) (b)

Figure 5.4: **(a)** Firing rate as a function of k_r for several values of V_c (legend) with $k_i = 10.4\,\mathrm{s}^{-1}$. A clear transition is seen (Region I to Region II), with the critical value of k_r and sharpness of the transition depending on the clamp strength. **(b)** Firing rate as a function of k_r, same as (a), but with three different k_i (legend) and fixed $V_c = -50\,\mathrm{mV}$. The transition seen in (a) is also present here. For both plots, $\chi_c = 500\,\mathrm{pS}$.

$$p_e(V) = \frac{1}{1 + e^{-\frac{2q}{kT}(V - V_0)}} \tag{5.2}$$

Using $p_a(t) + p_i(t) = 1$, the lower two equations in Eqs. 5.1 can then be replaced by a single equation for p_a, reducing the system to two dimensions. Taking it a step further, the system can be recast in dimensionless form to standardize the subsequent analysis. Eq. (5.1) suggests the choice of $\tau = C/(N_0\chi)$ as the time scale and V_N as the voltage scale. Writing the total channel conductance $N_0\chi$ as χ_0 (so $\tau = C/\chi_0$), Eq. (5.1) can be made dimensionless by dividing all voltages by V_N and scaling by τ. Similarly, the rates become dimensionless when scaled by τ, e.g. $\tilde{k_r} = \tau k_r$. With these changes, the 3D dynamical system is transformed into a dimensionless 2D dynamical system in terms of the coordinates $V(t)$, $p_a(t)$:

$-2q/kT$	V_0	N_0	C	χ	$p_a(t=0)$	$V(t=0)$
4	-0.2	50	300 pF	200 pS	1	-1

Table 5.2: Parameters for simulations of the 2D dynamical system. The initial condition of the system is above threshold, so firing begins immediately. Note that N_0, C, and χ are only for recovering dimensional quantities from the results if needed; they are not necessary for the simulation.

$$\begin{aligned} \frac{dV}{dt} &= p_a(t)\, p_e[V(t)]\,[1 - V(t)] + \chi_c\,[V_c - V(t)] \\ \frac{dp_a}{dt} &= k_r - k_r \left[1 + \frac{k_i}{k_r} p_e[V(t)]\right] p_a(t) \end{aligned} \tag{5.3}$$

where all terms are implicitly dimensionless, i.e. $V/V_N \to V$, $t/\tau \to t$, $\chi_c/\chi_0 \to \chi_c$, etc. Numerically, taking some "standard" values for the experimental parameters, $C = 300\,\text{pF}$, $\chi = 200\,\text{pS}$, $N_0 = 100$, the time scale is $C/(N_0\chi) = 1.5 \times 10^{-2}\,\text{s}$; so for example the (dimensional) rate $k_r = 0.2\,\text{s}^{-1}$ corresponds to the dimensionless rate $(Ck_r)/(N_0\chi) = \tau k_r = 3\times10^{-3}$. If the parameters (q, V_0) of Eq. (5.2) which define the open probability function $p_e(V)$ are fixed, then the 2D dynamical system Eq. (5.3) once again depends only on the four control parameters χ_c , V_c , k_r, and k_i/k_r; the first three of which are analogous to the same χ_c, V_c, k_r in the 3D system.

Referring to Fig. 5.1 as a guide, the nature of the transitions in the system can be elucidated by sampling points along a horizontal line across the phase diagram, i.e. for fixed choices of (V_c, χ, k_i) excite the system at various values of k_r and record the resulting firing rates. The relevant simulation parameters are given by Table 5.2.

For the fixed values $V_c = -1.7$, $k_i = 0.15$, and $\chi_c = 0.05$, the behavior of Region I in Fig. 5.1 (AP trains) is seen in the interval $4.03 \times 10^{-3} \lesssim k_r \lesssim 9.20 \times 10^{-3}$. Fig. 5.5(a) shows

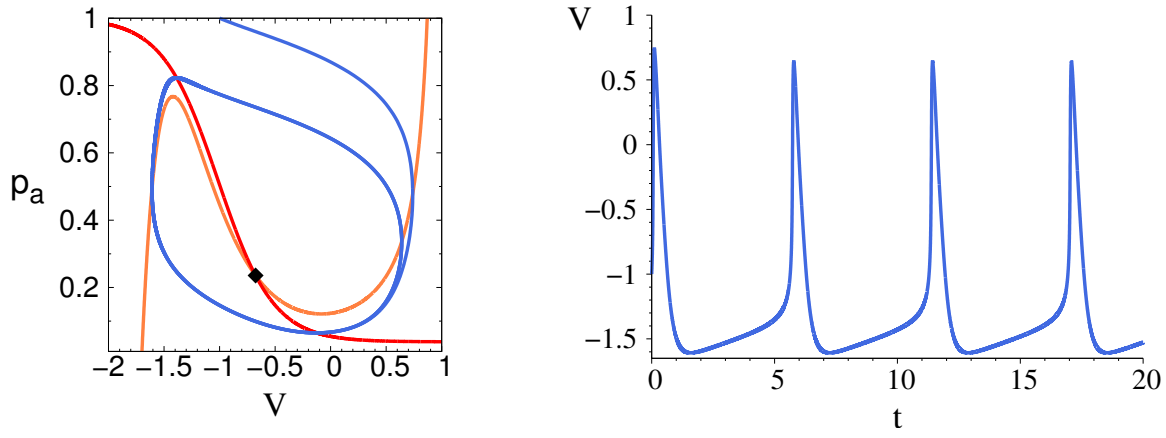

(a) (b)

Figure 5.5: **(a)** Phase space trajectory (blue) in the V, p_a plane for the 2D dynamical system, displaying the limit cycle corresponding to an AP train, with $k_r = 6.0 \times 10^{-3}$, $k_i = 0.15$, $V_c = -1.7$, and $\chi_c = 0.05$. Also shown are the nullclines $dp_a/dt = 0$ (red) and $dV/dt = 0$ (orange). **(b)** Time trace of the AP train corresponding to the limit cycle shown in (a).

the phase space trajectory for $k_r = 6.0 \times 10^{-3}$, which is a limit cycle, the corresponding AP train is shown in Fig. 5.5(b).

For $k_r \geq 9.21 \times 10^{-3}$ the system exhibits damped oscillations, corresponding to the behavior of Region III in the phase diagram. The transition between AP trains and damped oscillations is sharp. Fig. 5.6 shows the same quantities as Fig. 5.5, for $k_r = 9.20 \times 10^{-3}$, which is in Region II, close to the transition to Region III (note the difference in spike shape compared to Fig. 5.5(b)). Fig. 5.7 shows these plots for $k_r = 9.21 \times 10^{-3}$, on the other side of the transition in Region III. Here the phase space trajectory spirals into the (stable) fixed point, corresponding to damped oscillations of $V(t)$. Note that with the above parameter values (specifically, the relatively small k_i) the system did not cross through Region II. Rather, the transitions $I \rightarrow II$ and $II \rightarrow III$ have "merged", in the sense that the transition from AP trains to damped oscillations is also accompanied by a steep increase in frequency (Figs. 5.6(b), 5.7(b)). The phenomenology just described is that of a subcritical

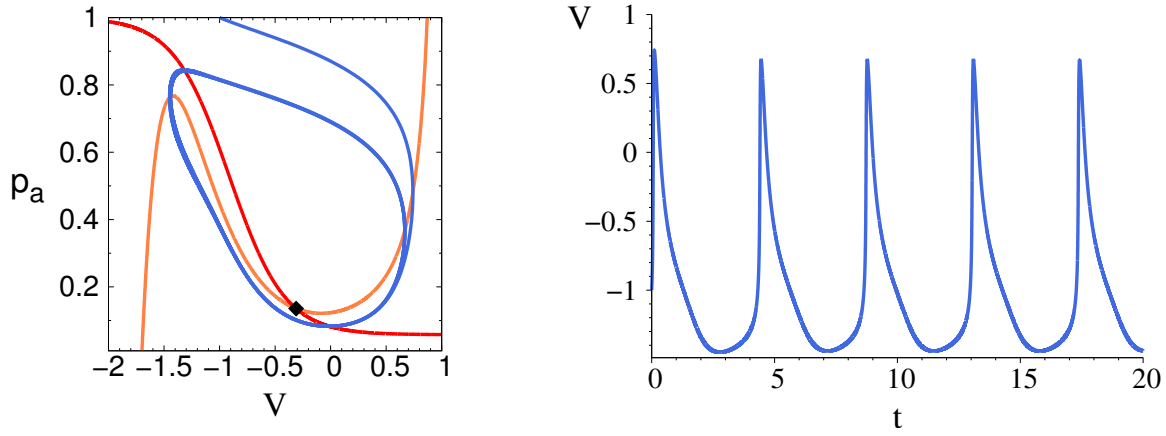

(a) (b)

Figure 5.6: **(a)** Phase space trajectory for $k_r = 9.20 \times 10^{-3}$ (other parameters are same as in Fig. 5.5), just inside Region I. **(b)** Time trace of the trajectory shown in (a).

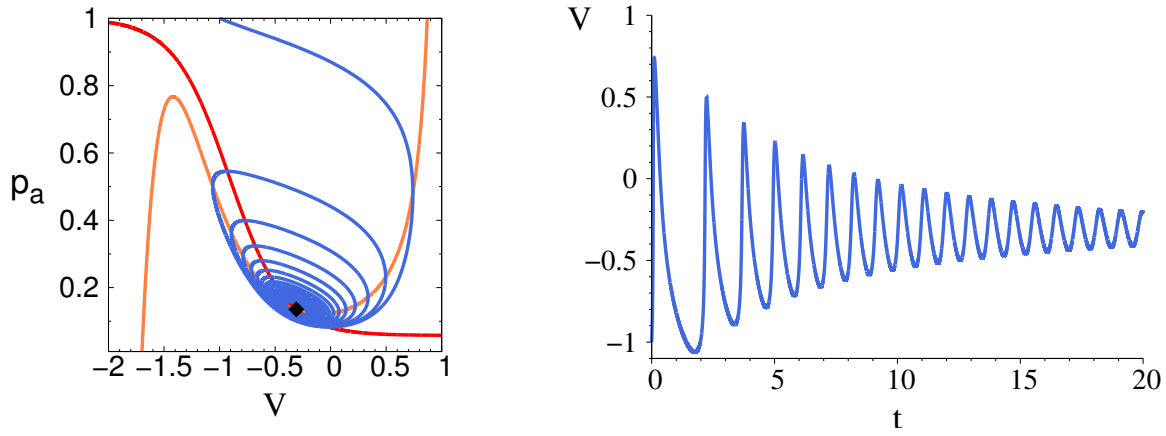

(a) (b)

Figure 5.7: **(a)** Phase space trajectory for $k_r = 9.21 \times 10^{-3}$ (other parameters are same as in Fig. 5.5), just outside Region I. There is no longer a stable limit cycle and trajectory spirals into the stable fixed point. **(b)** Time trace of the trajectory shown in (a).

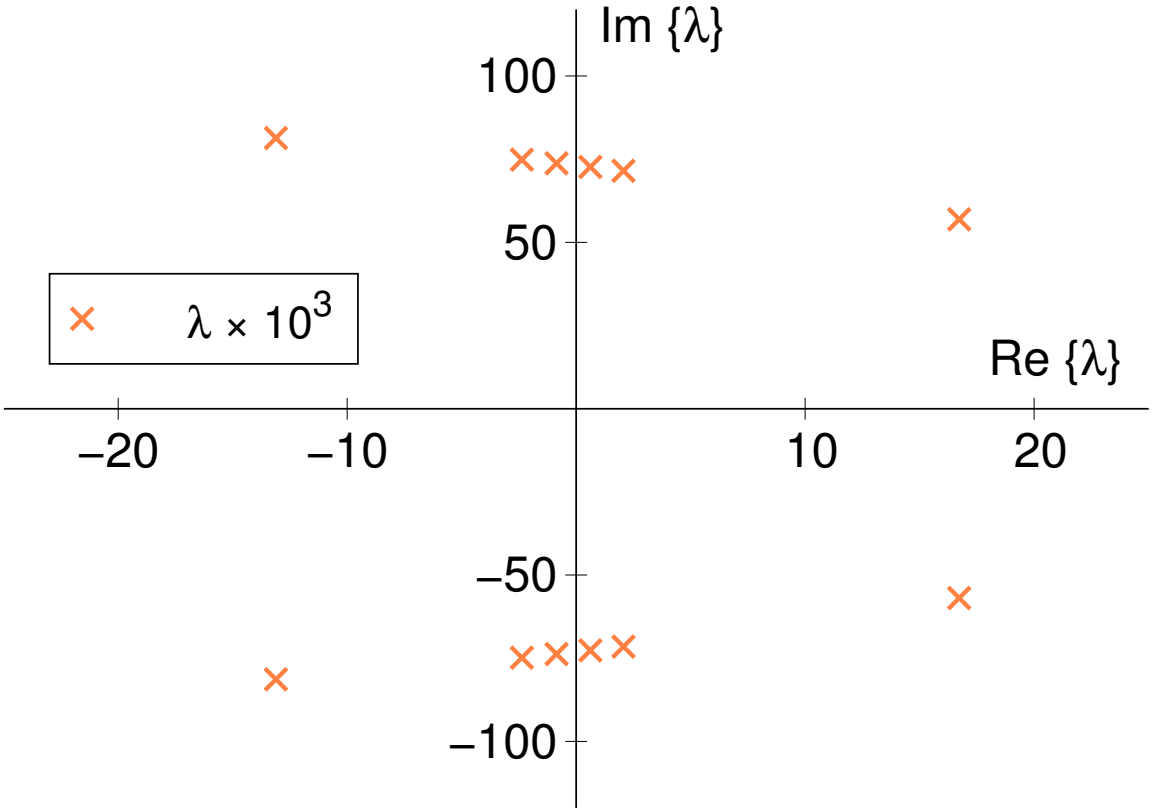

Figure 5.8: Eigenvalues λ of the stability matrix at the fixed point, calculated numerically for the dynamical system Eqs. (5.3) for different values of k_r. From left to right, the points correspond to: $k_r = (10.0, 9.30, 9.20, 9.10, 9.0, 8.0)\times 10^{-3}$. Other parameters are as in Fig. 5.5.

Hopf bifurcation [33]. The linear stability analysis of the fixed point close to the bifurcation shows that the eigenvalues of the stability matrix form a complex conjugate pair and cross the imaginary axis from right to left as the fixed point changes from unstable to stable. The eigenvalues λ (real and imaginary part) are shown in Fig. 5.8 for different values of k_r near the bifurcation. With the parameter values of this section, the bifurcation point is at $k_r \approx 9.21 \times 10^{-3}$, as expected.

For $k_r \gtrsim 12 \times 10^{-3}$ (not shown) the system is so heavily damped that there are no

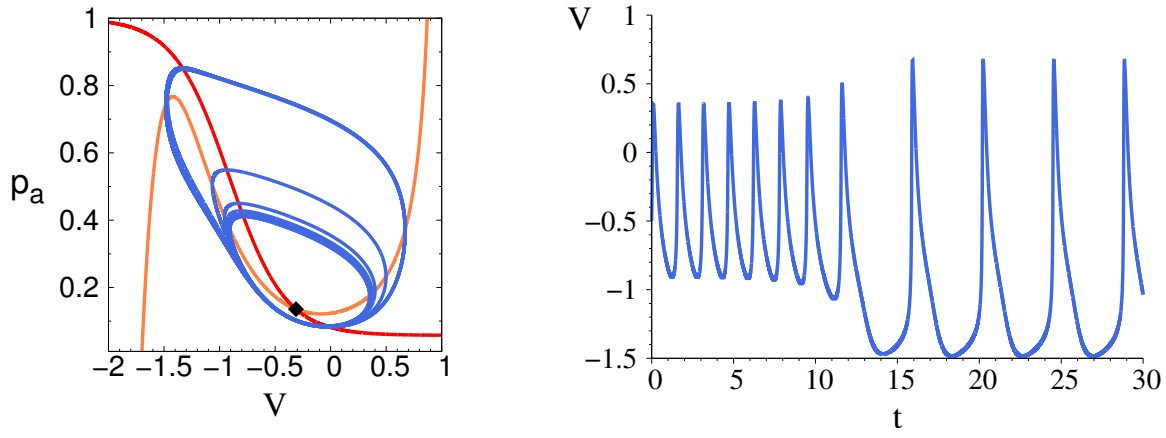

Figure 5.9: **(a)** Limit cycle for $k_r = 9.18 \times 10^{-3}$ with the initial state ($V = -0.5$, $p_a = 0.39$), showing the presence of an unstable limit cycle. Other parameters are same as in Fig. 5.5. **(b)** Time trace of the trajectory shown in (a).

oscillations; depending on the initial conditions, it either approaches the fixed point value from one side or fires once and then approaches the fixed point. This is the behavior of Region IV of Fig. 5.1, the transition into this region being one from the underdamped to the overdamped regime.

In general, the behavior of the system is independent of the choice of initial conditions. Since there is only one fixed point, for any starting point $(V(0), p_a(0))$ the system either spirals into the fixed point, if it's stable, or moves to the limit cycle. However, there are exceptions to this near the Hopf bifurcation. Fig. 5.9 shows such a case. The system starts at $(V, p_a) = (-0.5, 0.39)$, which is close to the fixed point. The trajectory travels outwards and makes several loops before stabilizing at the larger stable limit cycle. A trajectory which starts slightly closer to the fixed point would instead spiral inward. This bistability arises from the presence of an unstable limit cycle which is in between the stable fixed point and stable limit cycle. For k_r values far from the Hopf bifurcation, this phenomenon is not seen because the fixed point itself is unstable.

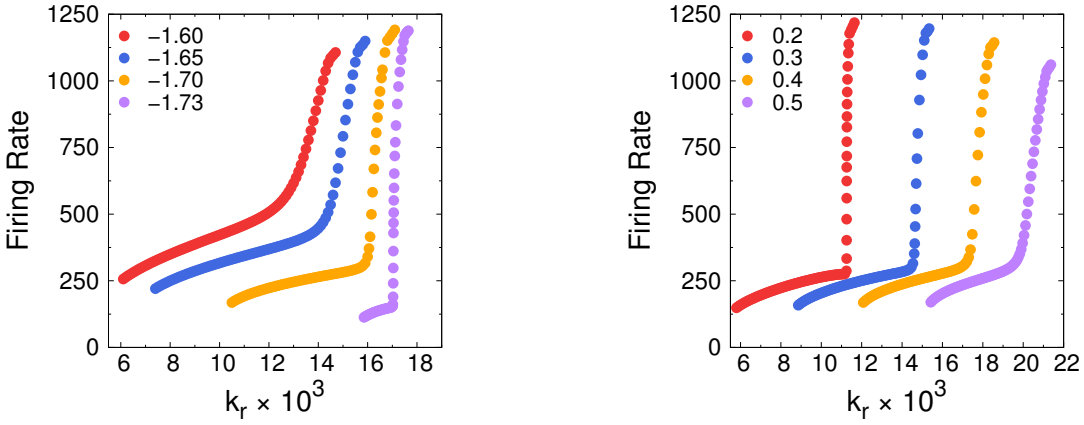

(a) (b)

Figure 5.10: **(a)** Firing rate for the reduced 2D model as a function of k_r, varying V_c (legend) with $k_i = 0.35$ and $\chi_c = 0.05$ held fixed. The phenomenology is the same as for the 3D system. In particular, there is a sharp transition for a critical value of V_c. **(b)** The same transition displayed for fixed $V_c = -1.7$, $\chi_c = 0.05$ and different values of k_i (legend).

By moving up in the phase diagram, i.e. increasing k_i, the existence of Region II in 2D system can be shown as well. Fig. 5.10, which is analogous to Fig. 5.1, but obtained for the 2D system, demonstrates this. In Fig. 5.10(a) the firing rate vs k_r is plotted with fixed $k_i = 0.35$ and different values of V_c. It is evident that the phenomenology remains the same as the 3D system: at a critical value of V_c the transition is sharp, and it smooths out as V_c is raised, with the transition shifting to smaller values of k_r. Fig. 5.10(b) displays the same transition for fixed V_c and different values of k_i.

Figs. 5.11, 5.12 show representative phase space trajectories and time traces across the Region I $\rightarrow$ Region II transition, for the 2D system. Different from the Hopf bifurcation corresponding to the transition II $\rightarrow$ III, the fixed point inside the limit cycle remains unstable on both sides of the transition. This is confirmed by an analysis of the eigenvalues of the stability matrix at the fixed point, which remain on the right side of the imaginary axis in both cases.

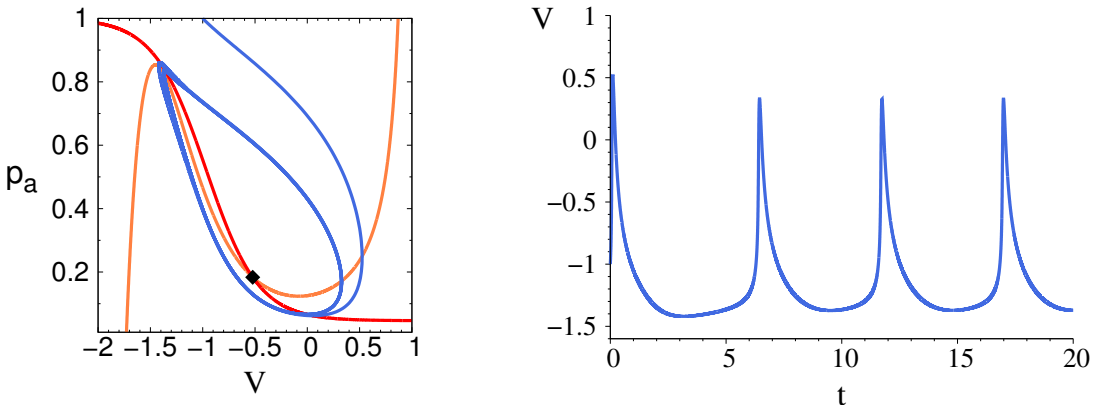

(a) (b)

Figure 5.11: Phase space trajectory (a) and corresponding time trace (b) for the 2D system just prior to the I $\rightarrow$ II transition. $k_r = 17.03 \times 10^{-3}$, $k_i = 0.35$, $V_c = -1.73$, $\chi_c = 0.05$.

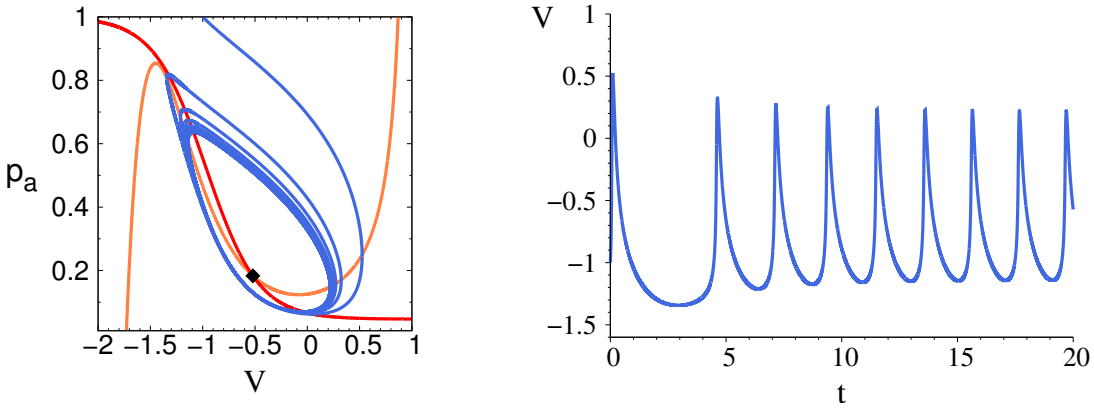

(a) (b)

Figure 5.12: Phase space trajectory (a) and corresponding time trace (b) for the 2D system just after the I $\rightarrow$ II transition. $k_r = 17.05 \times 10^{-3}$, $k_i = 0.35$, $V_c = -1.73$, $\chi_c = 0.05$

In addition to the subcritical Hopf bifurcation, the system also contains a few other bifurcations which are similar to those of the Morris-Lecar system [40, 41]. These will be described briefly, using k_i as the bifurcation parameter: Starting at small k_i, there is one stable fixed point at the intersection of the V and p_a nullclines, which is globally stable. This corresponds to the system having no excitability, i.e. action potentials cannot be produced. As k_i increases, the V nullcline moves to the right, and a saddle-node bifurcation will occur when the two nullclines intersect at a second point, resulting in two additional fixed points post-bifurcation. As k_i is further increased, one of the newly created fixed points will annihilate with the original stable fixed point in another saddle-node bifurcation. This causes limit cycles to arise (Region I and Region II), as the only remaining fixed point is unstable. Finally, as k_i is increased further, the remaining fixed point becomes stable through the Hopf bifurcation described above and all trajectories spiral into it (Region III), until eventually no oscillations occur (Region IV).

The transitions explored in this section can also be found when following different trajectories in parameter space. Since the control parameters which have to do with channel rates are k_r and k_i/k_r, a natural trajectory is to keep the latter fixed. The overall picture remains the same: as an example, Fig. 5.13 depicts the firing rate vs k_r for fixed k_i/k_r.

5.2.1 Analogy to the Magnetization Transition

The plots of Fig. 5.4 and Fig. 5.10 present a qualitative resemblance to a number of equilibrium phase transitions. In Fig. 5.4(a), the firing rate ν vs k_r of the $V_c = -54\,\mathrm{mV}$ curve exhibits a sharp transition; for $k_r \geq k_r^c = 21.15 \times 10^{-2}\,\mathrm{s}^{-1}$, the system exhibits power law behavior, with $(\nu - \nu_c) \propto (k_r - k_r^c)^\beta$, with $\nu_c \approx 58\,\mathrm{mHz}$, and a scaling exponent $\beta \approx 0.317$ (Fig. 5.14). For $V_c > -54\,\mathrm{mV}$ the transition appears smoothed out. This resembles the behavior of the magnetization M vs temperature T for a ferromagnet close to the Curie

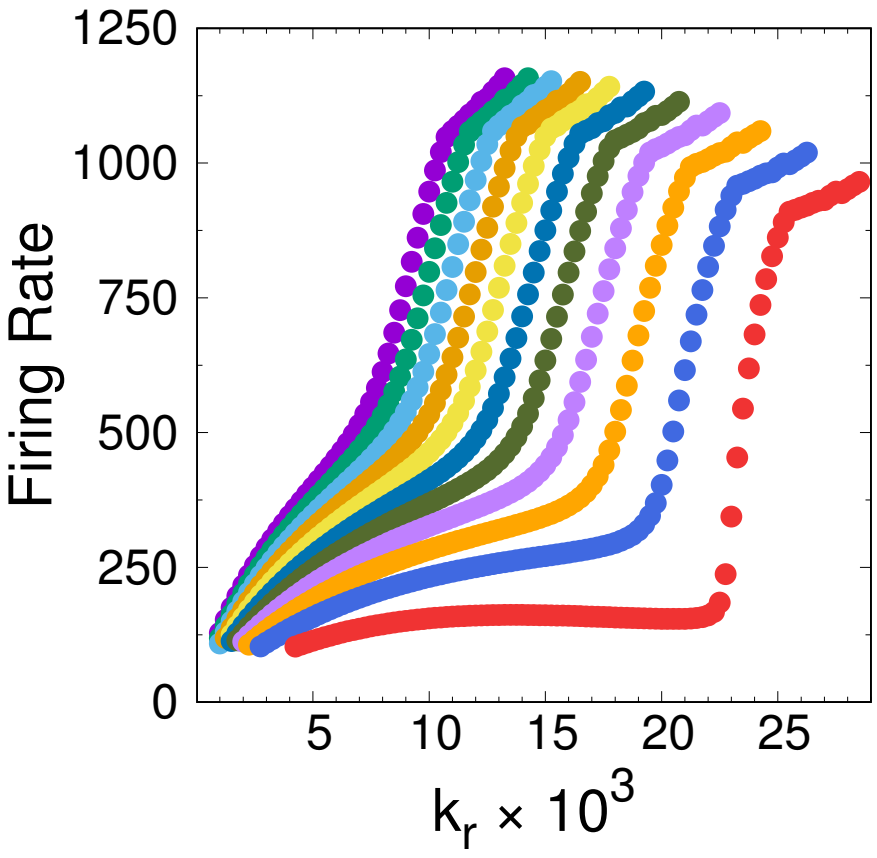

Figure 5.13: The transition from Region I to Region II in the 2D system, explored along trajectories with fixed $k_i/k_r = 25$. The different curves correspond to V_c in increments of 0.02, starting at $V_c = -1.52$ (violet) and ending at $V_c = -1.72$ (red).

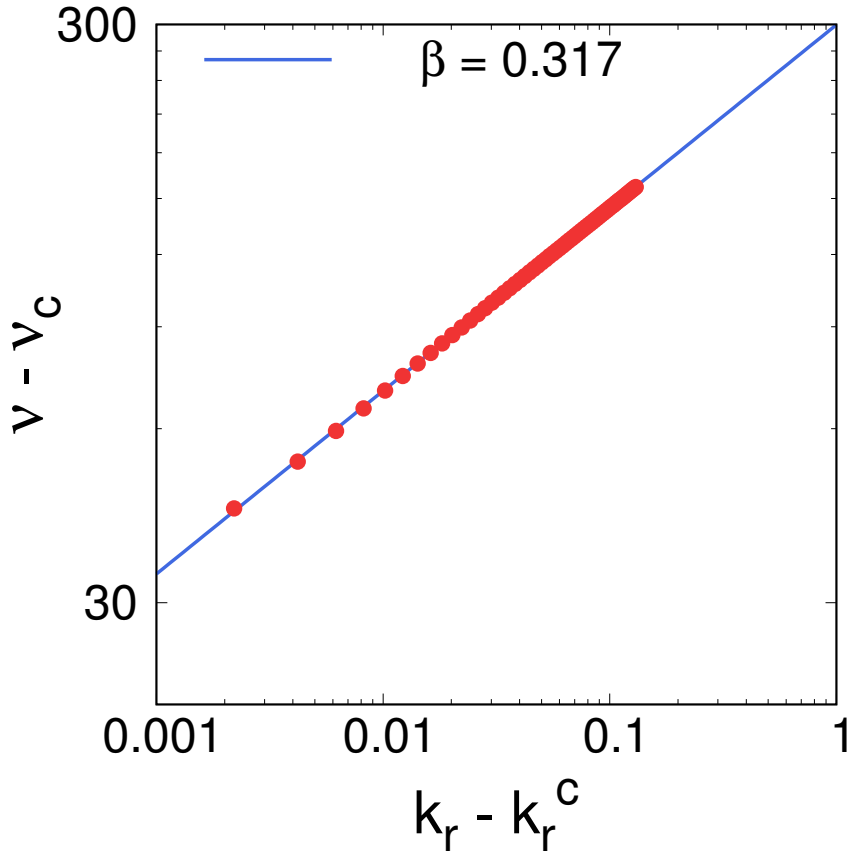

Figure 5.14: Scaling exponent for the firing rate as a function of the recovery rate, for Region II of the purple curve in Fig. 5.4. The critical values $k_r^{(c)}$ and ν_c were determined by starting with a value very close to the the I $\rightarrow$ II transition and making small adjustments until the points fall into a straight line.

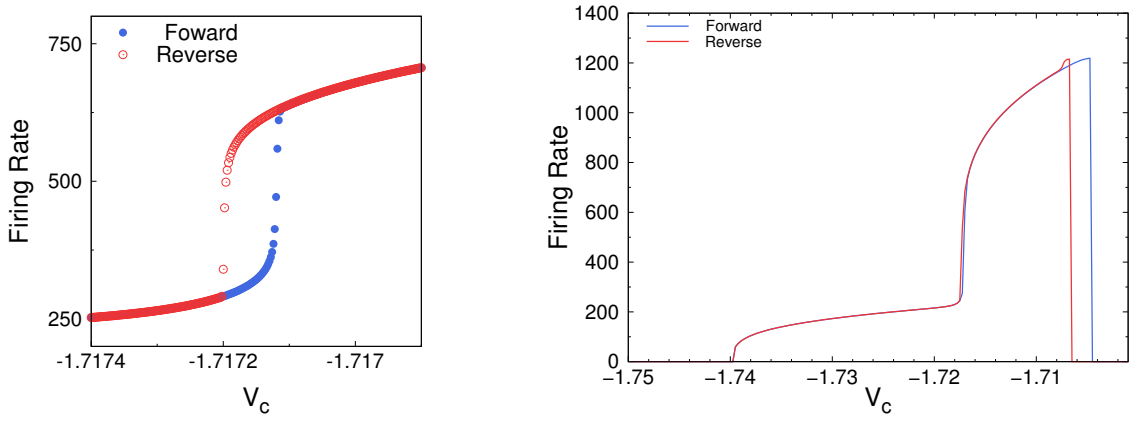

Figure 5.15: **(a)** Hysteresis in the firing rate of the 2D model. Starting with $\chi_c = 0.05$, $k_r = 13.4 \times 10^{-3}$, $k_i = 0.25$, and $V_c^{(i)} = -1.718$, the clamp value is increased in increments of 2×10^{-6} until $V_c^{(f)} = -1.716$ (2,000 total V_c values sampled), staying at each V_c value for $t = 20$ so that a firing rate can be calculated. The process is then reversed, with the clamp returning to initial value through the exact same intermediate values. **(b)** A zoomed out plot of the same transition in (a), showing the onset of oscillations ($V_c \approx -1.74$), as well as additional hysteresis at the subcritical Hopf bifurcation ($V_c > -1.71$). This plot was generated by sampling points from $V_c^{(i)} = -1.75$ to $V_c^{(f)} = -1.70$, with same parameters as in (a).

point. In zero external magnetic field ($H = 0$) the magnetization rises abruptly for $T < T_c$, exhibiting power law behavior $M \propto (T_c - T)^{\beta}$. Experimentally, the scaling exponent for systems in the Ising universality class is $0.31 \leq \beta \leq 0.33$; for the Ising model in 3D it is $\beta \approx 0.325$ [42].

For finite field ($H \neq 0$) the transition appears smoothed out in the M - T plane. With the correspondence $\nu \leftrightarrow M$, $k_r \leftrightarrow T$, $V_c \leftrightarrow H$, the plots in Fig. 5.4 resemble the magnetization vs temperature as the external field is turned on. For the magnetic system, a plot M vs H would display the phenomenon of hysteresis for $T < T_c$. The question to ask then, is whether the firing rate ν vs clamp voltage V_c could also show hysteresis, for $k_r < k_r^c$.

To investigate the occurrence of hysteresis in our model of the AA, the 2D voltage independent model is simulated in a slightly different way. The system begins in some initial state with χ_c, k_i, and k_r fixed, with an initial clamp value $V_c^{(i)}$. The clamp voltage is then increased "adiabatically" from this initial value to a final value $V_c^{(f)}$ over a time interval T, in uniform increments ($V_c^{(f)} > V_c^{(i)}$). The process is then reversed, with the clamp lowered from $V_c^{(f)}$ to $V_c^{(i)}$ over the same interval T. The firing rate is calculated for each time increment t ($t = T/N$ where N is the number of V_c values sampled between the initial and final values) and plotted as a function of V_c for both the forward and reverse processes. The results of this protocol show that, for certain parameter choices, there is a difference in firing rate between the forward and reverse processes in the vicinity of the I $\rightarrow$ II transition, i.e. a hysteresis loop in the $V_c - \nu$ plane. Fig. 5.15(a) shows the result for $\chi = 0.05$, $k_r = 13.4 \times 10^{-3}$, $k_i = 0.25$. The jump in firing rate corresponds to the I $\rightarrow$ II transition, and occurs at slightly different values of V_c depending on the system's direction of approach. Note that the hysteresis loop shown here is not due to the subcritical Hopf bifurcation in the system, which corresponds to the transition II $\rightarrow$ III. The existence of hysteresis at a subcritical Hopf bifurcation is well known [33], and occurs at slightly larger values of V_c. This can be seen in Fig. 5.15(b).

5.3 Voltage Dependent Inactivation and Recovery

It is interesting to ask how the dynamics change if k_i and k_r are instead voltage dependent, as is the case for the KvAP channel used in the experiment. Taking the voltage dependence to be of the Arrhenius form, $k = \kappa \exp[\alpha(V - V_0)]$, simulations of the system show that the phenomenology remains the same. The voltage dependent model produces the same four types of behavior (AP trains, oscillations, damped oscillations, and single shot AP) as found in the voltage independent model, for a wide range of parameter values. Fig. 5.16 shows example time traces from a system with voltage dependent inactivation and recovery rates: $k_i = 3\, e^{20V}$, $k_r = \kappa_r\, e^{-20V}$, $V_c = -56\,\mathrm{mV}$, and all other parameters identical to the voltage

independent model. In the figure, the system traverses through the four regions in the same fashion as before (I $\rightarrow$ II $\rightarrow$ III $\rightarrow$ IV) as κ_r is increased. Holding κ_r fixed and varying another parameter again produces the same four regions of behavior. Most notably, the sharp transition between Region I and Region II which was found in the voltage independent model is preserved (for certain parameter choices).

While the voltage dependent model more closely aligns with the experiment, it is not as useful for the purpose of analyzing the transitions between regions in the system, given that the voltage independent model has the same phenomenology with less parameters. Having shown that removing the voltage dependence from k_i and k_r does not fundamentally alter the available behaviors of the system, the preceding analysis on the model with constant k_i and k_r should remain applicable to the experiment.

5.4 Dynamics in the Experimental System

The rates measured in Ch. 3 can be approximately mapped on to the voltage independent phase diagram of Fig. 5.1 by considering the range of possible voltages encountered in the physical system. Typical experimental conditions are bounded from below by the resting voltage and above by the Nernst potential: -200 mV $< V <$ 42 mV. This corresponds to a window $0.02 < k_r < 0.33$ and $0.17 < k_i < 1.24$ for the rates. This rectangle lies almost entirely in Region IV of the phase diagram (Fig. 5.17). This in agreement with the experimental observations, as no large scale autonomous oscillations have been observed with the present system, and most firings of the AA result in single shot APs. However, the possibility of observing oscillations in a single AA may still remain. Fig. 5.18 shows that, though small, it is possible for secondary firings to occur in the AA. Thus, while the KvAP in its current form is most likely not suitable for exploring some of the more interesting behaviors discussed in this chapter, the location of its rates in phase space is not as far from

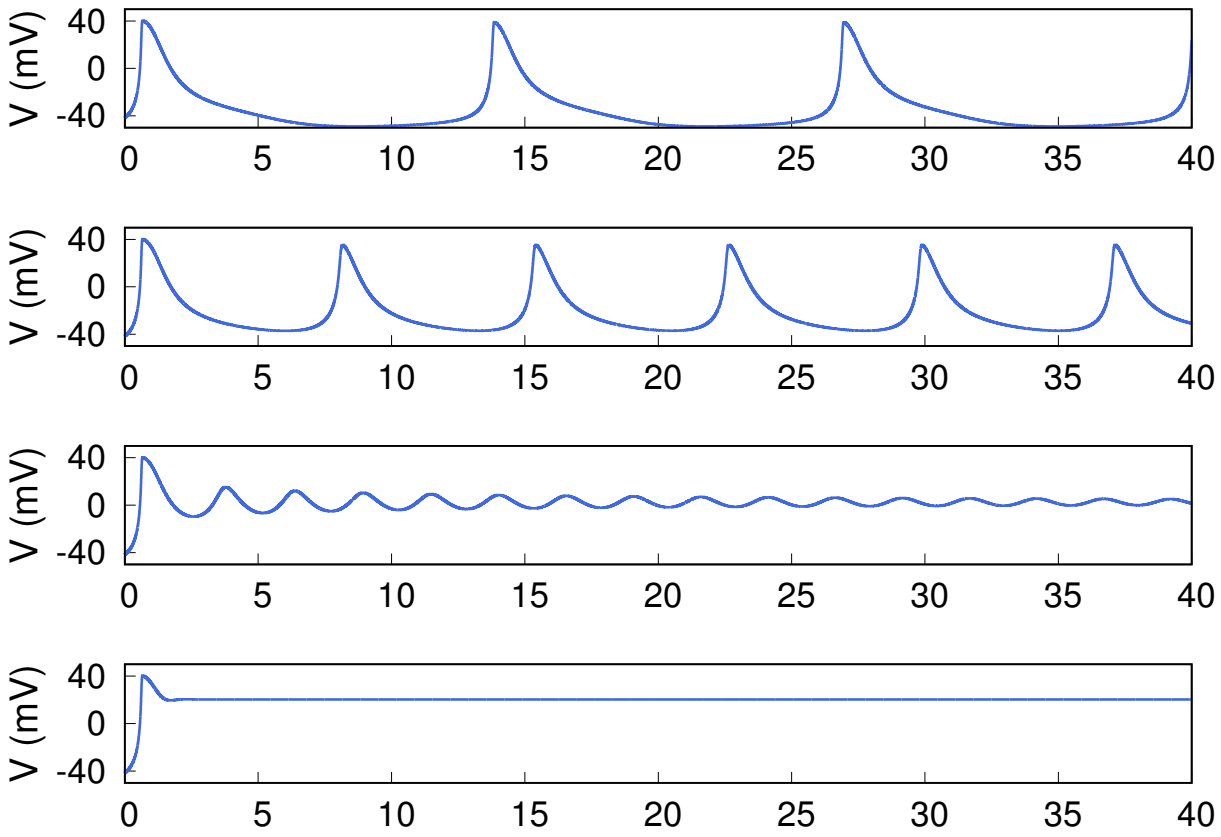

Figure 5.16: Representative time traces of the 3D model with voltage dependent recovery and inactivation rates. The x-axis is time (s), and the traces from top to bottom are representative of regions $\mathrm{I}-\mathrm{IV}$, and correspond to $\kappa_r = 0.037, 0.038, 0.06$, and $0.3\,\mathrm{s}^{-1}$, respectively. The fixed inactivation and recovery parameters are: $\kappa_i = 3\,\mathrm{s}^{-1}$, $\alpha_r = -20\,\mathrm{V}^{-1}$, $\alpha_i = 20\,\mathrm{V}^{-1}$, $V_0^{(r)} = V_0^{(i)} = 0$, with clamp value $V_c = -56\,\mathrm{mV}$. Other parameters (N_0, C, etc.) are identical to the voltage independent case (Table 5.1). The top two traces are chosen to showcase the sharp transition between Region I and Region II.

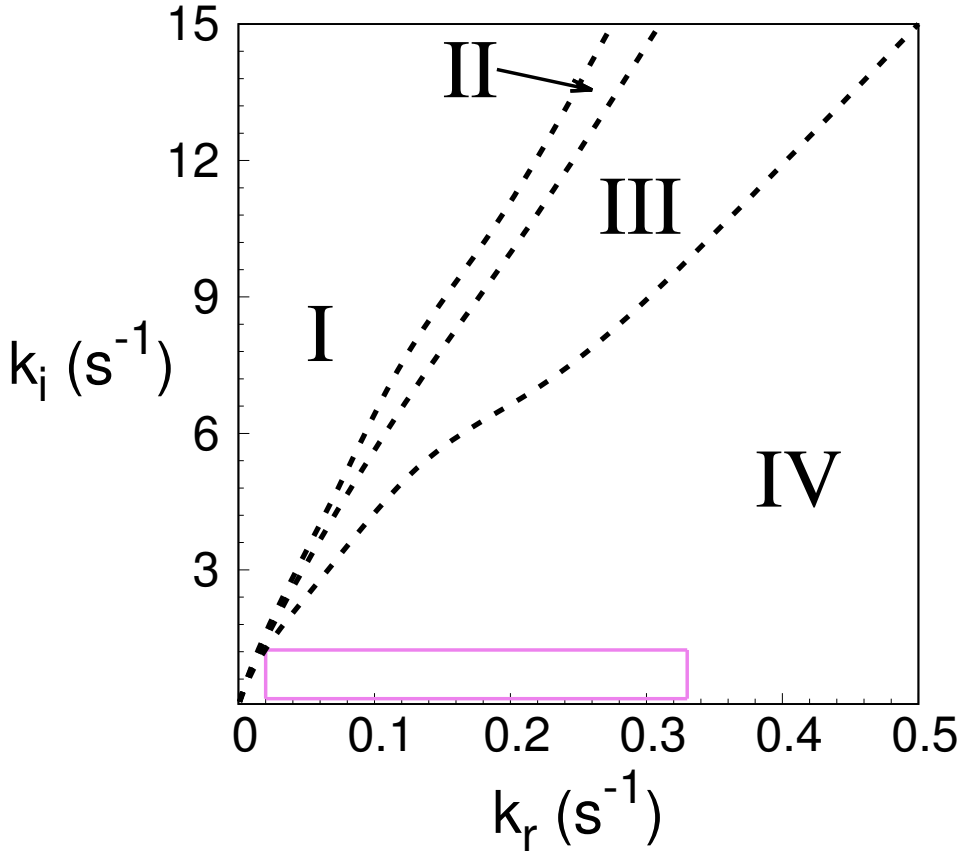

Figure 5.17: Experimentally measured inactivation and recovery rates mapped onto the phase diagram (violet).

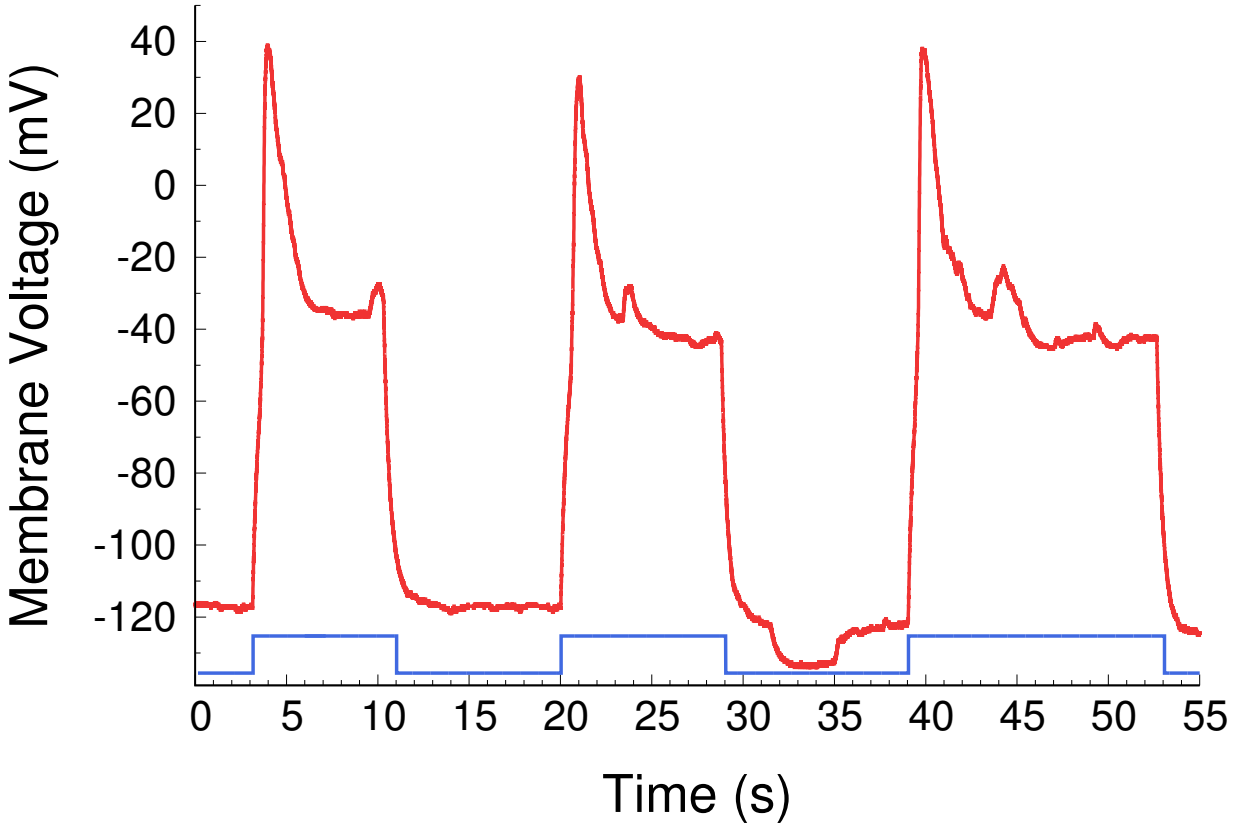

Figure 5.18: Action potentials (red) from the AA elicited in the usual way, by stepping the clamp (blue, not to scale) from the resting potential to an above threshold value. Of interest is the secondary firings which occur without additional input to the CLVC.

autonomous oscillations as previously believed.

5.5 Discussion

The simplified Hodgkin-Huxley type model analyzed in this chapter captures the dynamics of the experimental system quite well. The reduced number of parameters in the model allows a mapping of the important features of the system's parameter space in the form of a phase diagram. A key insight is that the AA, a synthetic biology system consisting of one

voltage gated channel species with inactivation, can be dynamically equivalent to a biological system of two voltage gated channel species without inactivation (e.g. the Morris-Lecar model). This raises the question of whether action potentials dependent on a single gated channel species exist (or have existed) in nature. To my knowledge, no such system has been identified.

The bifurcations in the model that occur when the system moves across regions in the phase diagram have universal character, which should therefore be maintained across different systems. Indeed, the Hopf bifurcation corresponding to the onset of AP trains seen in the AA is well established for the neuron [28], and is commonly encountered in other models of excitability (e.g. the Chialvo map [43]). In contrast, the transition separating regions I and II in the phase diagram is less established. In fact, this transition does not seem to have been discussed in the electrophysiology literature, either in theory or experiments. A qualitative analogy with the magnetization transition also prompted a search for hysteresis, which is indeed present.

The analysis of the AA as a dynamical system discussed here has been focused on transitions in the model as a function of the inactivation and recovery rates, k_i and k_r. The motivation for focusing on the rates stems from the desire to establish guidelines for the future choice of channels, as a direction for potentially improving the experimental system. The main conclusion here is that channel with much faster (or more strongly voltage dependent) inactivation would be desirable for generating interesting dynamics. Using the measured rates of KvAP as a base, a faster recovery rate would place it at higher in the phase plane of k_r, k_i, where the dynamics of Region I or Region II may be possible. Alternative channels aside, it should be noted that the same bifurcations can also be explored as a function of parameters which are experimentally controlled in the AA: χ_c and R_c. For example, Fig. 5.19 shows plots of the firing rate vs clamp conductance χ_c for the reduced

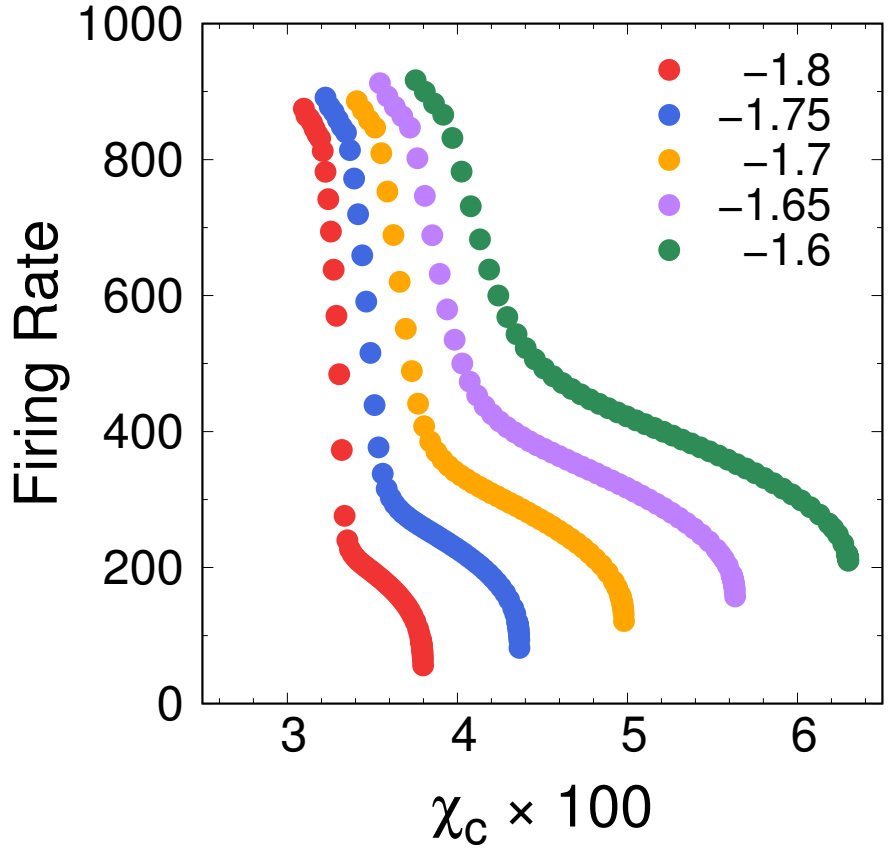

Figure 5.19: Firing rate of the AA as a function of the clamp conductance, χ_c, computed for the 2D voltage independent model. Each curves corresponds to a different V_c values (legend). For lower clamp values a sharp transition occurs in firing rate as χ_c is increased past a critical value (Region II $\rightarrow$ Region I).

2D model, for different values of the clamp voltage V_c. The transition I $\rightarrow$ II is again visible as a sharp increase in firing rate as χ_c is lowered past a critical value. The fact that the transition is also present in this slice of the parameter space means that it may be possible to design an experiment to observe it with the current AA setup, as both χ_c and V_c are control parameters. It would be difficult to observe this same behavior in experiments with living cells, because one does not have the same control over the experimental parameters.

CHAPTER 6

Connected Systems

Despite the fact that the excitable system discussed in this work is named "Artificial Axon" (for historic reasons), the action potentials generated by the AA do not actually propagate in space as they would in the biological axon. While there are plans to address this directly by developing a space extended version of the AA, this chapter will instead focus an alternative approach and one of the long term goals of the AA project: building a network of interconnected AAs. The first step in such an endeavor is the addition of "electronic synapses" to the system. These connections introduce the possibility of feedback, and serve as ways for individual AAs to communicate among each other. The choice of synaptic strength enables the formation of both excitatory and inhibitory connections, mirroring the characteristics of the biological system. Preliminary results with two connected AAs will be discussed. Specifically, a system which propagates action potentials discretely, and initial experimental and numerical results for the two AA oscillator.

6.1 Electronic Synapse

To connect individual AAs, a current clamp circuit (Fig. 2.3) is used as an electronic imitation of a synapse. The mechanism is similar to that of the dynamic clamp used in traditional electrophysiology experiments [44], though simplified. A synapse links two AAs by receiving the voltage from the "pre-synaptic" AA as input, and delivering a current proportional to that voltage to the post-synaptic AA as output. These synapses are tunable via the coefficient of proportionality α, and the activation threshold V_T (if the pre-synaptic voltage

is below V_T the synapse is "off", it does not inject any current). Thus, the current delivered by a synapse is given by:

$$I_2(t) = \alpha\, V_1(t)\, \Theta[V_1(t) - V_T] \tag{6.1}$$

where Θ is the step function, and the subscripts "1" and "2" denote the pre-synaptic and post-synaptic AAs, respectively; and so for $\alpha > 0$ the synapse is "excitatory" (injecting positive current), while for $\alpha < 0$ it is "inhibitory". The specifications of the current clamp are described in Ch. 2, and the control parameters of the synapse α and V_T are set directly in the LabView program which interfaces with the AA platform. With the synapse active, the equation describing the membrane voltage in the post-synaptic AA will have an additional term which corresponds to the synapse current:

$$\frac{dV}{dt} = \frac{N_0\chi}{C}\left(p_o(t) + \chi_\ell/\chi\right)\left[V_N - V(t)\right] + \frac{1}{RC}\left[V_c - V(t)\right] + \frac{1}{C}I_2(t) \tag{6.2}$$

In the experiments, the usual value for the threshold is $V_T = 0$, so that the synapse is only active if there is firing in the pre-synaptic AA. Typical values of the synapse "strength" are of the order $|\alpha| \sim 10\,\mathrm{pA}\ /\ \mathrm{mV} = 10\,\mathrm{nS}$. For excitatory synapses, the value of α is chosen such synaptic current is just enough to bring the AA above threshold, so that the dynamics arising from the opening of the ion channels are preserved.

6.2 Discrete Propagation

With the current experimental setup supporting up to two AAs and two synapses, the simplest connected system that can be constructed consists of two AAs connected by a single "excitatory" synapse ($\alpha > 0$). Fig. 6.2 shows experimental time traces of the voltage for this configuration. The first axon (AA_1) is caused to fire in the standard way, by stepping up its

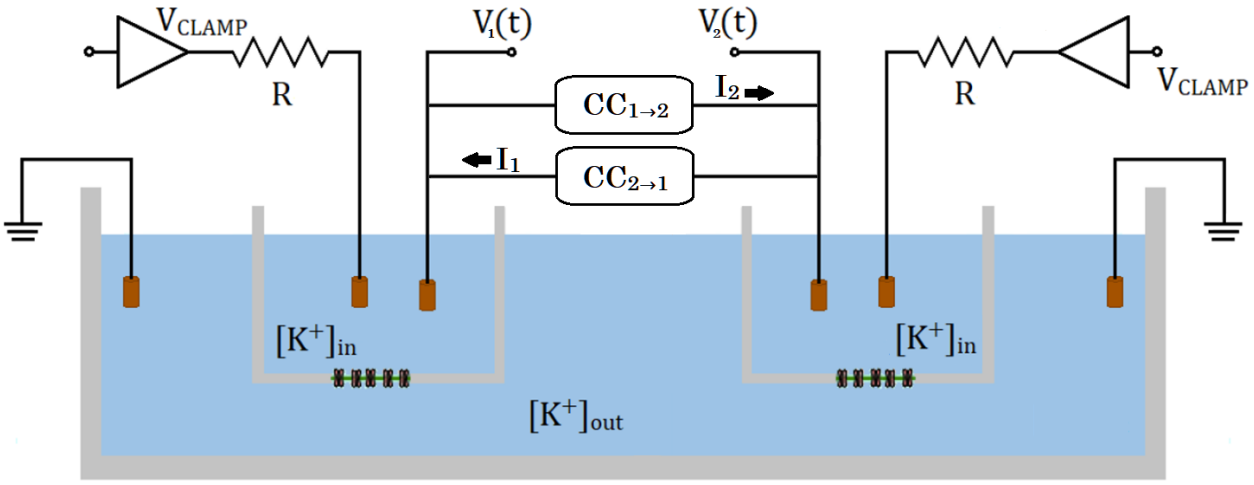

Figure 6.1: Diagram of two connected Artificial Axons. Each axon possesses its own clamp and measurement electrode. The current clamps which connect the AAs output through the measurement electrode. The two separate ground electrodes are connected externally.

clamp ($CLVC_1$) above threshold from the resting value. As V_1 crosses zero from the opening of the ion channels, the synapse starts to inject positive current into AA_2, eventually causing it to fire. Then, as the channels in AA_1 inactivate, V_1 crosses zero again in the downwards direction and the synapse stops injecting current. V_2 is pulled back to the resting potential by a combination of channel inactivation and its clamp ($CLVC_2$). During this whole process $CLVC_2$ is held steady at the resting value. V_1 does not return to its resting potential because there are no further inputs to $CLVC_1$ after the initial step up. The end result is that AA_2 goes through a complete action potential cycle, including repolarization, with AA_1 acting as the input. If AA_2 was connected in the same way to a third axon AA_3, a similar action potential cycle would be generated in AA_3, and so on. A system of several AAs linked in such a way would allow for discrete spatial propagation of action potentials. The configuration described here is similar to a previously result in the lab [27], in which the firing of an action potential in AA_1 elicits a firing in AA_2. The difference being that, here AA_1 is made to fire via adjustment of its clamp value, rather than using an external current source, reducing the number of electronic components in the system. In summary, with a single excitatory

synapse, AA_1 provides an input signal to AA_2 which then fires a complete action potential cycle. AA_1 can be thought of as a sensory input, which could be realized in practice by embedding light or chemically gated channels in AA_1, for example.

6.3 Oscillator with Two Artificial Axons

As discussed in Ch. 5, a single AA with KvAP cannot sustain autonomous oscillations for a constant input current. Nevertheless, by connecting two AAs with synapses it is in principle possible to construct an oscillator. For this purpose a second synapse is added to the previous construction which provides inhibitory feedback. Now AA_1 connects to AA_2 through an excitatory synapse ($\alpha_{12} > 0$), and AA_2 connects back to AA_1 through an inhibitory synapse ($\alpha_{21} < 0$). Fig. 6.3(a) shows an experimental result with this set up, with the only input once again being the initial step up of $CLVC_1$. The dynamics are similar to Fig. 6.2 at first, with the excitatory synapse playing the same role as before. However, now when V_2 crosses zero, the inhibitory synapse starts injecting negative current into AA_1, pulling V_1 down to negative values below the resting potential (hyperpolarization). As V_2 crosses zero again on the falling edge, the inhibitory synapse shuts off and AA_1 repolarizes (V_1 rises again) since the $CLVC_1$ remains at an above threshold value. If AA_1 is able to fire as it did initially as a result of this repolarization, in principle the process would repeat and a train of APs would be generated in both AAs, i.e. an oscillator. As Fig. 6.3(a) shows, this did not occur in the experimental attempt, as the second firing of AA_1 was significantly weaker, due to an insufficient number of channels recovering from the inactive state during the hyperpolarization step. This in turn meant that the current provided to AA_2 through the excitatory synapse was not enough to elicit a second AP, and the "oscillations" died out.

Fig. 6.3(b) shows a numerical simulation which replicates the protocol and experimental

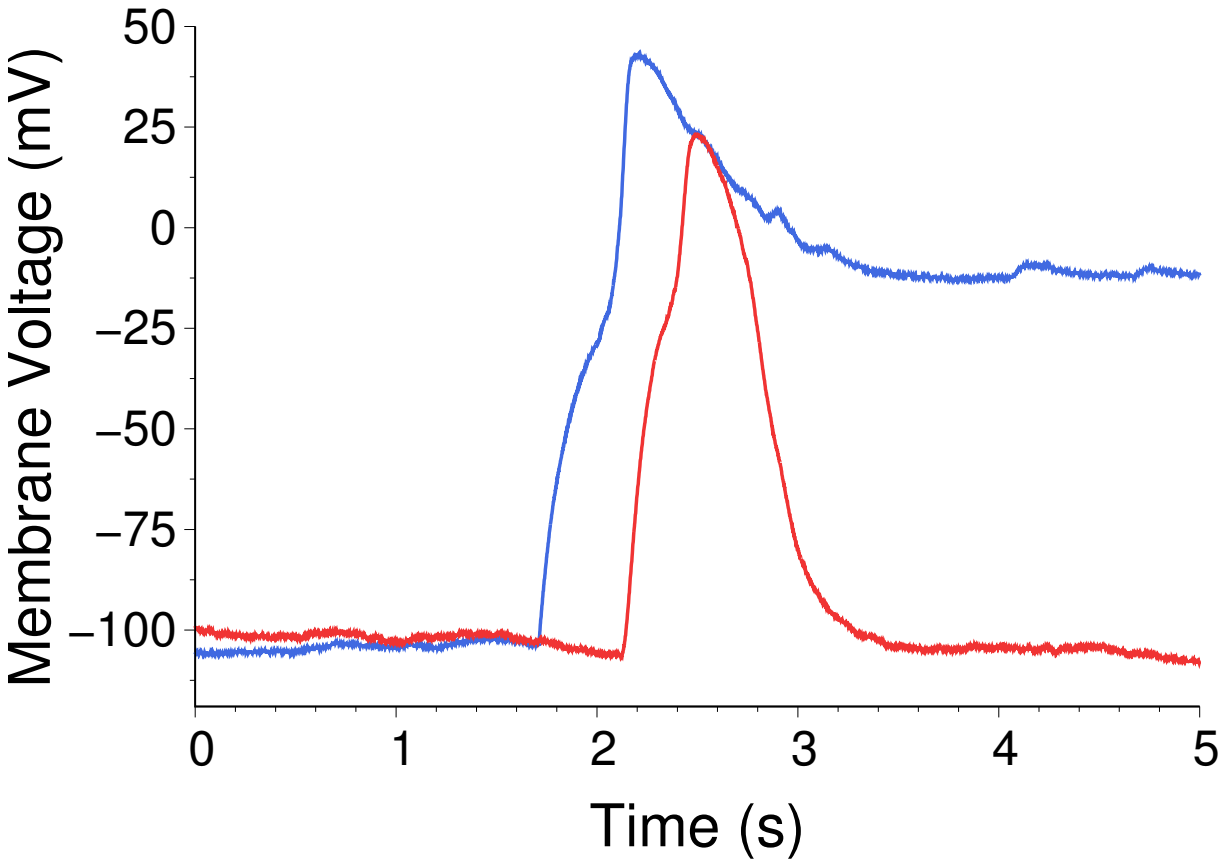

Figure 6.2: Experimental measurements of the voltage for a two AA system connected by one excitatory synapse, showing discrete propagation of an action potential. Both AAs begin with their respective clamps at a below threshold value, $V_r \approx -100\,\text{mV}$. The process initiates when AA_1 (blue) is caused to fire by raising its CLVC above threshold at $t \approx 1.8\,\text{s}$. When V_1 crosses zero, the synapse starts to inject current into AA_2 (red), causing it to fire as well. As V_1 falls below zero due to inactivation, the synapse shuts off and V_2 is returns to its resting potential. The end result is a complete action potential in AA_2, with the initial step up of AA_1's CLVC as the only input.

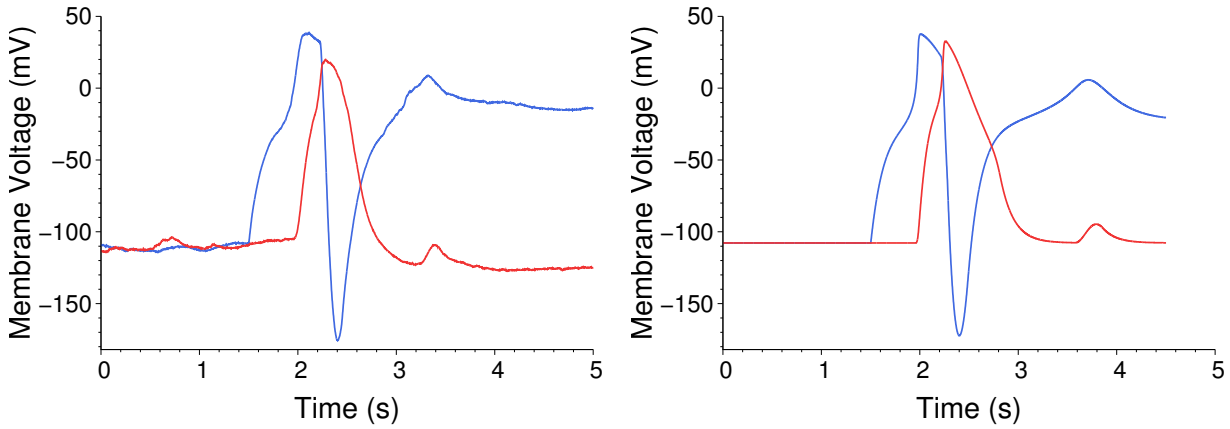

(a) (b)

Figure 6.3: **(a)** Experimental measurements of the voltage from two AAs connected by one excitatory and one inhibitory synapse. The protocol is the same as Fig. 6.2, the only difference being the addition of the inhibitory synapse $\alpha_{21} = -25\,\text{nS}$. The firing of AA_1 (blue) causes the excitatory synapse ($\alpha_{12} = 6\,\text{nS}$) to inject current into AA_2 (red), as before. When AA_2 fires, the negative synaptic current injected in AA_1 pulls V_1 down sharply. In this experiment, not enough channels in AA_1 recovered from inactivation during the negative voltage swing, as a result the second firing of AA_1 was much weaker and could not elicit firing in AA_2, prematurely ending the cycle. **(b)** The same protocol as in (a), numerically simulated with a combination of measured rates and fitted parameters: $N_0 = 250$, $C = 275\,\text{pF}$, $\chi = 167\,\text{pS}$, $\alpha_{12} = 7.33\,\text{nS}$, $\alpha_{21} = -10.67\,\text{nS}$, and $V_T = 0$.

measurements of Fig. 6.3(a). The goal being to determine whether it is possible to avoid the issue of insufficient recovery encountered in the experiment through adjustments in the controllable parameters. After various probings of the simulated system, the somewhat expected result is that to alleviate the issue of the inactivated channels, one only needs to increase the inhibitory synapse strength. Fig. 6.4 shows autonomous oscillations occurring in the model, obtained with the same parameter settings as for Fig. 6.3(b), except the strength of the inhibitory synapse $AA_2 \rightarrow AA_1$ has been increased from $\alpha_{21} = -10.67\,\text{nS}$ to $\alpha_{21} = -20\,\text{nS}$. Thus the conclusion is that autonomous oscillations are achievable with the current experimental system, and the key factor in determining whether oscillations are sustained or die out is how low AA_1 is pulled by the negative feed back from AA_2. A hyperpolarization value for AA_1 of at least $\approx -200\,\text{mV}$ is indicated by the simulations to be the minimum required for sustained oscillations under the present conditions.

6.4 Outlook

The system of two AAs connected by electronic synapses show promise for progressing the Artificial Axon system beyond single firing measurements, and serves as a prototype for future network developments. Each synapse providing an additional tunable parameter allows for a high degree of control in the experiments. The main challenge which limits the successful implementation of the oscillator, and in turn the feasibility of scaling up, is the stability of the experiment. While simulations show that a stronger inhibitory synapse is sufficient to generate oscillations with two AAs, the reality is that the lipid membrane in the experiment cannot withstand arbitrarily large voltages. As a result the synapse strengths must be carefully adjusted such that the desired dynamics can occur, while also ensuring that the stability of the experimental platform is not compromised. Given these obstacles, a substantial amount of work required to advance the AA beyond the two-well setup.

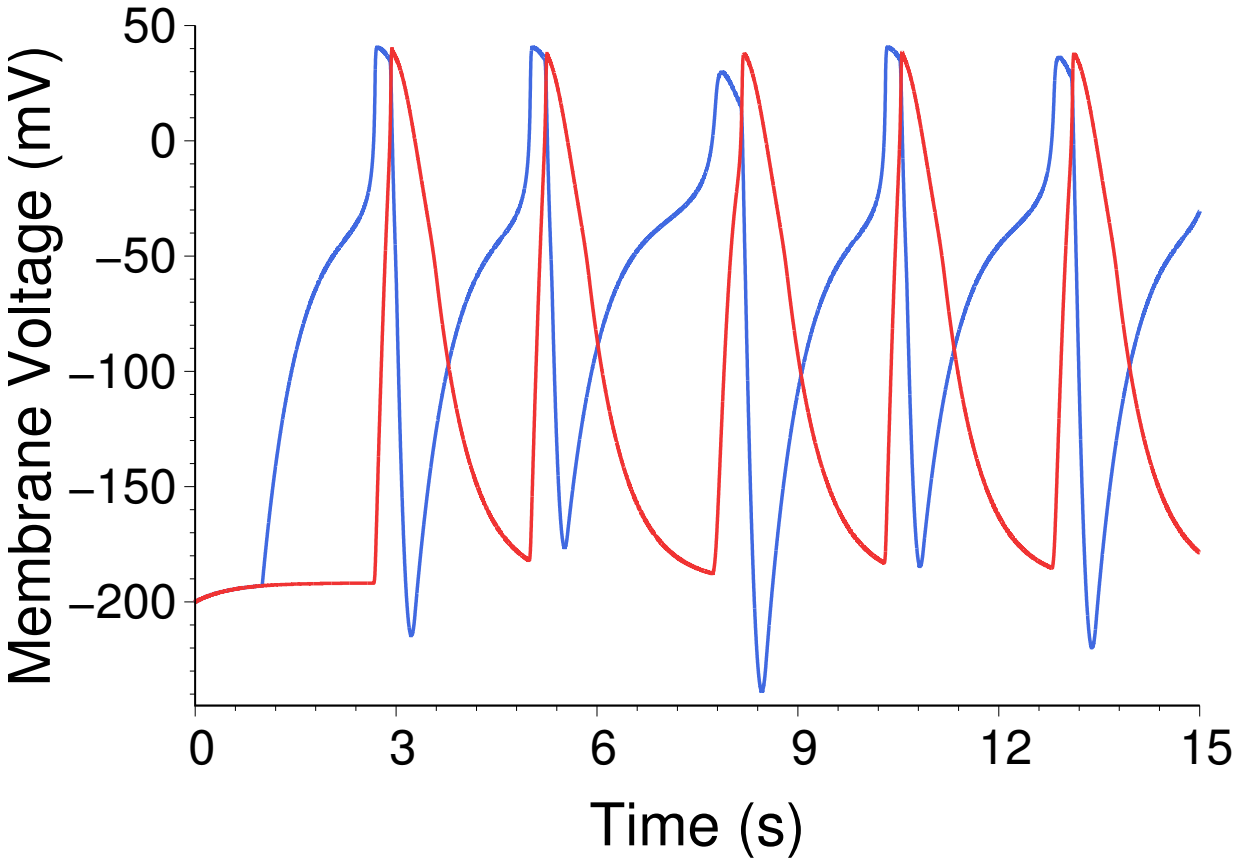

Figure 6.4: Numerical simulation of the two AA system (V_1 blue, V_2 red) identical to that of Fig. 6.3(b), except the inhibitory synapse strength has been increased to $\alpha_{21} = -20\,\text{nS}$. As a result, AA_1 experiences more intense hyperpolarization, which allows more channels to recover from inactivation and enables sustained oscillations in both AAs.

CHAPTER 7

Future Directions

In closing, the work presented here demonstrates the capabilities of the Artificial Axon as a cell-free breadboard for electrophysiological studies. The idea is to construct, at each scale, the minimal system which retains the essential properties of the more complex biological systems, and the AA fulfills such a role. As a minimal generator of action potentials, it is capable of producing the same behaviors as those in the neuron. Yet it is also distinct as an excitable system in that it generates action potentials with one ion species, a possibility which is not usually considered in traditional live cell setups.

In terms of the dynamics of a single AA, the reported measurements of critical behavior bridge the gap between the AA and real neurons through the universal properties near criticality, despite the fact that the AA as a system does not fire with the same level of complexity as the neuron. On the prospect of generating more than single shot action potentials, analysis of our minimal model for the AA shows that AP trains and oscillations are permitted by the system, and so achieving them becomes a matter of accessing the relevant regions in the phase diagram. With consideration of the control parameters which span the parameter space (k_i, k_r, V_c, and χ_c), the latter two seem especially viable as ways to move through the phase space, as they are adjustable parts of the experiment circuitry. A simple change which could lead the system to oscillations is to consider χ_c as a tunable parameter, swapping the fixed clamp resistance R_c for a potentiometer. In practice however, the range of available χ_c is restricted, as the original role of the clamp resistor (to suppress leaks, hold

the system off equilibrium, and allow for channel dynamics) must still be satisfied. On the other hand, a more difficult, but still feasible, approach is to tinker with the inactivation and recovery rates. As briefly mentioned in Ch. 3, it has been shown that different compositions of the lipid membrane have a significant effect on the kinetics of the channel, with the net charge of the lipid strongly influencing the half voltage of equilibrium opening rates [23, 30]. This phenomenon could be utilized to our advantage as a quick and simple way to "modify" channel rates without having to directly altering the channel's structure via mutagenesis. Channel kinetics may also change as a function of temperature [15, 31, 32], which could be another way to indirectly tune the system. All in all, a variety of methods can be used to increase the tunability of the system, and the implementation of some combination of them will likely necessary for exploring the phase space experimentally.

The aspect demanding the most focus in improving the system pertains to its scalability. Extending the AA beyond a two-axon configuration will require significant efforts, given the difficulty of sustaining multiple operational AAs. Fragility of the lipid membrane and the inconsistency of channel functionality are the main obstacles. Possible strategies include using hydrogels to stabilize the system [24, 25], an endeavor which is currently underway in the lab. Other, more systemic, changes could involve moving from a suspended lipid setup to a supported lipid one.

Beyond these immediate areas of improvement, there are several long term directions for the AA which we would like to explore in the future, ideally once issues of robustness and ease of construction are ameliorated. The first is the implementation of different types of channels in AA. One could imagine a chip consisting of an array of independent AAs, each constructed with a different kind of ion channel. Such a system could be developed into a "synthetic nose" for assaying potential new drugs with respect to their effect on channel dynamics, for example. Another direction of interest is the creation of a space extended

AA, with generated action potentials propagating in space as they do in the real axon. Theoretical work done on this front by another lab member has shown that even a minimal implementation can generate interesting behavior, such as the propagation of solitary waves [39]. Finally, we have in mind to build a "neural network" on the computer which obey the dynamics of the AA. The idea is inspired by the function of chromatophores in the skin of the octopus, which allow them to camouflage in response to changes in the environment. By combining modern machine learning techniques with the biological underpinnings of the AA, we hope make progress on addressing a question which is no doubt the most consequential one of the modern age: "How does an octopus think?"

Bibliography

[1] Jonathan Platkiewicz and Romain Brette. A Threshold Equation for Action Potential Initiation. *PLoS Comput Biol*, 6(7):e1000850, 2010.

[2] D. W. Bechert, M. Bruse, W. Hage, and R. Meyer. Fluid Mechanics of Biological Surfaces and their Technological Application. *Naturwissenschaften*, 87(4):157–171, 2000.

[3] Jiadi Zhu, Teng Zhang, Yuchao Yang, and Ru Huang. A comprehensive review on emerging artificial neuromorphic devices. *Applied Physics Reviews*, 7:011312, 2020.

[4] Mark W Barnett and Philip M Larkman. The action potential. *Practical Neurology*, 7: 192–197, 2007.

[5] D. A. Jacobson and L. H. Philipson. Action potentials and insulin secretion: New insights into the role of Kv channels. *Diabetes, Obesity and Metabolism*, 9:89–98, 2007.

[6] Alexei Verkhratsky and Vladimir Parpura. History of Electrophysiology and the Patch Clamp. In *Patch-Clamp Methods and Protocols*, volume 1183, pages 1–19. Springer New York, New York, NY, 2014. ISBN 978-1-4939-1095-3 978-1-4939-1096-0.

[7] A. L. Hodgkin and A. F. Huxley. A quantitative description of membrane current and its application to conduction and excitation in nerve. *J. Physiol. (Lond.)*, 117:500–544, 1952.

[8] Bertil Hille. *Ion channels of excitable membranes*. Sinauer, Sunderland, Mass, 3rd ed edition, 2001. ISBN 978-0-87893-321-1.

[9] Christine Beeton. Differences in ion channel phenotype and function between humans and animal models. *Frontiers in Bioscience*, 23:43–64, 2018.

[10] Boris Martinac, Yoshiro Saimi, and Ching Kung. Ion Channels in Microbes. *Physiological Reviews*, 88(4):1449–1490, 2008.

[11] Robert Bähring and Manuel Covarrubias. Mechanisms of closed-state inactivation in voltage-gated ion channels. *The Journal of Physiology*, 589:461–479, 2011.

[12] Barbara A Niemeyer, Laurence Mery, Christian Zawar, Arnt Suckow, Francisco Monje, Luis A Pardo, Walter Stühmer, Veit Flockerzi, and Markus Hoth. Ion channels in health and disease: 83 rd Boehringer Ingelheim Fonds International Titisee Conference. *EMBO reports*, 2:568–573, 2001.

[13] Youxing Jiang, Alice Lee, Jiayun Chen, Vanessa Ruta, Martine Cadene, Brian T. Chait, and Roderick MacKinnon. X-ray structure of a voltage-dependent K+ channel. *Nature*, 423:33–41, 2003.

[14] Xiao Tao and Roderick MacKinnon. Cryo-EM structure of the KvAP channel reveals a non-domain-swapped voltage sensor topology. *eLife*, 8:e52164, 2019.

[15] Rajnish Ranjan, Emmanuelle Logette, Michela Marani, Mirjia Herzog, Valérie Tâche, Enrico Scantamburlo, Valérie Buchillier, and Henry Markram. A Kinetic Map of the Homomeric Voltage-Gated Potassium Channel (Kv) Family. *Frontiers in Cellular Neuroscience*, 13:358, 2019.

[16] Donhee Ham, Hongkun Park, Sungwoo Hwang, and Kinam Kim. Neuromorphic electronics based on copying and pasting the brain. *Nature Electronics*, 4:635–644, 2021.

[17] Vijay Balasubramanian. Brain power. *Proceedings of the National Academy of Sciences*, 118:e2107022118, 2021.

[18] A. Ariyaratne and G. Zocchi. Nonlinearity of a voltage gated potassium channel revealed by the mechanical susceptibility. *PRX*, 3:011010, 2013.

[19] A. Ariyaratne and G. Zocchi. Toward a minimal artificial axon. *J. Phys. Chem. B*, 120: 6255, 2016.

[20] Catherine Morris and Harold Lecar. Voltage oscillations in the barnacle giant muscle fiber. *Biophys. J.*, 35:193 – 213, 1981.

[21] Amila Dinesh Ariyaratne. *Rheology of biological macromolecules*. PhD thesis, University of California, Los Angeles, 2015.

[22] Hector Garcia Vasquez. *Development of the Computational Unit for an Artificial Axon Network*. PhD thesis, University of California, Los Angeles, 2018.

[23] Daniel Schmidt, Samuel R. Cross, and Roderick MacKinnon. A Gating Model for the Archeal Voltage-Dependent K+ Channel KvAP in DPhPC and POPE:POPG Decane Lipid Bilayers. *Journal of Molecular Biology*, 390:902–912, 2009.

[24] Tae-Joon Jeon, Noah Malmstadt, Jason L. Poulos, and Jacob J. Schmidt. Black lipid membranes stabilized through substrate conjugation to a hydrogel. *Biointerphases*, 3: FA96–FA100, 2008.

[25] Tae-Joon Jeon, Noah Malmstadt, and Jacob J. Schmidt. Hydrogel-Encapsulated Lipid Membranes. *Journal of the American Chemical Society*, 128:42–43, 2006.

[26] Ziqi Pi and Giovanni Zocchi. Critical behavior in the artificial axon. *J. Phys. Commun.*, 5:125013, 2021.

[27] H. G. Vasquez and G. Zocchi. Coincidences with the artificial axon. *EPL*, 119:48003, 2017.

[28] Christof Koch. *Biophysics of Computation*. Oxford University Press, 1999.

[29] Vanessa Ruta, Youxing Jiang, Alice Lee, Jiayun Chen, and Roderick MacKinnon. Functional analysis of an archaebacterial voltage-dependent K+ channel. *Nature*, 422(6928): 180–185, 2003.

[30] Élise Faure, Christine Thompson, and Rikard Blunck. Do Lipids Show State-dependent Affinity to the Voltage-gated Potassium Channel KvAP? *Journal of Biological Chemistry*, 289:16452–16461, 2014.

[31] Sm Thompson, Lm Masukawa, and Da Prince. Temperature dependence of intrinsic membrane properties and synaptic potentials in hippocampal CA1 neurons in vitro. *The Journal of Neuroscience*, 5:817–824, 1985.

[32] A. L. Hodgkin and B. Katz. The effect of temperature on the electrical activity of the giant axon of the squid. *The Journal of Physiology*, 109:240–249, 1949.

[33] Steven H. Strogatz. *Nonlinear Dynamics and Chaos*. Westview Press, 2015.

[34] M. Sekerli, C.A. DelNegro, R.H. Lee, and R.J. Butera. Estimating Action Potential Thresholds From Neuronal Time-Series: New Metrics and Evaluation of Methodologies. *IEEE Trans. Biomed. Eng.*, 51(9):1665–1672, 2004.

[35] Linan Guan, Bing Jia, and Huaguang Gu. A Novel Threshold Across which the Negative Stimulation Evokes Action Potential Near a Saddle-Node Bifurcation in a Neuronal Model with Ih Current. *International Journal of Bifurcation and Chaos*, 29:1950198, 2019.

[36] E. M. Izhikevich. Neural excitability, spiking and bursting. *Int. J. Bifurcat. Chaos*, 10: 1171–1266, 2000.

[37] K. Tsumoto, H. Kitajima, T. Yoshinaga, K. Aihara, and H. Kawakami. Bifurcations in morris-lecar neuron model. *Neurocomputing*, 69:293–316, 2006.

[38] Z. Zhao and H. Gu. Transitions between classes of neuronal excitability and bifurcations induced by autapse. *Sci Rep*, 7:6760, 2017.

[39] Xinyi Qi and Giovanni Zocchi. Kink propagation in the artificial axon. *EPL*, 137:12005, 2022.

[40] Kunichika Tsumoto, Hiroyuki Kitajima, Tetsuya Yoshinaga, Kazuyuki Aihara, and Hiroshi Kawakami. Bifurcations in Morris–Lecar neuron model. *Neurocomputing*, 69: 293–316, 2006.

[41] Congmin Liu, Xuanliang Liu, and Shenquan Liu. Bifurcation analysis of a Morris–Lecar neuron model. *Biological Cybernetics*, 108:75–84, 2014.

[42] Nigel Goldenfeld. *Lectures On Phase Transitions And The Renormalization Group (Frontiers in Physics v. 85)*. CRC Press, 2018.

[43] Dante R. Chialvo. Generic excitable dynamics on a two-dimensional map. *Chaos, Solitons & Fractals*, 5:461–479, 1995.

[44] Ronald Wilders. Dynamic clamp: A powerful tool in cardiac electrophysiology. *The Journal of Physiology*, 576:349–359, 2006.